Geometric Context From Single And Multiple Views

Alexander John Flint
Exeter College

Supervised by Prof Ian Reid and Prof David Murray
Active Vision Laboratory
Robotics Research Group
Department of Engineering Science
University of Oxford

Trinity Term 2012

This thesis is submitted to the Department of Engineering Science, University of Oxford, for the degree of Doctor of Philosophy. This thesis is entirely my own work, and, except where otherwise indicated, describes my own research.

Alexander John Flint
Exeter College

Doctor of Philosophy
Trinity Term 2012

Geometric Context From Single And Multiple Views

Abstract

In order for computers to interact with and understand the visual world, they must be equipped with reasoning systems that include high–level quantities such as objects, actions, and scenes. This thesis is concerned with extracting such representations of the world from visual input.

The first part of this thesis describes an approach to scene understanding in which texture characteristics of the visual world are used to infer scene categories. We show that in the context of a moving camera, it is common to observe images containing very few individually–salient image regions, yet overall texture structure often allows our system to derive powerful contextual cues about the environment. Our approach builds on ideas from texture recognition, and we show that our algorithm out–performs the well–known Gist [67] descriptor on several classification tasks.

In the second part of this thesis we we are interested in scene understanding in the context of multiple calibrated views of a scene, as might be obtained from a Structure–from–Motion or Simultaneous Localization and Mapping (SLAM) system. Though such systems are capable of localizing the camera robustly and efficiently, the maps produced are typically sparse point-clouds that are difficult to interpret and of little use for higher–level reasoning tasks such as scene understanding or human-machine interaction. In this thesis we begin to address this deficiency, presenting progress towards modeling scenes using semantically meaningful primitives such as floor, wall, and ceiling planes.

To this end we adopt the indoor Manhattan representation, which was recently proposed for single–view reconstruction [43]. This thesis presents the first in–depth description and analysis of this model in the literature. We describe a probabilistic model relating photometric features, stereo photo–consistencies, and 3D point clouds to Manhattan scene structure in a Bayesian framework. We then present a fast dynamic programming algorithm that solves exact MAP inference in this model in time linear in image size. We show detailed comparisons with the state–of–the art in both the single– and multiple–view contexts.

Finally, we present a framework for learning within the indoor Manhattan hypothesis class. Our system is capable of extrapolating from labelled training examples to predict scene structure for unseen images. We cast learning as a structured prediction problem and show how to optimize with respect to two realistic loss functions. We present experiments in which we learn to recover scene structure from both single and multiple views — from the perspective of our learning algorithm these problems differ only by a change of feature space. This work constitutes one of the most complicated output spaces (in terms of internal constraints) yet considered within a structure prediction framework.

Contents

Acknowledgements

This thesis is the culmination of many years of work and would not have been possible without the help and support of many people.

I would like to thank my supervisors, Professors Ian Reid and David Murray for their guidance and patience, and good spirit throughout the long English winters.

If there are any ideas of any value within this thesis, credit should undoubtedly go to the amazing people I had the privilege to work with at the Active Vision Lab in Oxford. In particular I would like to thank Christopher Mei and Gabe Sibley for inspiration, encouragement, and the most interesting coffee–time discussions I have had the privilege of participating in. In addition, I owe much to discussions and collaborations with Michael Osborne, Matthew Blaschko, Eric Sommerlade, and Victor Prisacariu.

My research was funded by a Clarendon Scholarship, for which I owe gratitude to the wonderful people at the Clarendon Foundation and the Oxford University Press.

Throughout this work I have enjoyed the unfailing support of my family. To my mother, Kate, my father, Roger, and my brother, Hugh: I owe you everything. Thank you for guiding me here, guiding me through, and always guiding me onwards.

I would also like to thank partners–in–crime Akshat Rathi, Priya and Preethi Vijayakumar, and Michelle Fernandez, for making my time at Oxford what it was.

Notation

Throughout this thesis, the following conventions will be used for typesetting mathematics unless otherwise indicated:

- **Sets** are written in calligraphic type: $\mathcal{S}$.
- **Fields** are written in upper case: $\mathbb{F}$. In particular, $\mathbb{R}$ denotes the reals and $\mathbb{Z}$ denotes the integers.
- **Vectors** are written in lower case bold: $\boldsymbol{x}$. Vectors are usually column vectors, with elements specified by subscript index (*e.g.* $\boldsymbol{x} = (x_1, x_2, x_3)$).
- **Matrices** are written in upper case: H. The entry in the i^{th} row and j^{th} column is $H_{i,j}$.
- **Conditional probabilities** are written $P(A \mid B)$. In most cases A and B will correspond to the event that certain variables take on certain values, for example: $P(x \mid y)$.
- **Expectations** of x with respect to a distribution p are written $\mathbb{E}_p[x]$.
- **Gradients** of y with respect to x are written $\frac{\partial y}{\partial x}$.
- **Inner products** for geometric quantities are written $\boldsymbol{x} \cdot \boldsymbol{y}$. In the more general context of Hilbert spaces we switch to the notation $\langle \boldsymbol{x}, \boldsymbol{y} \rangle$.
- Where there is a need to differentiate the estimated and true values of a quantity y, the former will be written $\hat{y}$ and the latter y^*.

1

Introduction

Humans are visual in nature and as such we have constructed our world around visual cues. We use written street signs rather than, say, smells or sounds to navigate the road network because our biological vision system has both higher fidelity and wider bandwidth than other senses. In order for computers to understand and interact with our world we must either develop automated vision systems or re–signpost our world. Computer vision is the endeavour to take the former route.

This thesis addresses the problem of developing a computer vision system that understands the geometry of the environment at a semantically meaningful level. By "semantically meaningful" we mean at the level of objects and events relevant to humans and human interactions, as in the difference between an city roadmap (which we would say is semantically meaningful on account of its high–level representation of quantities such as roads and addresses) and a set of 3D points in space. Our goal is to recover semantically meaningful models of the world from visual input.

To this end we explore two types of models. The first relates low–level photometric information directly to high–level concepts such as the function of an environment and the location of objects within it. Building on recent progress in contextual computer vision, we show how to derive visual context directly from an environment's texture structure. The second type of model we explore relates images to high–level concepts via an intermediate representation of

high–level scene geometry. Contrary to much previous work in geometric computer vision, we select a representation that leads naturally to semantic–level reasoning tasks such as place recognition and object detection, for which we argue that the indoor Manhattan model is an attractive choice. Much of this thesis concerns the estimation of indoor Manhattan models from single and multiple images.

1.1 Motivation

The research presented here has been motivated from a variety of angles over time. This thesis was originally motivated by the application area of augmented reality (AR). In the broadest sense, AR systems aim to overlay relevant information onto a human's visual field–of–view. One important challenge is to build a 3D model of the environment and track the sensor with respect to it in order to create the illusion of annotations that move with 3D objects in the environment. This problem is known as simultaneous localisation and mapping (SLAM), and has seen great progress over the past several decades. In particular, visual SLAM, in which the sensing apparatus is a camera, has taken great strides, moving from single rooms to a entire cities, and from costly off–line processing to real–time systems. However, in order to select relevant information and have annotations interact seamlessly with other visual stimulus, the AR system must have some understanding of the visual world beyond the low–level point clouds generated by SLAM systems.

It is neither surprising nor objectionable that so much effort towards AR has focused on visual SLAM, but now that high–performance SLAM systems *are* available, the question that naturally presents itself is: *are we done yet?* In this thesis we will argue that while SLAM is an important first step, many challenging and general computer vision problems remain to solve before AR systems can be fully realised. For example, the relevance of certain types of information to the wearer varies with the type of environment that the wearer is moving within. Directions to a restaurant may be relevant while outdoors but directions to the kitchen are less likely to be helpful within the wearer's own house. Within the home, the augmentations most useful in

the kitchen are likely to be different to those suitable to the bedroom. Furthermore, the likely locations of various objects is tightly coupled to the surfaces and boundaries within an environment. A human would not search for lost keys on the ceiling first, nor outside a window, but to make this inference an AR system must first identify key surfaces and their orientations. These problems are not immediately solved by the ability to locate oneself within an arbitrary 3D coordinate frame, though a major theme of this thesis is how to use such information together with other image evidence for high–level reasoning tasks.

Although this thesis was originally motivated by applications within AR, much inspiration was drawn from the single–view computer vision literature, principally from the literature dedicated to *scene understanding*, which is the problem of understanding images in terms of objects, actions, and semantically meaningful geometric primitives. Scene understanding has a long history within the single–view computer vision literature but a shorter history within the multiple–view literature. One motivation for this research is the extension of traditional scene understanding techniques to the context of multiple views. This is a challenging problem because single–view techniques are commonly cast in terms of rectangular arrays of pixels, which do not naturally incorporate the kind of geometric information available in a multiple view context.

There is a very large literature on single–view scene understanding, and a corresponding plethora of models to choose from. The focus of this thesis is on the extraction of high–level geometric information within indoor–type environments, with relevance to scene categorisation and object localisation. The hope is that this problem is large enough to be interesting, small enough to be tractable, and perhaps insightful enough to be instructive for future research in the relatively new domain of multiple–view scene understanding.

There are many reasons that utilising multiple views is an attractive direction for scene understanding research. Firstly, video on the internet has become increasingly important over the past several years, increasing the relevance of computer vision systems that process video streams rather than single images. Secondly, mobile phones have become more attractive devices for vision systems as the processors and cameras now ubiquitously attached to them con-

Figure 1.1: An example of an indoor Manhattan scene.

tinue to become more powerful. Finally, depth sensing cameras have entered the mainstream consumer hardware market and are likely to become more common over the coming years.

1.2 Our Approach

In this thesis we present two approaches to deriving semantic–level scene information from visual input.

1.2.1 Photometric Models

The first model we present is a purely photometric approach and builds on ideas from texture analysis, in particular the texton model. This model associates each pixel with a discrete texture element, which is then related to the semantic–level variable of interest. We show how textons can be leveraged toward the problems of scene recognition and contextual object search. Despite the simplicity of this approach, we show that it is effective for the proposed problems.

In contrast to systems based on edges, interest points, or local descriptors, utilising texture information allows us to leverage visual information in non–salient image regions. This is particularly important for environments in which there are few individually distinctive image patches, yet the overall scene appearance conveys significant information.

We present qualitative results motivating the use of texture structure for the stated task, followed by a formal probabilistic model and quantitative comparisons with the state–of–the–art.

1.2.2 Coarse Geometric Models

The second part of this thesis focuses on capturing geometric information in a form well–suited to semantic–level reasoning. This represents a departure from much of the scene understanding literature, in which geometric information is captured implicitly, rather than via explicit geometric assumptions. Our decision to work with explicit geometric models is motivated by the observation that much about scenes and objects is tied to the high–level shape of the environment, particularly the location of major surfaces and boundaries.

As a simple illustration of this, consider the image shown in Figure 1.1. Despite the low information content of the image – it is defined by just a handful of vertices – a human can make many high–level inferences about this environment, including answers to questions such as (in order of increasing difficulty):

1. What is the direction of gravity?
2. Where would doors most likely be found?
3. Where would a person be most likely to stand and at what scale?
4. Is this an office or a house?
5. What is the absolute scale of the environment?

While the image does not provide enough information for definitive answers to any of these questions, it does provide surprisingly strong evidence given that it consists of just a few hundred bits of information. Thus it seems that coarse geometric information is particularly valuable for high–level inference.

The image in Figure 1.1 shows one example of an indoor Manhattan environment [43], which is the hypothesis class we adopt for geometric reasoning in this thesis. Under this model the

world is composed of a floor plane, ceiling plane, and a set of vertical walls that meet at vertical edges. Indoor manhattan environments constitute a subset of the more general set of Manhattan environments, in which any arrangement of surfaces in three dominant directions is permitted. It is an attractive model for a number of reasons. Firstly, as argued above, it captures geometric information of high value for semantic–level reasoning. Secondly, despite the strong geometric assumptions, a surprisingly broad range of environments can be represented exactly or approximately as indoor Manhattan models. Thirdly, strong geometric assumptions assist in the interpretation of ambiguous image evidence, since salient information in one region can constrain the interpretation of other regions. Finally, an efficient inference algorithm exists for this hypothesis class, which is the subject of later chapters.

There is no hard distinction between a "geometry–less" and a "geometry–laden" approach to scene understanding. In either case one is drawing probabilistic inferences from images; the distinction is in how those inputs are combined, which conditional independences are assumed, and how the hypothesis class is formulated. Our choice to incorporate geometry corresponds to a particular choice of independence assumptions, which differ from those typically chosen in photometrically inspired models. This thesis is concerned with the recovery of geometry for the sake of the high–level inference that it enables, not for the sake of the geometry itself, and our choice of model reflects this.

1.3 Exegesis

The remainder of this thesis is organised as follows. Chapter 2 presents a review of literature relevant to this thesis. Due to the connection of our work to the traditionally disparate fields of SLAM and scene understanding, the literature review breaks down into scene understanding work that has touched on geometry, and SLAM work that has touched on scene understanding.

Chapter 3 presents an appearance–only approach to scene understanding in the context of a moving camera. We work with textons as the basic observation unit and present a probabilistic model connecting these to scene categories and object locations.

We then begin the presentation of our work concerning indoor Manhattan models. Chapter 4 presents the model formally, and covers various geometric observations on which later chapters rest. There is little prior work on the indoor Manhattan model, so we dedicate a full chapter to defining the model formally and describing several useful representations. We then turn in Chapter 5 to identifying the orientation of three cardinal Manhattan directions given multiple calibrated views. We show that estimating scene rotation jointly from all available views is a dramatic improvement over the standard approach of identifying vanishing points separately in each image. We also show an order of magnitude improvement over approaches that use surface normals estimated from a reconstructed point cloud.

Chapter 6 presents a probabilistic model relating sensor data to the geometric quantities we wish to extract. We give separate probabilistic models for photometric features, stereo data, and point clouds, then we show how to combine these into a fully Bayesian model, allowing our system to be easily tailored to a variety of contexts. We present a dynamic programming algorithm that solves both maximum–aposteriori and maximum–likelihood inference within our model. This inference procedure is both fast and exact, making a compelling alternative to previous approaches that explode combinatorially in model complexity.

Chapter 7 presents a learning routine in which we learn to reconstruct Manhattan environments based on training examples. We cast the learning problem in a discriminative framework and use state–of–the–art tools from the structured prediction literature. We show that learning with respect to single versus multiple views differs only by a change in feature space, and we present extensive results for both contexts.

Finally, chapter 8 summarises key results and suggests directions for future work.

2

Literature Review

2.1 Introduction

In this section we provide a review of the literature relevant to this thesis. We begin by examining the literature on context in single–view computer vision. This area is of great interest since many of the techniques may be transferable to our multiple–view setting. We then turn to a review of the use of context in robotics applications, a subject that has received somewhat sparse attention in the literature and has, as yet, no cohesive formulation or problem statement.

2.2 Context in Computer Vision

Over the past decade there has been renewed interest in the use of contextual information for computer vision tasks. There are many definitions of what "context" means and how to represent it. Here we review the dominant paradigms that have emerged around contextual reasoning in scene understanding. Many single–image contextual approaches have been targeted at a specific problem — namely that of object recognition — and while this is not aligned exactly with our own goal it is still instructive to review these contributions because the ideas they propose for inferring context are often separable from the specific task to which the authors choose to apply them.

2.2.1 Holistic Approaches

Gist Features

The work of Torralba *et al.* [67] has been very influential in expounding the value of contextual reasoning for vision. In their work, they compute a feature vector composed of statistics from the entire image and use this to reason about the contents of the image. This feature vector is termed the "gist" of the image and is computed as follows. First, an input image is passed through a bank of Gabor filters at n orientations and m scales, producing nm response images. Next, each response image is divided into a $k \times k$ grid. Finally the average over each grid cell is computed for each response image, and these values are concatenated to form the final feature vector of length nmk^2.

In early work, Torralba *et al.* used the gist vector to learn about scene categories. They showed that images could be classified into categories such as "road", "forest", and "bedroom" by applying a support vector machine (explained below) directly to the gist vector. In later work [67] they show how the location and scale of objects can be predicted from the gist vector. The Expectation–Maximisation algorithm [1] is employed to learn a mixture of Gaussians that relates the gist features to the probability of an object being present at various locations and scales. An example prediction is shown in Figure 2.1.

Support vector machines (SVM) were proposed by Vapnik [69] just over a decade ago and have since gained widespread support both inside and outside the machine learning community. SVMs learn to discriminate two classes by finding the separating hyperplane in feature space for which the distance to training examples is maximised.

The Expectation–Maximisation algorithm is a widely used tool for parameter estimation in the presence of unobserved variables [1]. Direct inference in such cases would require marginalisation over all unobserved variables, but the integrals involved typically make this approach infeasible. The EM algorithm overcomes this by iterating between two stages. First, the expected likelihood is computed with respect to the unobserved variables (the E–step), and second, the

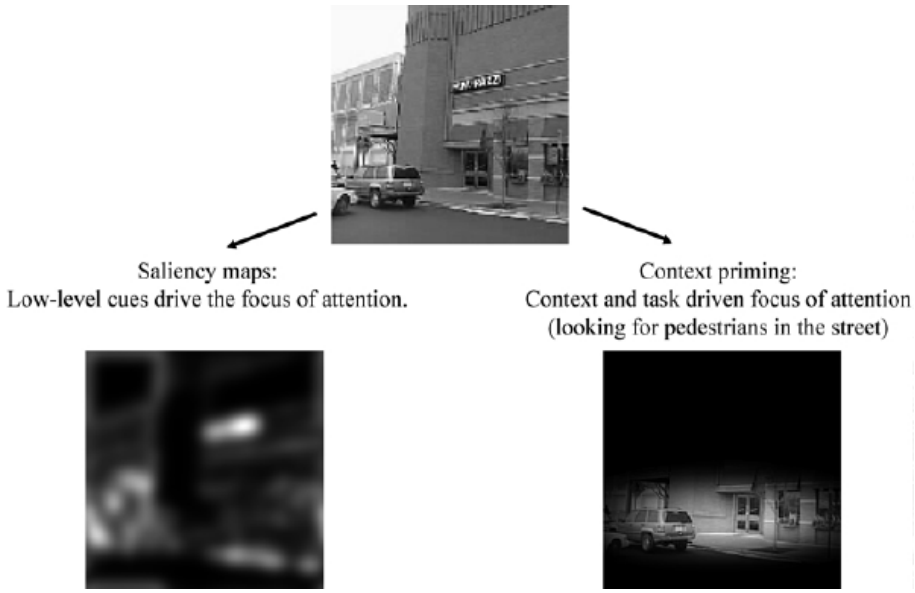

Figure 2.1: Torralba *et al.* [67] is able to improve upon traditional interest point detectors by learning the relationship between gist features and likely object locations. *Reprinted with express permission of Prof Antonio Torralba.*

model parameters are maximised with respect to the distribution computed in the first step (the M–step). These steps are repeated until convergence.

Scene Classification

Fei–Fei and Perona [18] classified images explicitly into semantic categories such as "coastal", "inner city", or "bedroom". Although their work focuses on the classification task itself, the output scene label is clearly a useful piece of contextual information for integration into a broader scene understanding system.

Fei–Fei and Perona represent an image as a bag of words, where the "words" are obtained by clustering SIFT features (explained below) obtained at regularly sampled locations across all training images. Once the codebook of words has been learnt, each image is collapsed to a simple sequence of integers representing the index of the codebook entries identified within it.

Analogous to document understanding approaches in which each section is associated with an inferred topic, Fei–Fei and Perona model a hidden "topic" variable for each image feature. In their model they also include a theme variable, which induces a class–conditional multinomial

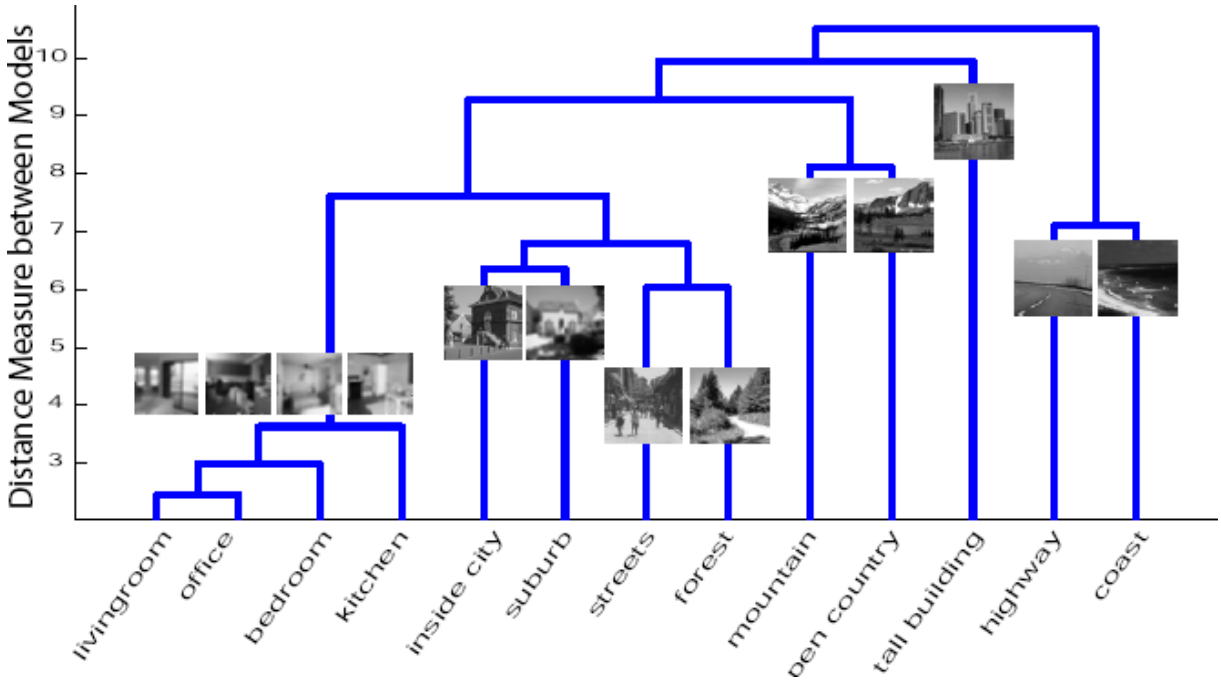

Figure 2.2: Dendogram showing the relationships between scene categories learnt by the system of Fei–Fei and Perona [18]. The model matches human intuition well. *Reprinted with express permission of Prof Fei–Fei Li.*

distribution over topics.

On a dataset of 15 scene categories, each with several hundred images taken from the web as well as from datasets released by other researchers, the system obtains an average classification accuracy of 64.0%.

The scale–invariant feature transform (SIFT) was first proposed by Lowe [47] for use in object recognition. Given some input image, SIFT generates a set of interest points and corresponding feature vectors that are robust to changes in lighting, scale, and camera viewpoint. To select salient features at a range of scales, SIFT builds a scale–space representation of the image [46] and selects locations that are well–localised in both the spatial and scale dimensions. Features are generated from a histogram over gradient orientations in a patch around each selected interest point.

2.2.2 Geometric Context

An explicit understanding of scene geometry can assist image understanding in numerous ways. Several authors have shown how to obtain coarse 3D reconstructions from a single image, which allows rich geometric reasoning for inference about such things as the objects and actions likely to occur within the scene, and the scale and position at which these might be found.

Pixel–wise Geometry Estimates

Hoiem *et al.* [35] approach geometric context as a per–pixel labelling problem in which the labels identify geometric properties of the 3D surface from which each pixel was captured. Although there are many 3D scenes that could have generated any particular image, Hoiem *et al.* note that some scenes are more probable than others given our knowledge of the world. To keep this difficult inference task tractable, the authors limit the pixel labels to "sky", "ground", and "vertical", the last of which is further sub–divided into "left–facing, "right–facing", and "front–facing". While there are some real–world scenes that cannot be represented by these geometric primitives, the authors show that they are able to model many useful and interesting types of scenes.

The authors take a machine learning approach to the reconstruction problem. First, the image is segmented into superpixels using the algorithm of Felzenszwalb *et al.* [20]. Next, pairs of adjacent superpixels are merged in order to gradually grow the small superpixels into larger regions. To do this, an affinity metric between adjacent superpixels is learnt using a boosted decision tree classifier, the input to which is a feature vector containing cues such as colour, texture, location, shape, and vanishing points. At evaluation time many different segmentations are generated by considering the superpixels in different orders. For each ordering, the first k superpixels are assigned to unique segments, then the remaining superpixels are assigned to the segment with which they have the greatest affinity. Each segment is classified into one of the geometric classes listed above using another a boosted decision tree classifier with the same

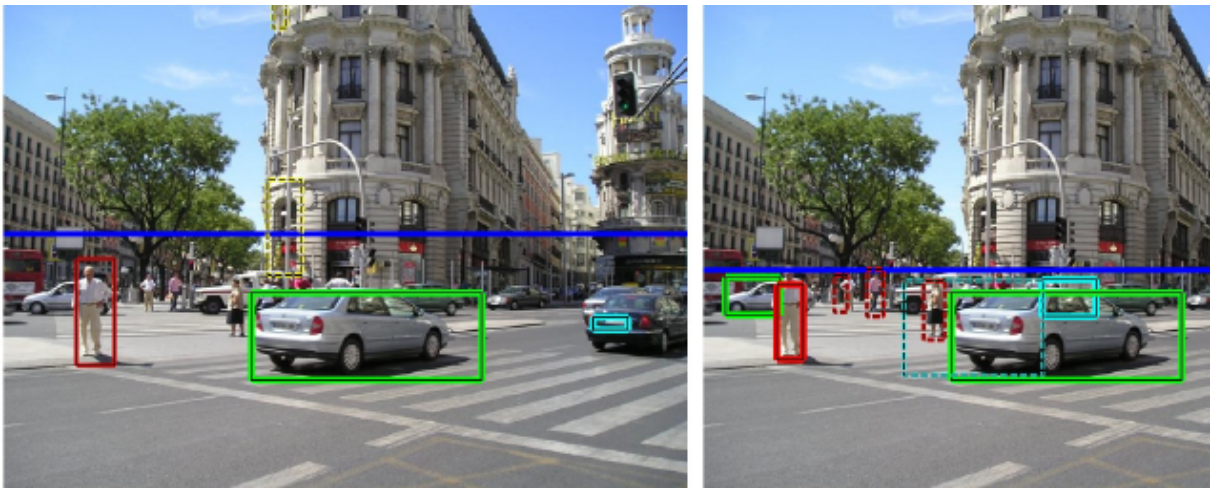

Figure 2.3: The left image shows car and pedestrian detections when using local features only. The right image shows detections when geometric context is leveraged: several false–positives are eliminated and several new correct detections are made. *Reprinted with express permission of Dr Derek Hoiem.*

input cues as for the affinity metric learning. Finally, superpixels are labelled according to the consensus vote amongst the segments to which they belong.

The authors further show that the geometric labels obtained in this way can be used as priors for object detection, since detections in unlikely places and scales can be suppressed, while those in geometrically consistent positions can be amplified. Figure 2.3 shows the improvement in detection performance resulting from the use of geometric context.

Make3D

Another approach to deriving geometric context has been proposed by Saxena *et al.* [58]. Rather than the fixed set of orientations employed by Hoiem *et al.*, Saxena *et al.* only assume that the scene is piece–wise planar. They allow these planar patchlets to take on arbitrary orientations, which they represent with a normal vector.

Saxena *et al.* apply a machine learning methodology to this problem. They begin by dividing the image into superpixels, each of which is associated with a feature vector containing the output of a set of filters, including colour, texture, and edges. Each superpixel also includes the features of neighbouring superpixels so that the inference process can reason in terms of

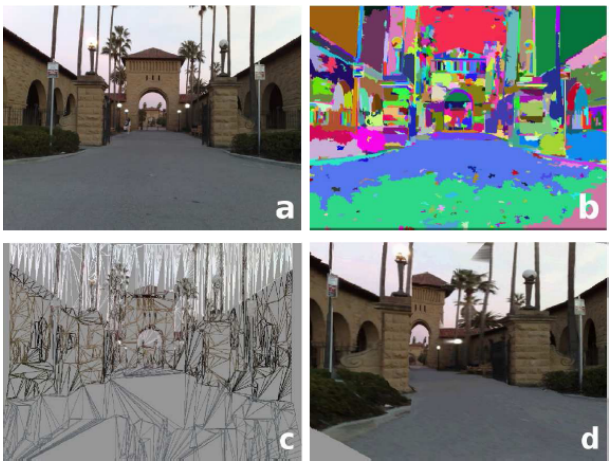

Figure 2.4: Results from the geometric context system of Saxena *et al.* [58]. From top left to bottom right the panes show (a) the original, (b) the superpixels, (c) the inferred 3D model, (d) a re–projection of the 3D scene. *Reprinted with express permission of Dr Ashutosh Saxena.*

broader image properties rather than local statistics alone. In addition, each superpixel boundary is associated with a separate set of features. These are generated by running segmentations based on different image properties and recording whether the boundary is present in each.

The superpixels are organised into a Markov Random Field (MRF), with edges between pairs that share a boundary in the image. The node potentials are learnt from the superpixel features and edge potentials are learnt from the boundary features. The authors allow for coplanar, connected, and disconnected relationships across boundaries, with the former preferred *a priori* over the latter. The MRF parameters are learnt through Multi–Conditional Learning and inference is performed by solving a linear program.

Within a dataset of 152 internet images the system was able to generate a qualitatively correct model (as judged by a human) 64.9% of the time. One such result is illustrated in Figure 2.4.

2.2.3 Manhattan–World Approaches

In recent years there has been growing interest in leveraging the Manhattan world assumption, in which a scene is modelled using surfaces oriented in three mutually orthogonal directions. This idea was originally proposed by Coughland and Yuille [12], who were interested in recovering camera orientation from a single image. It has since been used in a variety of tasks

including vanishing–point detection [42], single–view reconstruction [43, 21], and multiple–view reconstruction [26, 24]. In general, the Manhattan world assumption is appealing for scene understanding tasks as it reduces the size of the hypothesis class one must search over.

Cuboid Models

Hedau *et al.* [31] reason about indoor environments by modelling the scene as the interior of an axis–aligned cuboid. This is perhaps the simplest possible instantiation of the indoor Manhattan assumption, but the authors show that even this restrictive model can be helpful when interpreting and recognising objects in photos of indoor environments. Their approach proceeds in two stages. First, three mutually orthogonal vanishing points are estimated from observed line segments. Next, a cuboid is identified by casting two rays from each vanishing point.

The authors use a structured prediction model to learn how to select bounds for the cuboid. Given training examples they train an SVM to rank cuboid hypotheses within a feature space defined over inputs (image features) and outputs (cuboids). This approach follows a similar methodology to the approach we propose in Chapter 7, though we learn within a much more general hypothesis class.

In later work [30] the authors connect the cuboid model of spatial boundaries to a model of objects within the room. Objects are modelled as axis–aligned cuboids resting on the floor. Several such cuboids are hypothesised, and the support for each is determined by an SVM trained with HOG features. The authors further show that by reasoning jointly about room boundaries and the objects within, the performance of both inference algorithms is improved.

Indoor Manhattan Scenes

Lee *et al.* [43] have investigated geometric context for the special case of *indoor* Manhattan environments, which are a sub–class of general Manhattan environments and have the following properties:

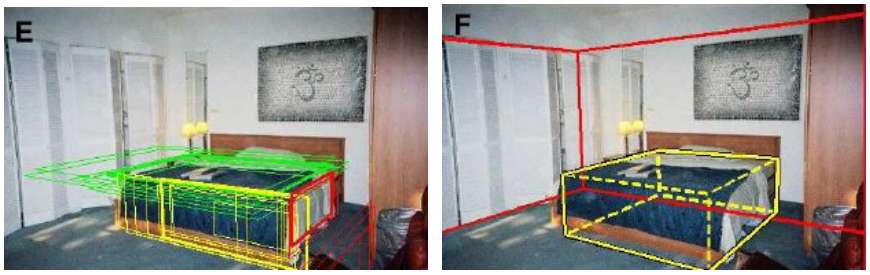

(a) Object hypotheses (b) Scene layout and object boundary

Figure 2.5: Results from the cuboid model of Hedau *et al.* [31, 30]. *Reprinted with express permission of Varsha Hedau.*

- There is a floor plane and a ceiling plane, which are parallel to one another and extend indefinitely in all directions.
- There are planar wall sections, which are orthogonal to the floor, extend all the way from the floor to the ceiling, and terminate in vertical boundaries.
- The wall sections are oriented in one of two mutually orthogonal directions.
- Many objects within rooms are aligned with the floor and/or walls and hence there will be many edges sharing vanishing points with floor, walls, and ceiling.

Although many real environments contain exceptions to these rules, the authors argue that their model is expressive enough to represent approximately or exactly many real–world scenes. This leads to a particularly simple model in which scenes are represented by a ground plane orientation and a set of wall segments.

Lee *et al.* show how such a model can be derived from a single image. They begin by sampling two pairs of lines in a RANSAC–like fashion to generate vanishing points. Each pair is checked for mutual orthogonality (using a prior on camera focal length) and for support amongst the other detected line segments. The intersection of the two pairs gives two vanishing points, from which the third can be derived. This results in a set of straight lines and their associated vanishing points.

The authors show that, given the assumptions above, any set of lines representing wall segments for which the associated vanishing points are known either give rise to exactly one Man-

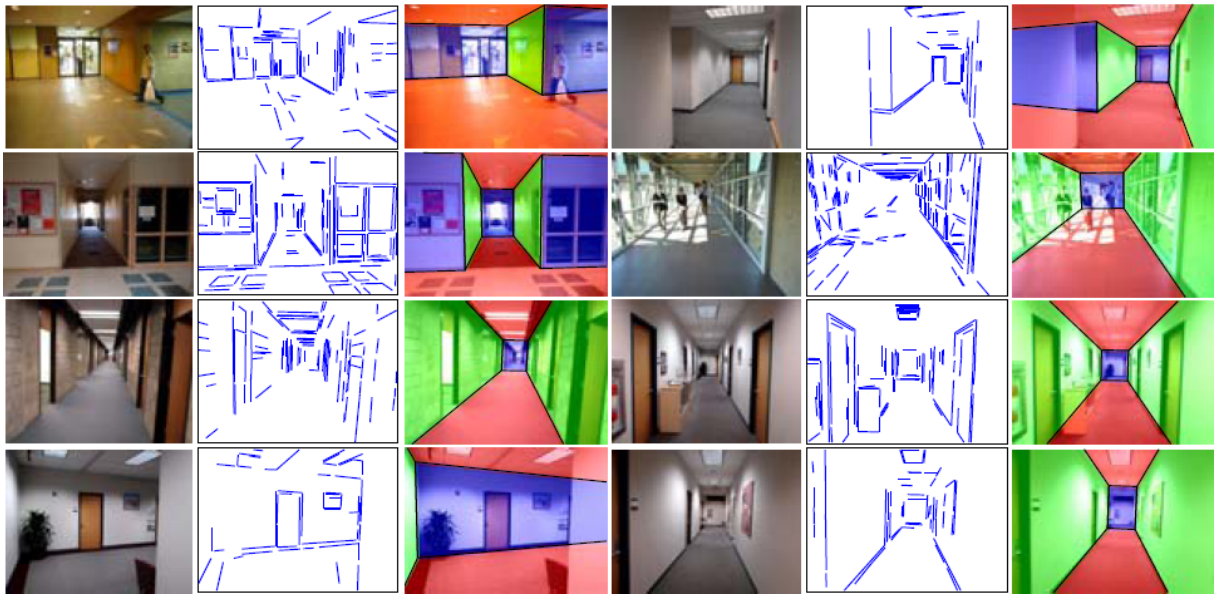

Figure 2.6: Inferred scene structure obtained for single images by Lee *et al.* [43]. Each triplet shows the original image, the detected line segments, and the final scene geometry. *Reprinted with express permission of David Lee.*

hattan world model or violate a set of easily–checkable rules. They therefore proceed to enumerate all valid hypotheses by running a branch–and–bound search over all combinations of line segments. This remains tractable because the validity check eliminates most combinations at an early stage of branching. Of the valid hypotheses, they choose the one which is maximally consistent with surface orientation estimates separately inferred from the image. Figure 2.6 shows some of the building structures their system was able to infer.

The second half of this thesis is concerned with models in this category.

Oriented Plane Sweeps

Gaullup *et al.* [27] present a fast stereo algorithm based on plane sweeping with respect to Manhattan–like surface orientations. They proceed by (1) selecting a vertical direction based on the camera trajectory; (2) identifying one horizontal and several upright surface orientations based on lines and estimated vanishing points; (3) performing plane sweep stereo with respect to each of these orientations; and (4) fusing the result into a depth map. The resulting depth map naturally encodes Manhattan scene structure since each pixel is implicitly associated with

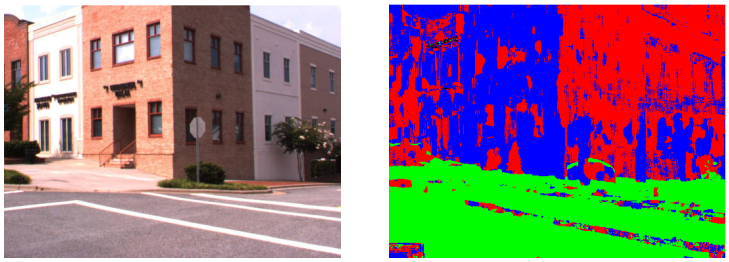

Figure 2.7: Manhattan–like scene structure obtained from the multi–way plane sweep approach of Gallup *et al.* [27]. *Reprinted with express permission of David Gallup.*

one of the upright or horizontal orientations.

Manhattan World Stereo

Furukawa *et al.* [26] used the Manhattan world assumption to improve the robustness of multiple–view reconstruction. Large textureless surfaces are common within indoor environments — for example walls, ceilings, and floors. Such regions challenge many 3D reconstruction techniques since identifying correspondences between views is challenging. To overcome this, Furukawa *et al.* built a 3D reconstruction system that leverages the Manhattan world assumption to extrapolate the layout of textureless regions from constraints imposed by edges and corners, which are easier to localise in multiple views. They model this task as an energy minimisation problem in which each pixel must be labelled as belonging to some axis–aligned plane. A smoothness prior ensures that system chooses the simplest arrangement of planes that match the observed image evidence.

Blocks World

As early as 1965, Roberts [57] proposed building scene representations up from cuboid building blocks. This idea has recently been revisited using modern probabilistic techniques by Gupta *et al.* [28]. Beginning with an empty ground plane, the authors iteratively add cuboids to explain image features such as corners and edges. Utilising a variety of stability and visibility constraints the authors show that they are able to model a variety of scenes.

(a) Input image (b) Inferred scene structure (c) 3D rendering

Figure 2.8: Results from the blocks world model of Gupta *et al.* [28]. *Reprinted with express permission of Dr Abhinav Gupta.*

Vertical Structure Priors

Zeisl *et al.* [75] improve upon traditional stereo algorithms by constraining reconstructions to a pair of horizontal planes (floor and ceiling) spanned by arbitrary vertical surfaces. Similarly to the algorithm we present in Chapter 6, they use dynamic programming for exact inference within their model. One difference between their approach and the one taken herein is that they permit arbitrary vertical surfaces, not just manhattan–oriented planes, and they penalise overall model complexity in a different way. We discuss the connection between this approach and our own, and given an empirical comparison in Chapter 6.

Horizontal/upright Models

Delage *et al.* [15] presented early single–view reconstruction work that focussed on identifying the boundary between horizontal and upright surfaces. They modelled this floor/wall fracture as a dynamic Bayesian network over image pixels, for which efficient dynamic programming inference algorithms are well known.

Barinova *et al.* [3] adopt a Manhattan–like hypothesis class for outdoor scenes. Their models consist of a ground plane supporting a series of vertical facades, which they infer using a conditional random field over pixels. The key inference problem in their approach is to recover a polyline separating the ground plane from the series of vertical facades. They use a standard Expectation–Maximization algorithm for maximum–likelihood inference, and

component–wise logistic regression to learn the CRF parameters from training data.

Felzenszwalb and Veksler [19] discuss a class of dynamic programming algorithms capable of maximum–likelihood image segmentation under various shape priors. One of the applications to which they apply their algorithm is single–image reconstruction.

Common to each of these approaches is a model that decompose into vertical segments running from left to right in the image. We take advantage of a similar decomposability within indoor Manhattan environments in the inference algorithm that we propose in Chapter 6.

3D stages

Nedovic *et al.* [52] derive geometric context by classifying images into 15 "stage categories". Each category consists of an arrangement of surfaces such as "ground", "sky", "upright", "background", and "figure", such as those shown in Figure 2.9. Their principal contribution is a large selection of powerful visual features containing salient geometric information, including cues derived from color, shape, texture gradients, atmospheric scattering, line segments, and segmentation boundaries. The authors train an SVM to associate input images with one of the 15 stage categories.

Their work relates to ours as follows. 13 of the 15 proposed stages are special cases of indoor Manhattan environments, which we analyse extensively in this thesis. The remaining two include an upright "person" segment, which we do not consider. The learning scheme we propose in Chapter 7 is also based upon large margin principles, but whereas Nedovic *et al.* learn with respect to 15 categories, we learn with respect to the much larger space of all possible indoor Manhattan models. The features they propose seem well suited to our own purposes and so future work could apply our inference and learning strategies to their features.

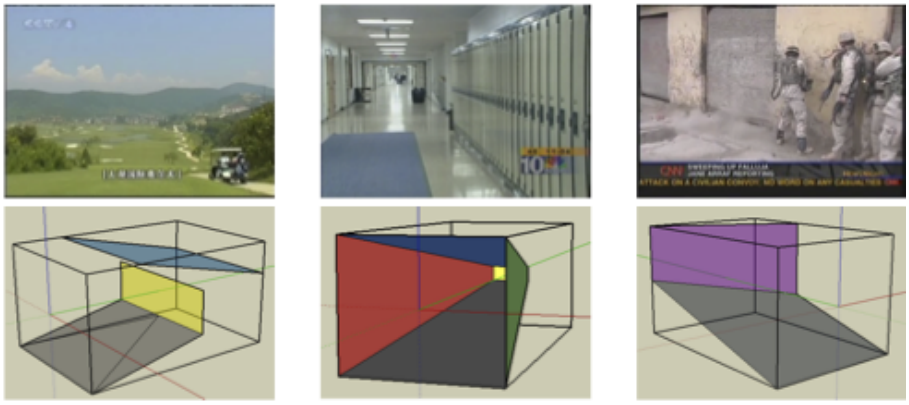

Figure 2.9: Three categories of "3D stages" defined by Nedovic *et al.* [52], with examples of representative images. *Reprinted with express permission of Vladimir Nedovic.*

2.2.4 Texture Recognition

Heitz and Koller [32] derived context from texture structure in images. Their model relates the presence of objects, which have specific boundaries, to the appearance of the nearby surfaces and foliage, which have no crisp notion of spatial support. This approach is motivated by the observation that object positions correlate with the appearance of their surroundings. For example, cars and bikes are likely to appear near road–like texture, whereas aeroplanes are likely to appear against a sky–like background.

They begin by identifying superpixels using the segmentation algorithm described by Ren and Malik [55], which is extends the normalised cuts algorithm due to Shi and Malik [61] . Each such region is associated with a feature vector comprising various colour and texture statistics, which, in their model, arises from a latent category variable, the intention being that superpixels will be clustered into meaningful groups like "road" and "sky". Meanwhile, a set of candidate object detections is generated by invoking a standard object detector and taking all detections above a certain threshold. The "things" are related to the "stuff" by a set of observed variables representing spatial relationships such as "above", "beneath", and "next to".

An advantage of the this model is that while object labels are required for training, no explicit segmentations or labels are required for the system to learn how to categorise the "stuff" regions since the system is capable of learning these unsupervised. The authors achieve this using the EM algorithm, which iterates between estimating the superpixel labels and optimising

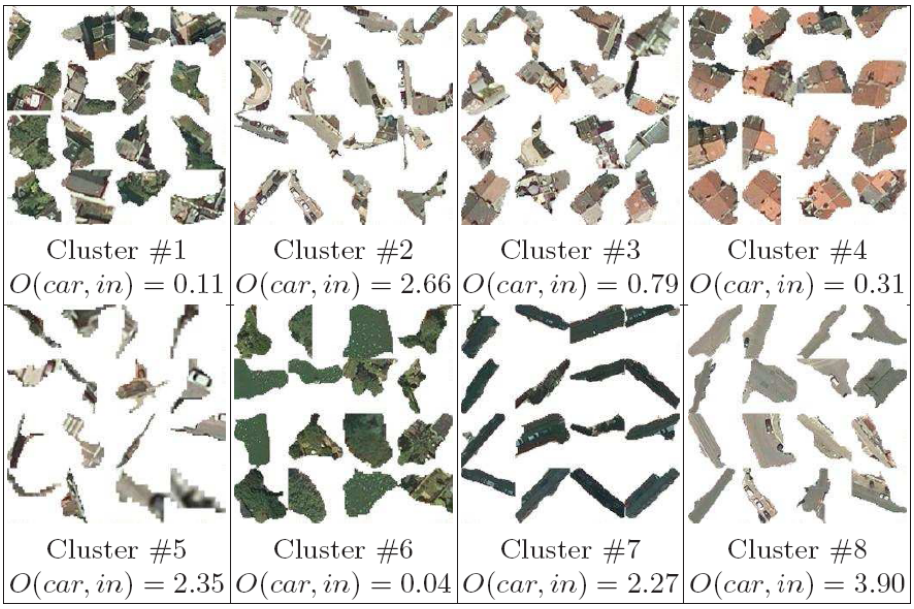

Figure 2.10: Superpixels clusters generated by the model of Heitz and Koller [32]. Shown below each panel is the odds ratios for a car appearing near a superpixel from that class. The odds ratio is higher for road–like regions than for foliage– or water–like regions. *Reprinted with express permission of Prof Daphne Koller.*

the appearance parameters for each label.

The authors also show how to learn a set of relationships that best describe the dependencies between objects and their surroundings. This involves augmenting the EM algorithm with a greedy search over possible relationships, iteratively adding the best candidate out of a pre–defined pool until convergence. This allows the system to adapt to the most salient relationships for a specific problem, which will differ between, say, images captured from satellites and the photos in the VOC datasets [17]. During evaluation both the object labels and superpixel labels are unknown, so exact inference is intractable. Instead, the authors use an approximate inference technique called Gibbs sampling. Figure 2.10 shows some example superpixel clusters along with their probabilistic relationship to car detections.

2.3 Context in Robotics

Cameras have long been recognised as a valuable sensor for mobile robotics. In addition to visual SLAM, cameras have been used in robotics tasks such as place recognition [14] and

scene description [54]. Contextual reasoning has received little attention from the robotics community. This section reviews the literature that does exist on this topic. We divide the work into two categories: map–centric approaches, which integrate sensor data into a map and then reason from this representation, and ego–centric approaches, which organise sensor data as a time–indexed series of observations.

2.3.1 Ego–centric approaches

Martinez *et al.* [51] have demonstrated that a robot can learn to classify its environment into semantic categories such as "corridor" or "room" based on simple range data features. They employ a SICK laser, which gives a 360° scan of the scene within a single horizontal plane. They collect features such as the distance between successive beams, the average beam length, and the eigenvalues of the polygon formed by the beam endpoints, which are concatenated to form a feature vector at each time step.

To relate these features to semantic categories, the authors employ the AdaBoost algorithm [56] using linear classifiers as the weak learners. AdaBoost is a popular classifier that learns by incrementally adding rules that maximally correct the mistakes it has made so far. Martinez *et al.* show that they are able to differentiate rooms, corridors, and doorways at 89% accuracy using this method. Furthermore, in environments that have not been seen before the system obtains 82% accuracy. The results for one environment are depicted in Figure 2.11.

Stachniss *et al.* [64] extends this to use visual cues from a panoramic camera in addition to the laser range data. Stachniss runs an off–the–shelf object detector for each of several object categories that correlate well with location. The chosen objects include computer monitors, coffee machines, and soap dispensers. At each time step, the robot's current location is categorised using the same AdaBoost classifier as described above, the only difference being that now the number of visual detections of each object type are appended to the AdaBoost input vector. This allows the classifier to select between visual and range data features (or combinations thereof) according to whichever is most salient for the task at hand.

Figure 2.11: Semantic labels assigned by the range data classification system of Martinez *et al.* [51]. 82% of places were correctly classified, despite the environment not having been seen during training. *Reprinted with express permission of Dr Oscar Martinez Mozos.*

The authors recognise that the robot's location is highly correlated over successive time steps and so model the robot's state as a Hidden Markov Model (HMM), with the transition probabilities estimated empirically. Stachniss *et al.* show that the addition of visual cues allow them to differentiate between rooms with a similar shape but different visual appearance (such as bedrooms and living rooms), whereas the original range–data–only approach of Martinez would fail in this case.

Posner *et al.* [54] show how to learn semantic labels such as "grass", "foliage", or "wall" for regions within urban environments. Like the systems described above, they reason from a combination of laser and vision features, including colour, location, and orientation properties. Unlike previous approaches they perform a quantisation step to form feature "words".

Incoming images are segmented based jointly on an off–the–shelf superpixel algorithm and continuity boundaries in the laser data, after which the problem is reduced to determining the appropriate label for each segment. They relate the features for each region to semantic labels using a graphical model that incorporates observation likelihoods as well as a sensor model describing the probability of false positive and false negative observations. While a standard

Figure 2.12: Semantic labels output by the system of Posner et al [54]. *Reprinted with express permission of Dr Ingmar Posner.*

approach would be to assume independence between the feature observations for tractability, the authors note that the observations are far from independent in reality and instead employ the Chow Liu algorithm to find the best tree–structured approximation to the full joint distribution. Inference within this model is performed by computing the full posterior over labels.

Posner *et al.* further refine the labelling by relating the labels of neighbouring patches in an MRF framework. They introduce edges for both spatial and temporal consistency, the former being derived from adjacency between segments within the image, and the latter being derived by reprojecting laser points into consecutive frames. Node potentials are given by the segment classifier described above while edge potentials are learned empirically from hand–labelled training data. Sequential tree–reweighted message passing (TRW–S) is chosen for inference within the MRF due to its efficiency guarantees.

The authors show that their system is able to accurately label a range of outdoor environments with 8 categories (grass, tarmac, dirt path, textured wall, smooth wall, foliage, vehicle). Their classifier obtains the highest precision for the "grass" category (95.5%) and the lowest for "vehicles" (79.7%). Furthermore, their system is able to run in under 4 seconds, which is suitable for periodic on–line operation. An example labelling is illustrated in Figure 2.12.

2.3.2 Map–centric approaches

An alternative approach to deriving context in robotics applications is to integrate new measurements into a map, and then reason about semantics within the map representation. In general this approach enables stronger integration of measurements taken over several time steps, at the cost of relying on the ability to correctly build a map.

Buschka and Saffiotti [8] have taken a map–centric approach to the problem of identifying room boundaries within indoor environments and recognising the resultant rooms. A series of laser range scans are fused into a 2D occupancy grid representing the probability that each cell is occupied by some object or boundary. Rooms boundaries are identified by applying dilation and erosion to the occupancy map, which are standard morphological filters from visual segmentation [25]. The authors demonstrate that this can be performed with fixed computational cost by discarding old parts of the environment as the robot moves through the environment.

The result of their algorithm is a series of "nodes" with topological connections between them, which correspond to the various rooms and corridors within the robot's environment and the doorways that connect them. The authors proceed to characterise each node by the size and eccentricity (length to breadth ratio) of its bounding box. This gives contextual information in two senses: firstly, the identification of room boundaries allows reasoning in terms of rooms rather than the entire known environment, and secondly, the characterisation of room shapes allows differentiation between rooms and corridors and thus allows different interpretations of sensor data in these semantically distinct workspaces.

Vasudevan *et al.* [72] use an alternative map representation based around the location of objects. They argue that this matches human perception of space. In their maps, each "object" (actually a SIFT landmark) occupies a separate coordinate frame, with uncertainty represented in the transformations between frames.

They identify doorways by running a line detector and testing various combinations of lines against a set of heuristics, enabling separation of the constituent rooms within an environment. This in turn allows per–room reasoning as was the case with the Buschka and Saffiotti system

described above. The difference here is that Vasudevan *et al.* identify doorways directly from visual input whereas Buschka and Saffiotti use occupancy maps.

Vasudevan *et al.* show that this representation leads naturally to reasoning about place context. They argue that place categories (bedrooms, kitchens, bathrooms, *etc.*) can be identified by the objects within them, and hence that their object–centric maps provide the perfect setting for this form of contextual reasoning. Formally, they learn a class–conditional object likelihood by computing the number of times each object is observed in each type of places versus the total number of times the place category has been observed. They then assume independence between object observations and compute the posterior over place categories by multiplying out the likelihoods for each observed object.

2.4 Conclusions

Modern structure–from–motion systems generate accurate metric maps of an environment, and can do so robustly and efficiently using visual input alone [40]. The problem of deriving high–level semantic context from such sensor data has been approached by several authors. Although there is not yet a widely agreed–upon problem formulation, current work in this area shows that semantics are important for many robotics applications, and can be derived from a range of sensor types. Important contributions include that of Martinez [51] and Stachniss [64], who show that place categories can be obtained from photometric and geometric cues, and Posner [54], who shows that scene regions can be associated with semantic categories, again by combining vision and range sensors.

The contextual reasoning problem for single–image vision has received comparatively greater attention. Torralba's seminal gist descriptor [67] has led to the development of many types of contextual cues, including geometric [34, 58], textural [32], and model–based [43] approaches. Our work is motivated largely by the success of the single–image approaches discussed above; in this thesis we show how to extend these ideas to incorporate a moving camera and the geometric information that a SLAM system provides.

3

Appearance–Only Context Models

This chapter explores an approach to scene understanding that relates low–level image information directly to high–level variables describing scene categories and coarse geometry. We build on a well–known texture analysis approach in which pixels are identified with characteristic texture units known as textons. Extending previous work in texture analysis and image recognition, we show that this approach — which has previously been applied to recognition of uniform textures — extends to high–level scene understanding problem in which the input image is composed of many objects and surfaces. We propose a novel recognition model in which we measure the displacement between texton occurrences in an image rather than their absolute location or overall frequency. We apply our ideas to two classification tasks: place recognition and camera orientation classification. Comparisons with the gist descriptor of Torralba *et al.* show superior performance on both tasks.[1]

[1]This work was published in part in:
Flint, Murray, and Reid, "Learning Textons For Real–Time Scene Context", in *Proceedings of the First International Workshop on Ego–Centric Vision, 2009*[23]

3.1 Introduction

One important aspect of scene understanding is the ability to differentiate between logical areas within an environment, such as rooms in a house. This problem is important in the domain of augmented reality because knowledge of the location of a user will give a strong indication as to the activities the user might undertake and the objects with which they are likely to interact.

Outside this specific application area, place recognition can be used as a generic source of context for further scene understanding tasks. Object recognition, semantic segmentation, and semantic reconstruction are all likely to benefit from a prior on place categories, since such information would correlate well with the location of objects, the function of surfaces, and the geometric structure of the environment.

The place recognition problem we propose in this chapter associates many images of a logical region — rooms within a house in our case — with a single place category. This means that there may be image pairs observing no common 3D locations, yet are associated with the same category, and hence the system will be expected to recognise them as associated with the same logical place. We also tackle the problem of identifying the approximate tilt of the camera from a single image. This problem requires the categorisation of images into 3 categories: "upwards–facing", "downward-facing", and "straight-facing".

We pursue an approach motivated by the texton model developed by Julesz [38] and introduced to the computer vision community somewhat later [76]. We show that low–level texture elements can be related to the high–level variables of interest to us, and that doing so yields state–of–the–art results for both scene understanding problems.

The remainder of this chapter is organised as follows. First we introduce the notion of textons, which form the basis of our approach. Next we motivate the use of textons for scene understanding problems in general by exploring the relationship between textons and scenes. We then describe our probabilistic model relating textons to place recognition and camera classification in detail. Next we present an empirical comparison between our system and the gist descriptor of Torralba *et al.*, followed by discussion and concluding remarks.

3.2 Background

The notion of textons as atomic texture elements was born in the neuroscience community when in 1981 Julesz [38] introduced textons as part of his theory of human visual attention. Julesz defined textons as elongated blobs, line terminators, and line intersections. Several researchers have proposed definitions of textons for use in computer vision applications (see [76] for an extensive discussion), including both topological and statistical descriptions. We follow the statistical account first proposed by Malik *et al.* [49]. Under this definition, an image is passed through a filter bank, producing a set of response images. Each pixel is then associated with a feature vector that contains each filter's response for that pixel. The feature vectors are then clustered and the resultant cluster centres become the texton exemplars.

At evaluation time the input images are passed through the same set of filters, and each pixel is again associated with a feature vector containing the filter responses at that point. Next, each pixel is labelled according to the index of the texton exemplar (from the training phase) closest to it in the L2 sense. The image is henceforth represented as an array of texton indices (the "texton map"); the remainder of the image data is discarded.

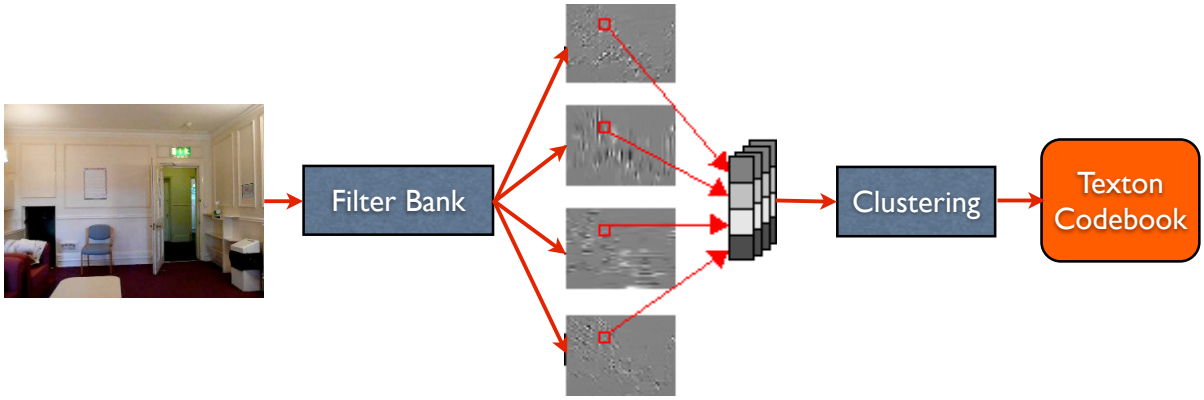

Figure 3.1: The texton generation process.

In the past textons have been successfully used to classify close–up photos of materials such as wood, paper, and glass. Varma and Zisserman [71] tackled this problem using the texton model discussed above. After forming the texton map they proceed by counting the occurrences of each texton, with the resultant histogram over texton frequencies forming the model

by which input images are matched to their category. In their work, Varma and Zisserman apply a nearest neighbour approach to classify the models, using the χ^2 statistic to measure distances. Representing data by a histogram over quantised features in this way has since become known by the terminology "bag–of–features" or "bag–of–words".

3.3 Textons for Scene Understanding

Textons are a widely used and well–understood within the computer vision community [76, 71, 49]. However, their use has mostly been limited to low–level image analysis tasks, such as texture classification. We propose to use textons as the basis for high–level reasoning tasks including scene classification. In the remainder of this chapter we will develop a novel model by which to utilise textons during inference. We begin in this section by motivating the use of textons for this application.

Many place recognition systems rely upon an interest point detector and descriptor to summarise input images [18, 14]. This has proven effective for outdoor environments as well as indoor environments that contain reasonably distinctive landmarks. However, these systems are fundamentally limited to a feature–centric view of the world in which only local information about interest points is utilised.

We believe that there is un–leveraged information in the texture structure within images, and that this can be used for scene understanding tasks such as place recognition. Many images of indoor scenes contain extremely poor visual information, particularly small, empty environments like corridors and foyers. Figure 3.2 shows some examples of these. Yet despite this information poverty, humans are capable of deducing much from these images. For example, consider the image at the right of Figure 3.2: there is barely one location here that would yield a useful SIFT feature, yet a human can identify the part of the environment that the image represents (a corner between wall and ceiling), and a human familiar with the environment can easily identify the room in which the image was captured. We think it is clear that, in this case, humans are using a holistic understanding of the image in which the edge structure together

with the texture of the surfaces is used to understand the image. We propose to use textons to leverage this valuable information.

Figure 3.2: Frames with low visual salience.

To investigate whether textons provide useful information about scene structure, we collected video sequences of an indoor environment and examined the textons generated by the algorithm described above. Our dataset consisted of $10,555$ frames from 5 rooms in a hostel. Some qualitative findings are described in the following sections.

3.3.1 Textons Select Salient Image Elements

Figure 3.3 shows 25 textons generated for this dataset, in order of their frequency of occurrence. The first 7 correspond to untextured regions of the image — *i.e.* patches with near–uniform intensity. This is expected since the majority of pixels lie within object or region boundaries, where either the texture is too fine for the camera to detect (a carpet, for example) or there simply is no texture (a white wall, for example).

The next most frequent textons are those corresponding to edges and bars at various orientations. Many image understanding algorithms explicitly employ a line detector [25], whereas in this case the use of textons has allowed the system to learn to identify these elements unsupervised.

At the other end of the frequency distribution, the least numerous textons are those corresponding to image structures such as junctions and line endpoints. These structures are also sought explicitly in many image understanding algorithms [25], whereas the use of textons selects these structures automatically and unsupervised.

Figure 3.3: Textons identified for our dataset during the offline training stage. Each panel shows a representative image patch for one of the cluster identified by K–means. The patches were selected by identifying the feature closest to each cluster centre, and then extracting a small patch about the image position from which it arose. The textons are sorted by decreasing frequency from top to bottom, left to right. Image patches are converted to grayscale before filtering, but here we show them in colour to assist visualisation. The patches vary in size due to clipping near image boundaries (this does not affect clustering).

3.3.2 Textons Focus Attention on Salient Image Regions

Figure 3.4 shows the frequency of each texton within our entire dataset. The most frequent textons at the left of the graph account for a disproportionately large number of pixels, whereas the textons towards the right account for a tiny minority. We have just seen that it is precisely these minority textons that correspond to the image elements that are most useful in image understanding, so in this sense the use of textons has automatically focused attention on the small fraction of pixels representing the most salient image structures.

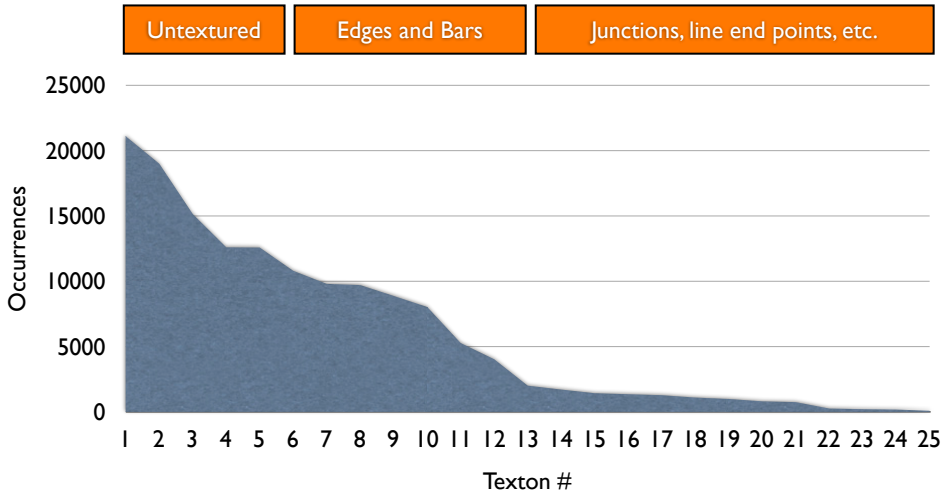

Figure 3.4: Frequency distribution of textons. The texton generation process assigns more textons to describing salient but rare image structures such as junctions and line end points than it assigns to frequent but non–discriminative image regions such as textureless patches.

3.3.3 Textons Correlate With Scene Structure

To further explore the relationship between textons and scene structure we divided all frames within our dataset into three orientation categories: "straight" (for which the camera's optical axis was within $\pm 22.5^\circ$ of the horizontal), "up" (above 22.5°), and "down" (below 22.5°). Next we computed an average occupancy map for each texton within across each category. Several per–texton heat–maps are shown in Figure 3.5. The first two rows show heat–maps for textons that correspond roughly to "floor" and "wall/ceiling". We can see that these reflect the image regions in which we would expect to find these scene parts given the various camera

orientations.

Perhaps the most instructive example of the texton/scene structure relationship, however, is that of the textons that represent edge elements, two of which are shown in the lower two rows of Figure 3.5. Consider the third row in this figure: The stratification evident in the heat–map for downward–facing frames indicates a common intersection somewhere above the image, whereas that for the upward–facing frames indicates an intersection below the image, and in the forward–facing frames the lines are close to parallel. This, of course, is exactly what we would expect from our understanding of projective camera geometry, but here our system has automatically and without supervision captured these geometric constraints (or at least some statistical form of them).

These illustration are simply indications that textons might provide salient information of value for scene understanding. We describe our model that explicitly relates these to each other in the next section.

Figure 3.5: Four example textons generated unsupervised for the camera orientation classification problem. From top to bottom the textons represent roughly "wall or ceiling", "floor", "vertical edge", and "horizontal edge". The six columns on the left show examples of where the texton was found. The three columns on the right show the average occupancy map over our dataset for images taken from an upwards–facing, horizontal, and downwards–facing camera (from left to right in the figure). The layout of the textons correlate strongly with camera orientation, which illustrates how our system is able to distinguish between camera orientations based on texton layout.

3.4 Learning and Inference

Having motivated the use of textons for image understanding we now describe our probabilistic model that relates textons to scene categories. For an input image I, we wish to discover the associated place category c. For each category we are given a set of example images at training time. We wish to model categories c according to the pixel locations in which textons appear within images associated with each category. One popular approach is the bag–of–features model [37] but this would remove all information about the locations of the textons, which as we have seen is a principal source of salient information. Instead we propose a new bag–of–texton–pairs model in which an image is represented as a collection of observed texton pairs $\{(t_i, t_j, s_{i,j})\}$ where t_i and t_j are texton labels and $s_{i,j}$ is the displacement between the image locations at which they were observed. By considering only displacements and not absolute pixel locations in our model we gain some robustness to camera orientation.

For an image I containing N pixels there are N^2 such pairwise observations. Our class–conditional likelihood is

$$P(I \mid c) = \prod_{i=0}^{N} \prod_{j=0}^{N} P(t_i,\ t_j,\ s_{i,j} \mid c) \tag{3.1}$$

where we have assumed independence between observations for tractability. We compute the likelihood (3.1) by estimating the joint distribution $P(t_i, t_j, s_{i,j}, c)$ using a histogram. We could have used Parzen windowing [53] for the continuous variable $s_{i,j}$ but due to the very large number of samples we obtain for each image, we found this to be unnecessary.

For images of reasonable size the cost of enumerating all N^2 texton pairs is prohibitively expensive. We overcome this by overlaying an $M \times M$ grid on the image and counting the occurrences of each texton within each grid cell. We then enumerate all pairs of grid cells and evaluate the texton pairs in aggregate. Hence for grid cells C_a and C_b containing n_i^a and n_j^b instances of texton t_i and t_j respectively, we evaluate $n_i^a n_j^b$ instances of the observation $(t_i, t_j, s_{a,b})$ where $s_{a,b}$ is the distance between the centres of the grid cells. We have lost some precision in the texton locations since each texton is effectively moved to the centre of the grid cell containing it, but our experiments show that we are still able to capture sufficient salient information. We also

note that quantizing displacements in this way implicitly shares information between similar displacements. One could think of this operation as an efficient approximation to building the full joint distribution and then smoothing along the displacement axis.

During training we evaluate these aggregated observations by multiplying the entry we make in the histogram by $n_i^a n_j^b$, and during evaluation the aggregate observations correspond to multiplications in the class–conditional log likelihood

$$\log P(I \mid c) \quad = \quad \sum_{a=0}^{M^2} \sum_{b=0}^{M^2} \sum_{i=0}^{K} \sum_{j=0}^{K} n_i^a n_j^b \log P(t_i,\ t_j,\ s_{a,b} \mid c) \tag{3.2}$$

In both cases the aggregated observations can be evaluated in a single step so the complexity is reduced from $O(N^2)$ to $O(M^4K^2)$. In practice we found that setting $M{=}8$, $K{=}25$ was sufficient to capture much of the salient image information, while allowing our system to run at video frame rate.

3.5 Place Recognition

We applied our system to the problem of place recognition. Our data set consisted of several video sequences captured in a hostel using a low–quality camera with a resolution of 320×240, which moved rapidly with the user's upper body. The sequences involved frequent motion blur and rapid variations in camera orientation.

We labelled each frame with the place that it was captured in. There were five labels: bedroom, kitchen, common room, garden, and corridor. We gave all frames captured in corridors the same label. This experiment does not correspond to place *category* recognition since most of the labels included frames from only one place instance. However, it is harder than strict landmark–style localisation because, as shown in Figure 3.6, many images with the same label contain non–overlapping views of the room they were captured in, yet the system is expected to recognise all of them as belonging to the same place.

We compared our system with the gist descriptor of Torralba *et al.* and a K–nearest–neighbours

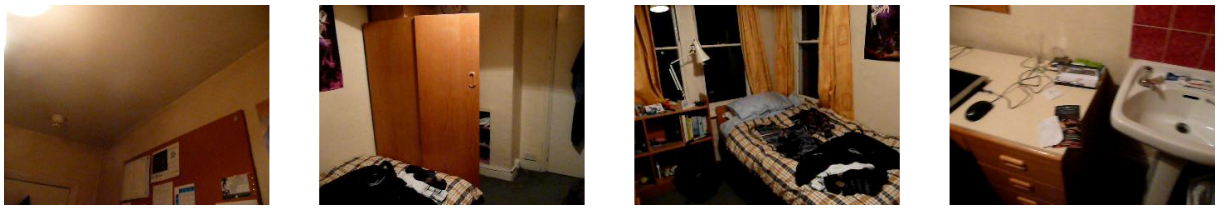

Figure 3.6: Four frames with the "bedroom" label. There are almost no overlapping scene parts but the system is required to (and did successfully) recognise each of them as part of the same place.

baseline, using vectorised grayscale images as feature vectors for the latter. For the gist descriptor we used the same Gabor filter bank that we used in our own system and we estimated the class–conditional likelihood in feature space by building Gaussian mixture models with the Gaussians constrained to be spherical, exactly as described in [67].

Initially we used 230 frames for training and 490 frames for evaluation (our training and evaluation sets were taken from separate sequences). The results from this experiment are shown in the middle row of Table 3.1 and in Figure 3.7. Our system outperformed Torralba's by a large margin. We suspected that the poor performance of Torralba's system was due to the training data not sufficiently populating the 32–dimensional feature space. This exemplifies one of the major advantages of our approach: the ability to learn from limited training data. However, to show that this is not the *only* advantage of our approach we ran auxiliary experiments with larger and smaller training sets. When the training set was enlarged our system outperformed Torralba's by a significant but smaller margin, and when the training set was decreased, the performance of our system decreased only slightly whereas Torralba's system was unable to estimate the Gaussian mixture due to the sparsity of training samples. The latter case corresponds to just 20 examples per label. These results are shown in the top and bottom rows of Table 3.1.

Figures 3.8 and 3.9 show positive and negative results from our system. Note how our system recognises images containing disjoint views of a room as belonging to the same place.

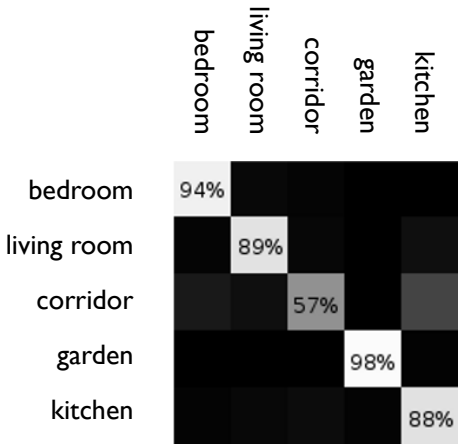

Figure 3.7: Confusion matrix for place recognition. This figure corresponds to the bottom row of Table 3.1.

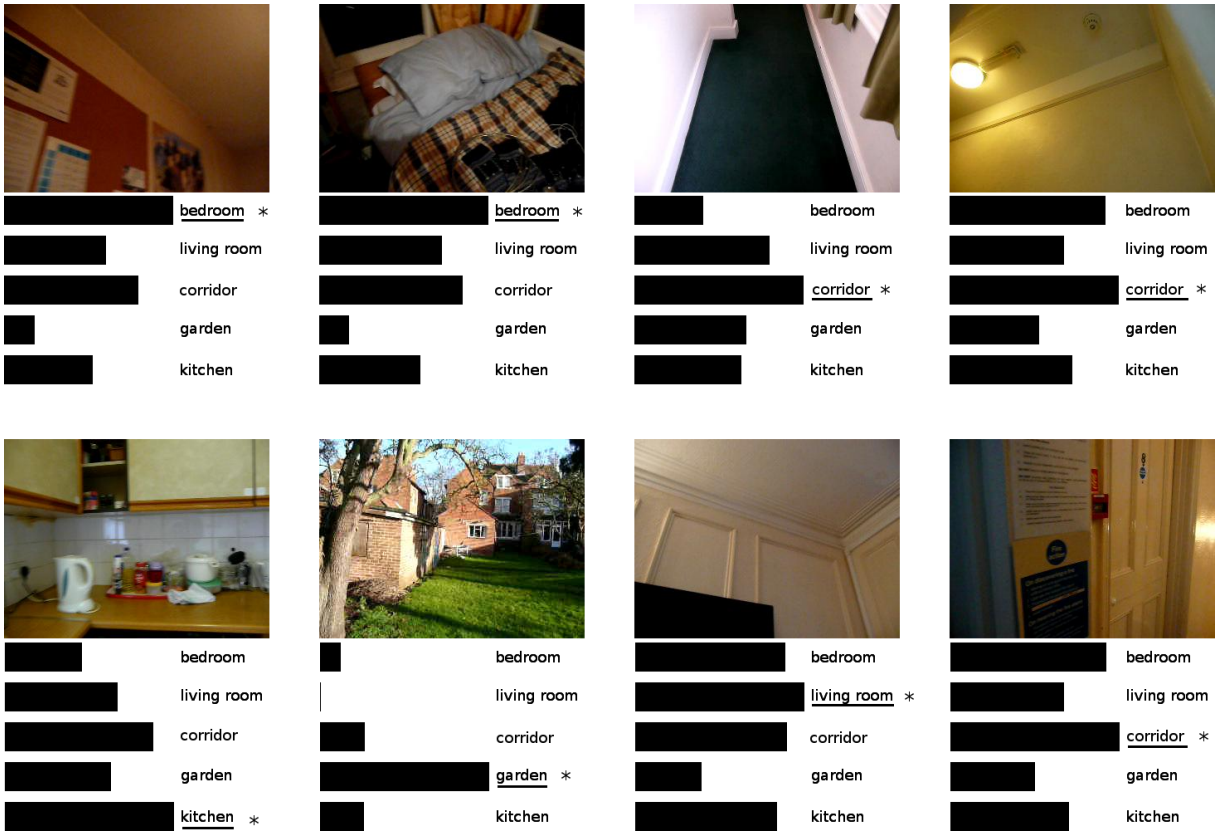

Figure 3.8: Example frames for which our classifier produced the correct output. The ground truth label is underlined and the output from our system is starred. We show the posterior distribution over class labels in black. Note the variation between images with the same label, and the low quality of many images.

No. training frames	This chapter	Torralba *et al.*	Nearest neighbours
103	**81%**	—	45%
230	**83%**	62%	52%
565	**85%**	70%	55%

Table 3.1: Recognition rate for the place recognition problem with varying numbers of training examples. The reported accuracy is the mean over the on–diagonal elements of the confusion matrix. The left column reports the total number of training examples for all categories. For the experiment with 103 training examples we were unable to estimate the Gaussian mixtures required for the system of Torralba *et al.* due to the sparsity of the training examples. The nearest neighbours baseline was computed by resizing images to 64 by 64 pixels and comparing raw pixel intensities in the L2 sense.

Figure 3.9: Example frames for which our classifier failed. See caption of Figure 3.8.

3.6 Camera Orientation Classification

In this section we show how our system can deduce a coarse camera orientation from a single image. We are interested only in the tilt of the camera with respect to the ground plane. Our intention is to make a rapid but coarse estimate of camera orientation. We pose the problem as a classification task with three labels: "up", "straight", and "down". The "straight" label represents images taken with the camera axis parallel to the ground plane, plus or minus $22.5°$, and the "up" and "down" labels represent all orientations facing further upwards or downwards respectively (see Figure 3.10).

We captured three sequences in which the camera orientation was fixed within one of the above orientation ranges. We included footage from five different places (the same rooms used in the previous section) but we labelled the frames according to orientation only. This represents a

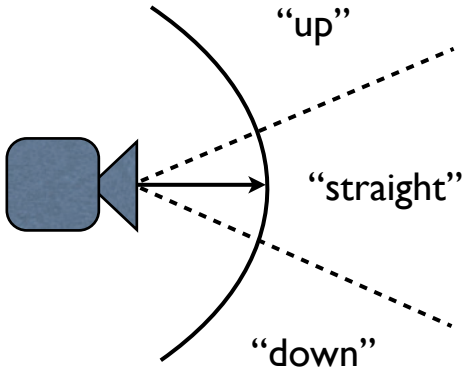

Figure 3.10: Definition of the labels for camera orientation recognition.

difficult classification task because the system must learn properties that correlate with camera orientation but are not tied to the appearance of a particular room. We then trained our system to distinguish between the three orientation categories as in the previous section.

We again compared with the “gist” of Torralba *et al.* and a KNN baseline. We ran auxiliary experiments with an enlarged training set as in the previous section. The results of these experiments are shown in Table 3.2 and Figure 3.11. Our system again outperformed both other classifiers by a significant margin. Some example frames for which our system correctly identified the camera orientation are shown in Figure 3.12. Of particular interest is our system’s ability to generalise across images taken with the same camera orientation at several different locations.

No. training frames	This chapter	Torralba *et al.*	Nearest neighbours
88	**70%**	61%	59%
728	**79%**	63%	59%

Table 3.2: Camera orientation classification results using small and large training sets. The reported accuracies are the average of the on–diagonal entries in the confusion matrix. In this case we were able to estimate the Gaussians for Torralba’s system using only 88 training examples because there were fewer categories than in the place recognition problem. The nearest neighbours baseline was computed by resizing images to 64 by 64 pixels and comparing raw pixel intensities in the L2 sense.

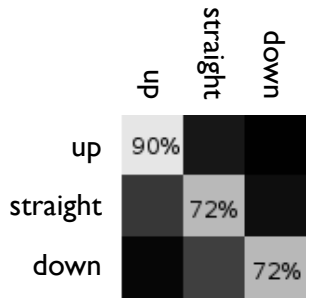

Figure 3.11: Confusion matrix for camera orientation classification. This figure shows results corresponding to the bottom row in Table 3.2.

Figure 3.12: Twelve frames for which our system correctly identified the camera orientation. From the top to bottom the rows contain images from the "up", "straight", and "down" classes.

3.7 Computational Concerns

The most computationally demanding aspect of our system is the convolutions needed to generate the pixel features. In this section we describe several optimisations for the convolution operation. Timing results are shown in Table 3.3 at the end of this section.

3.7.1 Separable Kernels

The Gabor function, which we use to generate pixel features, in its canonical form is a complex–valued function and can be trivially separated. However, in our work we use just the real part,

$$H_{real}(x, y) \quad = \quad g_2(x, y) \cos(kx \cos\theta + ky \sin\theta) \ , \tag{3.3}$$

where g_2 is the two–dimensional Gaussian function. This can be written as the difference between two separable function as

$$H_{real}(x, y) \quad = \quad \Big(g_1(x) \cos ax\Big)\Big(g_1(y) \cos by\Big) - \Big(g_1(x) \sin ax\Big)\Big(g_1(y) \sin by\Big) \tag{3.4}$$

where g_1 is the one–dimensional Gaussian function and we have used the cosine expansion formula. We implement this by running two separated convolutions and then taking their difference, which is significantly faster than performing the original convolution.

3.7.2 Parallelization over filters

Generating the pixel features requires convolving an input image with 12 different filters. To leverage the parallelism of modern multi–core CPUs we execute the convolutions in parallel where possible. This approach allows parallelization within a single scale, but requires synchronisation upon completion of each scale due to the down–sampling operation.

3.7.3 Parallelization over pixels

Modern graphics hardware allows efficient parallelization of small–scale computations such as per–pixel operations. This is is well suited to performing convolutions since each output pixel is functionally independent of all others. To leverage this we implemented convolutions using a C–like language designed specifically for programming graphics hardware. We note that further improvements may be possible since under the current implementation, much time is spent transferring data between the CPU and GPU, in comparison to which the time spent performing the convolutions is small. This bottleneck could be partially avoided if we performed the texton labelling in the GPU and transferred only the final texton map back to the CPU.

3.7.4 Timing results

Results from timing evaluations are shown in Table 3.3. The GPU strategy outperforms all others. It improves over the baseline strategy by a factor of 5 for the 320×240 image and by a factor of 6 for the 640×480 image.

It is interesting to note that when the image is enlarged to include four times as many pixels, the three CPU–based strategies degrade by a factor very close to four, whereas the GPU implementation degrades by a factor closer to three. This indicates that this task saturates CPU performance but that a significant overhead remains in the GPU implementation. This matches our observation in the previous section that transmitting data between the CPU and GPU consumes much time, and that further performance improvements are possible.

3.8 Conclusions

In this chapter we have shown that texture structure can be leveraged to deduce high–level information about image scenes. We have motivated the use of textons for this purpose with several qualitative examples, and have presented results from two in–depth experiments. In

	320×240		640×480	
Strategy	**Per Frame**	**Frame Rate**	**Per Frame**	**Frame Rate**
No parallelization	115.0ms	8.69Hz	463.6ms	2.16Hz
Filter–parallel	38.0ms	26.3Hz	148.0ms	6.76Hz
Image–parallel	32.1ms	31.2Hz	125.6ms	8.02Hz
Pixel–parallel (GPU)	23.5ms	42.5Hz	78.1ms	12.80Hz

Table 3.3: Timing results for the four parallelization strategies. Each strategy was evaluated for two image sizes. All strategies utilise separated filters. Results are averages over 10 invocations.

both cases our system based on relative displacements between textons obtains highly encouraging results. Furthermore, by utilising graphics hardware our system is capable of operating at video frame rate.

4

The Geometry of Indoor Environments

This chapter develops the idea that comprehensive scene understanding at the level of objects, actions, and surfaces requires at least a rudimentary understanding of the high–level geometry of the environment. There are many ways to capture such coarse geometry; here we argue that the indoor Manhattan representation is an excellent choice in terms of the salient geometric information it captures, its simplicity, and the elegant inference procedures it permits. This chapter focuses on analysing the model itself, leaving algorithms and empirical results to later chapters. This constitutes the first comprehensive definition and analysis of indoor Manhattan environments in the literature (though not the first account *per se* [43]). The primary contributions of this chapter are a derivation of the "vertex" and "seam" parametrisations, and the description of several properties of these parametrisations that will prove crucial to the development of the following chapters.[1]

[1] This work was published in part in:
Flint, Mei, Murray, and Reid, "A Dynamic Programming Approach To Reconstruction Building Interiors", in *Proceedings of the 2010 European Conference on Computer Vision* [21]

Figure 4.1: Two examples of indoor Manhattan environments.

4.1 Introduction

The preceding chapter described an approach to scene understanding in which raw image features were connected directly to high–level quantities such as scene categories. This chapter begins the development of a more sophisticated model in which pixel–level features are connected to high–level quantities via an unobserved intermediate level representing scene geometry. We focus on recovering this intermediate representation, leaving the application to specific classification tasks to future work. There are a number of reasons to see geometry as central to scene understanding. For an intuitive demonstration, consider the information conveyed by the red, green, and blue regions in Figure 4.1. These regions have very low fidelity (the entire model is defined by just a handful of polygons), yet it is clear that they convey considerable information about the likely locations of various objects, the scale at which those objects would appear, and how they would interact.

There are many choices for the representation of the intermediate–level variables; the following desiderata summarise the requirements relevant to our goals.

1. **Salience.** Of all the information present at the image level, the intermediate variables should capture as much of the information that is *relevant* to inferring the high–level quantities of interest as possible.

2. **Compression.** The intermediate representation should discard as much irrelevant infor-

mation as possible. All else equal, we prefer succinct representations of the world for efficiency reasons. See MacKay [48] for a discussion of the connection between compression and learning.

3. **Tractability.** All else equal, we prefer representations that lead to simple and efficient inference algorithms. A simple model for which inference is tractable may be preferable to a slightly more expressive model in which one must rely on approximate inference procedures with poorly–understood convergence properties.

4. **Simplicity.** All else equal, we prefer representations consisting of quantities that are intuitive to humans.

5. **Generality.** The chosen representation should be applicable to a wide variety of real–world environments.

We have chosen to work with the indoor Manhattan representation, in which the world is built up from a floor plane, a ceiling plane, and a sequence of vertical wall segments. This representation was originally proposed by Lee *et al.* [43]. Indoor Manhattan environments are a sub–class of general Manhattan environments, which simply specify surfaces in three mutually orthogonal directions. Indoor Manhattan scenes satisfy the desiderata above for the following reasons.

- **Compression and salience.** As described above, the geometric entities present in the indoor Manhattan representation correlate well the high–level quantities of interest for scene understanding. The models shown in Figure 4.1 consume just a few hundred bytes, yet capture much of the information present in the original image data, which consumes three orders of magnitude more space. The point here is not to save disk space, but to demonstrate that indoor Manhattan models efficiently capture salient information.

- **Simplicity.** Indoor Manhattan models are composed of quantities that have have natural semantics, being associated with entities such as the floor, walls, and ceiling of an environment.

- **Generality.** Indoor Manhattan models can represent many environments exactly or approximately; even those that do not conform exactly to the assumptions of the model. We expand on this later.

- **Tractability.** Indoor Manhattan scenes have special geometric structure that permits an elegant "seam" representation. This in term leads to efficient and exact inference algorithms for a range of sensor models, and an attractive learning algorithm. This are the subject of the ensuing chapters.

By adopting the indoor Manhattan representation we are *not* restricted to working with *ideal* indoor Manhattan environments — environments free of clutter, occlusions, windows, or other deviations from our assumptions. Rather, the point is to take account of such deviations in the probabilistic model relating image features to scene structure. For example, the model we present for depth measurements in Chapter 6 explicitly marginalises over the possibility that a given depth measurement corresponds to a clutter object, an object observed through a window, or an erroneous measurement. Thus we cast the Manhattan scene geometry as a latent variable to be inferred in the presence of noise, clutter, and occlusions, rather than as a complete description of everything we might observe. Empirical results in forthcoming chapters show many examples of our system working in real–world environments that are very far from ideal indoor Manhattan scenes, containing poor lighting and noisy images in addition to clutter, windows, and non–Manhattan–aligned surfaces.

However, this chapter focuses on analysing the representation itself, and so is concerned with ideal indoor Manhattan scenes. The contributions of this chapter are (1) the first comprehensive definition of the indoor Manhattan assumption; (2) two novel representations for indoor Manhattan scenes; and (3) a number of minor results connecting these representations and providing other insights crucial to the ensuing chapters. As mentioned above, this chapter does not contain any experimental results, though it does provide the conceptual infrastructure that the remainder of this thesis builds on. We begin by defining indoor Manhattan scenes, then we discuss our first representation in terms of floorplans, followed a description of the "vertex" and "seam" parametrisations that will be used in following chapters. Section 4.5 contains a

number of minor deductions of relevance to the ensuing chapters, then we close with a brief conclusion.

4.2 Indoor Manhattan Environments

Let a reconstruction G consist of a set of polygons P_i with vertices $\boldsymbol{v}_j \in \mathbb{R}^3$. An *indoor Manhattan reconstruction* is a reconstruction G with the following properties.

1. *Each polygon is oriented in one of three mutually orthogonal directions*. Formally, for each pair of polygons $P_i, P_j \in G$ with unit–length normals $\boldsymbol{n}_i, \boldsymbol{n}_j$,

$$\boldsymbol{n}_i \cdot \boldsymbol{n}_j \in \{0, 1\} \tag{4.1}$$

2. *There is a floor plane and a ceiling plane*. Formally, there exists some direction $\boldsymbol{n}_v$ and a pair of real numbers z_f, z_c such that each polygon $P \in G$ with normal $\boldsymbol{n} = \boldsymbol{n}_v$ has vertices $\boldsymbol{v}$ satisfying

$$\boldsymbol{v} \cdot \boldsymbol{n}_v \in \{z_f, z_c\} \tag{4.2}$$

3. *Vertical walls extend from floor to ceiling*. Formally, if $\boldsymbol{n}_i \neq \boldsymbol{n}_v$ then we say that $P_i \in G$ is a *vertical* polygon. This condition is satisfied if and only if each vertex $\boldsymbol{v}$ of each vertical polygon satisfies

$$\boldsymbol{v} \cdot \boldsymbol{n}_v \in \{z_f, z_c\} \tag{4.3}$$

4. *The edges of walls are vertical*. Formally, if $\boldsymbol{v} \in P$ and $\boldsymbol{v} \cdot \boldsymbol{n}_v = z_f$, then $\exists \boldsymbol{u} \in P$ such that

$$\boldsymbol{u} \cdot \boldsymbol{n}_v = z_c \tag{4.4}$$

and

$$\boldsymbol{u} = \boldsymbol{v} + \lambda \boldsymbol{n}_v \tag{4.5}$$

for some $\lambda \in \mathbb{R}$.

We assume a pinhole camera mapping homogeneous world coordinates $\boldsymbol{X} \in \mathbb{R}^4$ to homogeneous image coordinates $\boldsymbol{x} \in \mathbb{R}^3$ according to

$$\boldsymbol{x} = K \begin{bmatrix} R & \boldsymbol{t} \end{bmatrix} \boldsymbol{X} \,, \tag{4.6}$$

where K is a 3×3 homography, R is a 3–dimensional rotation matrix, and $\boldsymbol{t}$ is a 3–dimensional translation.

We define an indoor Manhattan *scene* as a reconstruction together with a camera viewpoint, subject to the following additional constraints.

1. The camera centre $\boldsymbol{c}$ is located between the floor and ceiling planes,

$$z_f < \boldsymbol{c} \cdot \boldsymbol{n}_v < z_c \tag{4.7}$$

2. The reconstruction is closed relative to the camera viewpoint. Formally, for each viewing direction $\boldsymbol{x}$ there is some polygon $P \in G$ containing a point $\boldsymbol{X}$ that projects to $\boldsymbol{x}$.

In general we will assume that scenes consist only of those polygons visible to the camera. Since reconstructions consists of a finite number of polygons and our camera model is linear, it can be shown that an indoor Manhattan reconstruction truncated to a view frustum remains an indoor Manhattan reconstruction as defined above.

4.3 Floorplans

The polygonal representation for indoor Manhattan environments is inconvenient for our purposes. A more useful representation is a *floorplan*, in which walls are represented as line segments in the XY plane. Formally, we define a floorplan F as a tuple (R_w, Z, T), where

- R_w is a 3–dimensional rotation;

- $Z = (z_f, z_c)$ is a pair of scalars defining the floor and ceiling planes,

$$P_{\text{floor}} = \{\boldsymbol{x} \mid \boldsymbol{x} \cdot [0\ 0\ 1] = z_f\} \tag{4.8}$$

$$P_{\text{ceil}} = \{\boldsymbol{x} \mid \boldsymbol{x} \cdot [0\ 0\ 1] = z_c\}\ ; \tag{4.9}$$

- $T = \{(\boldsymbol{u}_i, \boldsymbol{v}_i)\}_{i=0}^{M}$, is a set of line segments defining walls, $\boldsymbol{u}_i, \boldsymbol{v}_i \in \mathbb{R}^2$.

A floorplan F is converted to a reconstruction as follows. First, extrude each line segment vertically out of the floor plane to meet the ceiling plane, resulting in a set of vertical planes. Next, add polygons for the floor and ceiling planes, which may simply be sufficiently large polygons parallel to the XY plane. Finally, apply the coordinate transform R_w. Formally, the reconstruction corresponding to a given floorplan is given by $G = \{(\boldsymbol{p}_i, \boldsymbol{q}_i, \boldsymbol{r}_i, \boldsymbol{s}_i)\}$ where

$$\boldsymbol{p}_i = R_w \begin{bmatrix} \boldsymbol{u}_i \\ z_f \end{bmatrix} \tag{4.10}$$

$$\boldsymbol{q}_i = R_w \begin{bmatrix} \boldsymbol{v}_i \\ z_f \end{bmatrix} \tag{4.11}$$

$$\boldsymbol{r}_i = R_w \begin{bmatrix} \boldsymbol{v}_i \\ z_c \end{bmatrix} \tag{4.12}$$

$$\boldsymbol{s}_i = R_w \begin{bmatrix} \boldsymbol{u}_i \\ z_c \end{bmatrix} \tag{4.13}$$

For the remainder of this chapter we use the term "corner" to refer to a point at which two line segments in the floorplan meet. In 3D, a corner is therefore a vertical seam at which two walls meet. This contrasts with the usual computer vision terminology in which a corner corresponds to a point in 3D.

4.3.1 Images of Floorplans

The remainder of this thesis will be simplified considerably if we can assume that vertical lines in the world appear vertical in image coordinates. To that end we define the following homography:

$$H_{\text{rect}} = \begin{pmatrix} \boldsymbol{v}_v \times \boldsymbol{e}_3 \\ \boldsymbol{v}_v \\ \boldsymbol{v}_v \times \boldsymbol{e}_3 \times \boldsymbol{v}_v \end{pmatrix} . \tag{4.14}$$

where $\boldsymbol{v}_v$ is the vertical vanishing point and $\boldsymbol{e}_3 = [0\,0\,1]$. Let I' be the image formed by applying the homography H_{rect} as a coordinate transform to I,

$$I'(\boldsymbol{x}) = I(H_{\text{rect}}\boldsymbol{x}) \tag{4.15}$$

where we are implicitly working in homogeneous coordinates. We say that I' is *vertically rectified* in the sense that any line containing $\boldsymbol{v}_v$ in the original image will be mapped to a vertical line in the output image. To confirm this we note that H_{rect} maps $\boldsymbol{v}_v$ to vertical infinity as the following derivation shows.

$$H_{\text{rect}}\,\boldsymbol{v}_v = \begin{pmatrix} \boldsymbol{v}_v \times \boldsymbol{e}_3 \\ \boldsymbol{v}_v \\ \boldsymbol{v}_v \times \boldsymbol{e}_3 \times \boldsymbol{v}_v \end{pmatrix} \boldsymbol{v}_v \tag{4.16}$$

$$= \begin{pmatrix} 0 \\ \boldsymbol{v}_v \cdot \boldsymbol{v}_v \\ 0 \end{pmatrix} . \tag{4.17}$$

In practice the image I is not a continuous signal but is sampled at discrete pixel locations. As a result, the transformation H_{rect} will result in a a non–uniformly sampled image plane. Worse, if the vertical vanishing point $\boldsymbol{v}_v$ is within the original image boundary, then the transformation H_{rect} will introduce a singularity at this point.

Thankfully, the validity of the algorithms presented in the remainder of this thesis do not in fact depend on performing the rectification (4.15) — we could perform all calculations assuming a non–rectified image, in which case "image columns" would be replaced by "rays cast from the vertical vanishing point". The seam concept introduced in Section 4.4.3 would be replaced by paths moving clockwise or anti–clockwise about the vertical vanishing point depending on whether it is located above or below the image centre. However, it will simplify the remainder of this thesis considerably if we assume the rectification (4.15) so without loss of generality we assume throughout the remainder of this thesis that the vertical vanishing point falls outside the image bounds and that images have been rectified.

4.4 Parametrisation

In this section we turn to the scene parametrisation that we will use during learning and inference in the following chapters. We parametrise each component of the floorplan tuple $F = (R_w, Z, T)$ separately. R_w is parametrised as a member of the Lie group $SO(3)$, which will be discussed further in Chapter 5. The remainder of this section is concerned with the parametrisation of Z (the floor and ceiling position) and T (the position of the walls).

4.4.1 Parametrising the floor and ceiling location

In the preceding sections we implicitly parametrised the floor and ceiling planes with a pair of scalars $z_f, z_c \in \mathbb{R}$. We now switch to a different parametrisation (μ, λ) where $\mu \in \mathbb{R}$ parametrises a planar homology relating the images the floor and ceiling planes, and λ represents a scale factor that cannot be observed from a single view. λ is expressed in the coordinate system that the input camera poses are expressed in, which is typically defined by the structure–from–motion system that recovered those poses. This allows us to relate the entities estimated by structure–from–motion (points and cameras) to the entities estimated during Manhattan structure recovery.

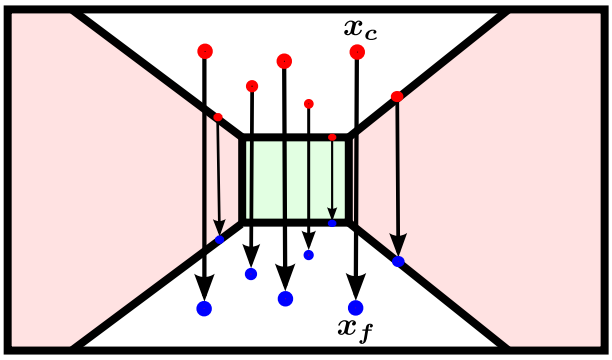

Figure 4.2: The mapping H_a transfers points between the ceiling and floor.

The advantage of this representation is that μ can be estimated from a single image and is sufficient to perform inference in the single image context. If only one image is available then we may simply ignore λ and the remainder of the algorithms in this thesis go through without modification, while in the multiple view context we may estimate λ directly.

ofWe define λ as the absolute z component (in the coordinate system used by structure–from–motion) either the floor or ceiling plane. To define μ we first need to introduce the *Manhattan correspondence*. For the purpose of this section we will say that two image points $\boldsymbol{p_f}$ and $\boldsymbol{p_c}$ correspond if and only if the difference between their back–projections onto the floor and ceiling plane respectively is parallel to the z axis, as illustrated in Figure 4.2. Formally, for a camera $(K, R, \boldsymbol{t})$, $\boldsymbol{p_f}$ and $\boldsymbol{p_c}$ are in correspondence if and only if there exists $\boldsymbol{X_f}, \boldsymbol{X_c} \in \mathbb{R}^3$ with

$$\boldsymbol{p_f} = K(R\boldsymbol{X_f} + \boldsymbol{t}) \tag{4.18}$$

$$\boldsymbol{p_c} = K(R\boldsymbol{X_c} + \boldsymbol{t}) \tag{4.19}$$

$$\boldsymbol{X_c} = \boldsymbol{X_f} + r\boldsymbol{e}_3 \quad r \in \mathbb{R} \tag{4.20}$$

Since the floor and ceiling planes are parallel, there is a planar homology H_a such that

$$\boldsymbol{p_f} = H_a\boldsymbol{p_c} \tag{4.21}$$

if and only if $\boldsymbol{p_f}$ and and $\boldsymbol{p_c}$ are in correspondence [13]. We define μ as the unique real number

such that

$$H_a = I + \mu \frac{\boldsymbol{v_v} \boldsymbol{h}^T}{\boldsymbol{v_v} \cdot \boldsymbol{h}} \tag{4.22}$$

where

$$\boldsymbol{h} = KR\boldsymbol{e}_1 \times KR\boldsymbol{e}_2 \tag{4.23}$$

is the horizon line. Given any corresponding pair $(\boldsymbol{p_f}, \boldsymbol{p_c})$, μ is given by [13]

$$\mu = \langle \boldsymbol{v_v}, \boldsymbol{p_c}, \boldsymbol{p_f}, (\boldsymbol{p_c} \times \boldsymbol{p_f}) \times \boldsymbol{h} \rangle \ , \tag{4.24}$$

where

$$\langle \boldsymbol{a}, \boldsymbol{b}, \boldsymbol{c}, \boldsymbol{d} \rangle = \frac{(\boldsymbol{a} - \boldsymbol{c}) \cdot (\boldsymbol{b} - \boldsymbol{d})}{(\boldsymbol{b} - \boldsymbol{c}) \cdot (\boldsymbol{a} - \boldsymbol{d})} \tag{4.25}$$

is the characteristic cross ratio of H_a.

Note that μ is invariant to the camera intrinsics since the cross ratio is a projective invariant[13]. We therefore assume without loss of generality that K is the identity for the remainder of this section.

To complete our parametrisation of the floor and ceiling planes we need to show how to compute (μ, λ) from (z_f, z_c). We may simply set λ to either z_f or z_c. Let

$$\boldsymbol{e_f} = z_f \, \boldsymbol{e}_3 \tag{4.26}$$

$$\boldsymbol{e_c} = z_c \, \boldsymbol{e}_3 \tag{4.27}$$

$$\boldsymbol{p_f} = R\boldsymbol{e_f} + \boldsymbol{t} \tag{4.28}$$

$$\boldsymbol{p_c} = R\boldsymbol{e_c} + \boldsymbol{t} \tag{4.29}$$

Then

$$\begin{aligned} (\boldsymbol{p_c} \times \boldsymbol{p_f}) \times \boldsymbol{h} &= \big((R\boldsymbol{e_f} + \boldsymbol{t}) \times (R\boldsymbol{e_c} + \boldsymbol{t})\big) \times \big(R\boldsymbol{e}_1 \times R\boldsymbol{e}_2\big) && (4.30) \\ &= \big((R\boldsymbol{e_c} + \boldsymbol{t}) \times (R\boldsymbol{e_f} + \boldsymbol{t})\big) \times R(\boldsymbol{e}_1 \times \boldsymbol{e}_2) && (4.31) \\ &= \big(R(\boldsymbol{e_c} - \boldsymbol{e_f}) \times \boldsymbol{t}\big) \times R\boldsymbol{e}_3 \ . && (4.32) \end{aligned}$$

We can now write

$$\begin{aligned}
\mu &= \langle \boldsymbol{v_v}, \boldsymbol{p_c}, \boldsymbol{p_f}, (\boldsymbol{p_c} \times \boldsymbol{p_f}) \times \boldsymbol{h} \rangle && (4.33)\\
&= \frac{\left(\boldsymbol{v_v} - \boldsymbol{p_f}\right)^T \left(\boldsymbol{p_c} - (\boldsymbol{p_c} \times \boldsymbol{p_f}) \times \boldsymbol{h}\right)}{\left(\boldsymbol{p_c} - \boldsymbol{p_f}\right)^T \left(\boldsymbol{v_v} - (\boldsymbol{p_c} \times \boldsymbol{p_f}) \times \boldsymbol{h}\right)} && (4.34)\\
&= \frac{\left(R\boldsymbol{e}_3 - (R\boldsymbol{e_f} + \boldsymbol{t})\right)^T \left(R\boldsymbol{e_c} + \boldsymbol{t} - (R(\boldsymbol{e_c} - \boldsymbol{e_f}) \times \boldsymbol{t}) \times R\boldsymbol{e}_3\right)}{\left(R\boldsymbol{e_c} + \boldsymbol{t} - R\boldsymbol{e_f} - \boldsymbol{t}\right)^T \left(R\boldsymbol{e}_3 - (R(\boldsymbol{e_c} - \boldsymbol{e_f}) \times \boldsymbol{t}) \times R\boldsymbol{e}_3\right)} && (4.35)\\
&= \frac{\left(\boldsymbol{e}_3 - \boldsymbol{e_f} - R^T\boldsymbol{t}\right)^T R^T \left(R\boldsymbol{e_c} + \boldsymbol{t} - (R(\boldsymbol{e_c} - \boldsymbol{e_f}) \times \boldsymbol{t}) \times R\boldsymbol{e}_3\right)}{\left(\boldsymbol{e_c} - \boldsymbol{e_f}\right)^T R^T \left(R\boldsymbol{e}_3 - (R(\boldsymbol{e_c} - \boldsymbol{e_f}) \times \boldsymbol{t}) \times R\boldsymbol{e}_3\right)} && (4.36)\\
&= \frac{\left(\boldsymbol{e}_3 - \boldsymbol{e_f} - R^T\boldsymbol{t}\right)^T \left(\boldsymbol{e_c} + R^T\boldsymbol{t} - ((\boldsymbol{e_c} - \boldsymbol{e_f}) \times R^T\boldsymbol{t}) \times \boldsymbol{e}_3\right)}{(\boldsymbol{e_c} - \boldsymbol{e_f})^T \boldsymbol{e}_3 - (\boldsymbol{e_c} - \boldsymbol{e_f})^T (((\boldsymbol{e_c} - \boldsymbol{e_f}) R^T\boldsymbol{t}) \boldsymbol{e}_3)} && (4.37)\\
&= \frac{(\boldsymbol{e}_3 - \boldsymbol{e_f} - R^T\boldsymbol{t})^T (\boldsymbol{e_c} + R^T\boldsymbol{t}) + (z_c - z_f)(\|\boldsymbol{t}\|^2 - (\boldsymbol{e}_3^T R^T\boldsymbol{t})^2)}{z_c - z_f} && (4.38)\\
&= \frac{1}{z_c - z_f}\Big((z_c + z_\rho)(1 - z_f - z_\rho) + z_\rho^2 - \|\boldsymbol{t}\|^2\Big) + \|\boldsymbol{t}\|^2 - z_\rho^2 && (4.39)
\end{aligned}$$

where in the last line we substituted $z_\rho = \boldsymbol{e}_3^T R^T \boldsymbol{t}$.

4.4.2 Parametrising walls

We choose to parametrise T in image coordinates because this will simplify the algorithms to be presented later. We first present the image–domain parametrisation, then show that it uniquely specifies a 3D scene.

Consider the scenes shown in Figure 4.3. Following rectification, vertical edges in the world appear vertical in each image, including the vertical seams between adjacent wall segments, so any line drawn vertically from the top to bottom of a rectified image intersects exactly one wall segment. That this is true in general follows from our assumption that walls meet at vertical seams and extend continuously from floor to ceiling, that the camera is located between the floor and ceiling planes, and that the environment is closed.

It turns out that once the vanishing points $\boldsymbol{v}_i$ and the Manhattan homology H_a are known, the quadrangle outlining a wall segment in rectified image coordinates is fully specified by just

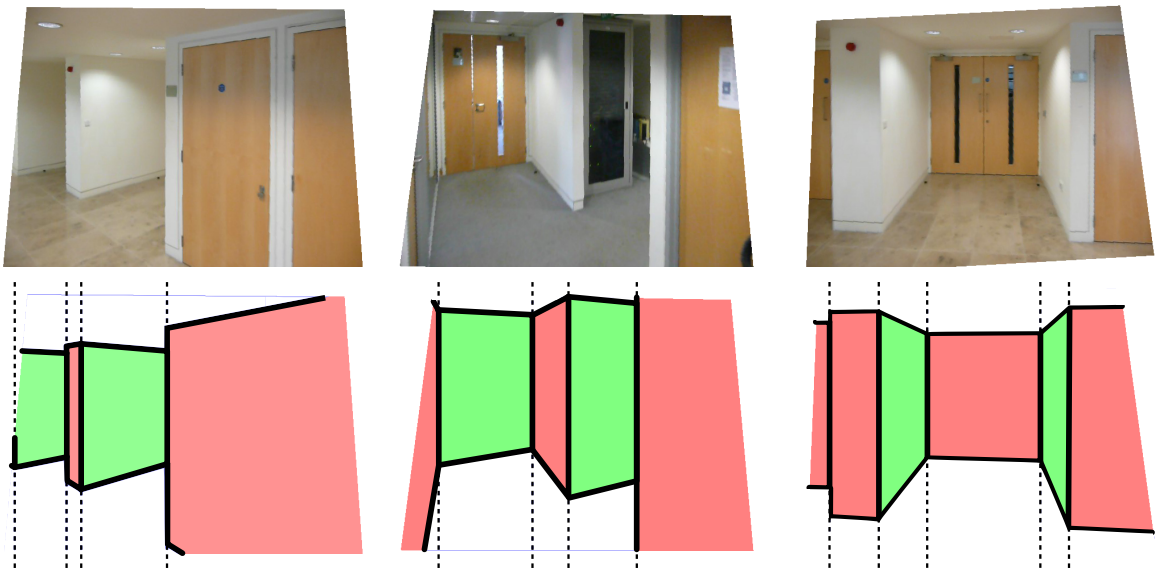

Figure 4.3: Three input images and the indoor Manhattan models we seek. Notice how each image column intersects exactly one wall.

four variables (one binary and three scalars)

$$W = (x_0, y, o, x_1) \tag{4.40}$$

as illustrated in Figure 4.4. x_0 is the location of the left edge, x_1 is the location of the right edge, y is the y–coordinate of the top–left corner, and $o \in \{1, 2\}$ is the index of the vanishing point associated with the wall. The four vertices of the wall are then given by

$$\boldsymbol{p_i} = \begin{bmatrix} x & y & 1 \end{bmatrix}^T \tag{4.41}$$

$$\boldsymbol{q_i} = \boldsymbol{p_i} \times \boldsymbol{v_{o_i}} \times \begin{bmatrix} 1 & 0 & -x_{i+1} \end{bmatrix}^T \tag{4.42}$$

$$\boldsymbol{r_i} = H_a \boldsymbol{q_i} \tag{4.43}$$

$$\boldsymbol{s_i} = H_a \boldsymbol{p_i} \, . \tag{4.44}$$

Since each image column intersects exactly one wall, we may think of the scene as a sequence of walls from left to right in the image. This observation suggests our scene parametrisation, which is simply a sequence of wall segments (see Figure 4.5. We make the additional observation that the right edge of a wall (x_1 in equation (4.40)) is redundant because it is always

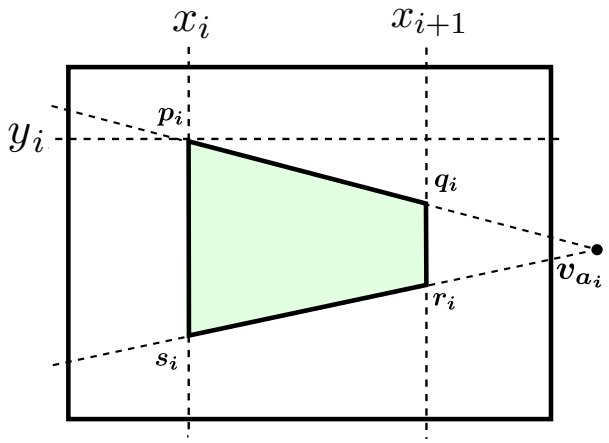

Figure 4.4: The scalars x_i, x_{i+1}, y_i, together with the vanishing point index $o_i \in \{1, 2\}$ and the homology H_a fully determine the four vertices of a wall.

coincident with the left edge of the wall to its right. A scene therefore is fully specified by

$$M = (x_1, y_1, o_1,\ x_2, y_2, o_2,\ \ldots,\ x_{n-1}, y_{n-1}, o_{n-1},\ x_n)\,. \tag{4.45}$$

These values are illustrated in Figure 4.5. Note that although the right edge of a wall always coincides with the left edge of its neighbour, it is not always the case that the top and bottom edges of adjacent walls meet at a point, *i.e.* $\boldsymbol{r_i} \neq \boldsymbol{s_{i+1}}$ in general. For example, notice the second wall in Figure 4.5.

Physical Feasibility

Not all scenes M are physically realisable as metric reconstructions, but those that are not can be discarded using simple tests on the locations of walls and vanishing points as enumerated by Lee *et al.* [43]. The reader is referred to their paper for details; the key result for our purposes is that a model is feasible if all of its corners are feasible, and the feasibility of a corner is dependent only on the immediately adjoining walls. We discuss these issues in detail during Chapter 6.

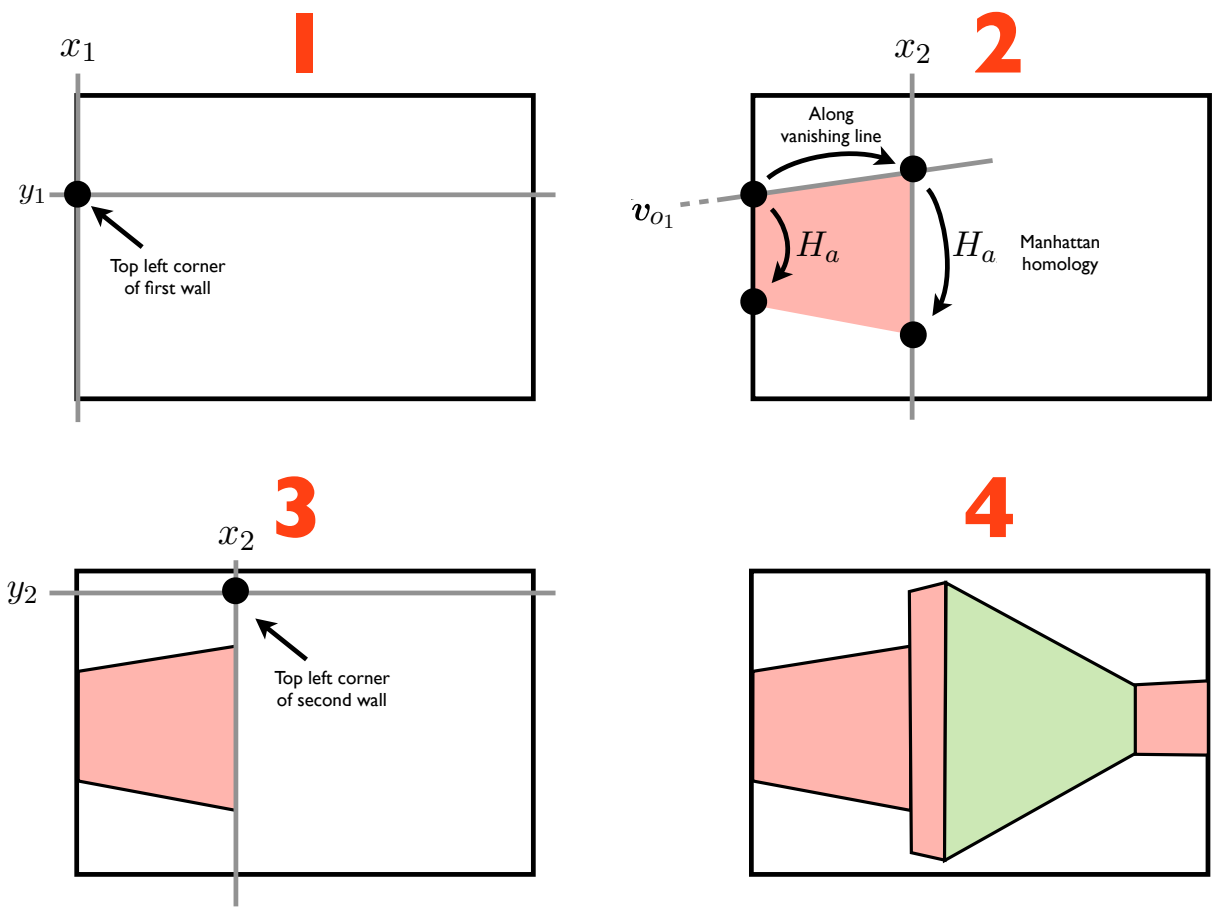

Figure 4.5: The meaning of the parameters in the vertex representation is illustrated through a constructive example. (1) The top–left corner of the first wall is at (x_1, y_1). (2) The top–right corner of the first wall is found by intersecting the vanishing line with the line x_2. Then both points are projected through H_a, yielding the four corners of the first wall. (3) The top–left corner of the second wall is at (x_2, y_2). (4) This is repeated to build up the entire model.

4.4.3 The Seam Representation

For the purpose of the probabilistic model that we will present in chapter Chapter 6 we will now present an additional, slightly different parametrisation that we will refer to as the *seam* representation of indoor Manhattan scenes. We will refer to the parametrisation of equation (4.45) as the *vertex* representation. A scene in vertex representation M uniquely determines a scene in seam S representation, but the converse is not true. For this reason we will always work in the vertex representation during inference, but to evaluate likelihoods, priors, and posteriors for a fixed scene we will find it notationally more convenient to work in the seam representation. Under the seam representation a scene is represented by associating a pair of

Figure 4.6: An example of an indoor Manhattan scene and its seam representation shown in red. The black dotted lines can be recovered from the seam using the Manhattan homology H_a.

scalars (s_j, o_j) to each image column j,

$$S = \{(s_j, o_j)\}_{j=0}^{W}\,, \tag{4.46}$$

where s_j is the y–coordinate of the bottom edge of the wall that intersects the j^{th} column, and $o_j \in \{1, 2\}$ is the index of its associated vanishing point. Note that the size of this representation is proportional to the image width, whereas the size of the vertex representation is proportional to the number of distinct wall segments. See Figure 4.6 for an illustration of this parametrisation.

We compute the seam representation S from a scene in vertex representation M as follows. For each $j \in [0, W]$ we identify the index of the (unique) wall segment that intersects column j by finding $x_i, x_{i+1} \in M$ such that $x_i \leq j \leq x_{i+1}$. Next we compute $\boldsymbol{s_i}$ and $\boldsymbol{r_i}$ according to equations (4.44) and (4.43), after which the position of the wall seam at column j is given by

$$s_j = (\boldsymbol{r_i} \times \boldsymbol{s_i}) \times \begin{bmatrix} 0 & 1 & -j \end{bmatrix}^T\,. \tag{4.47}$$

Finally, the orientation o_j at column j is equal to the orientation of the identified wall segment, o_i. The constructive process described above shows that there is exactly one seam S associated

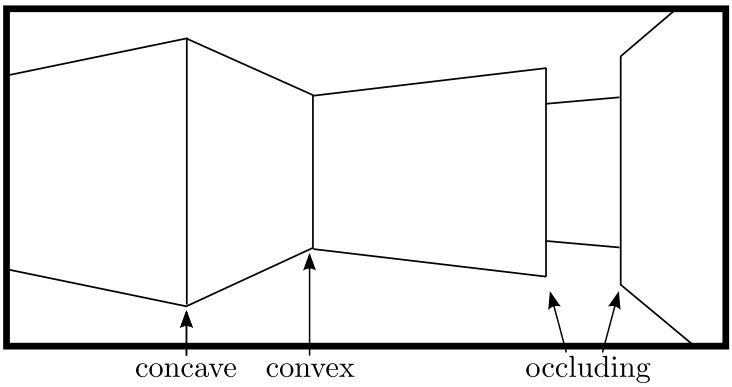

Figure 4.7: Each corner in an indoor Manhattan environment can be categorised as concave, convex, or occluding.

with a scene in vertex representation. However, there is no unique mapping in the reverse direction. In other words, the mapping from vertex representation to seam representation is many–to–one.

4.5 Deductions

In this section we make several geometric observations that are crucial to the following chapters.

4.5.1 Classification of Corners

Lee *et al.* [43] showed that corners between adjacent walls can be divided into three categories as follows.

- A *convex corner* occurs where two wall segments meet exactly and form an internal angle not greater than $180°$, *i.e.*

$$\boldsymbol{r_i} = \boldsymbol{s_{i+1}} \tag{4.48}$$

$$\text{and} \tag{4.49}$$

$$\frac{(\boldsymbol{s_i} - \boldsymbol{r_i}) \cdot (\boldsymbol{q_i} - \boldsymbol{r_i})}{\|\boldsymbol{s_i} - \boldsymbol{r_i})\|\|(\boldsymbol{q_i} - \boldsymbol{r_i}\|} \leq \frac{(\boldsymbol{r_{i+1}} - \boldsymbol{r_i}) \cdot (\boldsymbol{q_i} - \boldsymbol{r_i})}{\|\boldsymbol{r_{i+1}} - \boldsymbol{r_i})\|\|(\boldsymbol{q_i} - \boldsymbol{r_i}\|} \,. \tag{4.50}$$

- A *concave corner* occurs where two wall segments meet exactly and form an internal angle greater than $180°$, *i.e.*

$$\boldsymbol{r_i} = \boldsymbol{s_{i+1}} \tag{4.51}$$

$$\text{and} \tag{4.52}$$

$$\frac{(\boldsymbol{s_i} - \boldsymbol{r_i}) \cdot (\boldsymbol{q_i} - \boldsymbol{r_i})}{\|\boldsymbol{s_i} - \boldsymbol{r_i})\|\|(\boldsymbol{q_i} - \boldsymbol{r_i}\|} > \frac{(\boldsymbol{r_{i+1}} - \boldsymbol{r_i}) \cdot (\boldsymbol{q_i} - \boldsymbol{r_i})}{\|\boldsymbol{r_{i+1}} - \boldsymbol{r_i})\|\|(\boldsymbol{q_i} - \boldsymbol{r_i}\|} . \tag{4.53}$$

- An *occluding corner* occurs where two wall segments meet but their lower edges do not coincide, *i.e.*

$$\boldsymbol{r_i} \neq \boldsymbol{s_{i+1}} \tag{4.54}$$

Examples of each type of corner are shown in Figure 4.7.

4.5.2 Recovering Metric Scene Structure

We now show that once R_w and Z are known, a scene M in vertex representation uniquely specifies a 3D model. We show this by demonstrating how to convert a scene M to a floorplan F, after which we may apply equations (4.41), (4.42), (4.43), and (4.44) to recover a polygonal reconstruction. In the single image context, the reconstruction is recovered up to scale (there is only a one–parameter scale ambiguity since cameras are assumed calibrated and vanishing directions are assumed mutually orthogonal). In the context of multiple views the reconstruction is recovered within the coordinate system in which the camera poses are given to us (which is typically the coordinate system identified by structure–from–motion).

Let $\text{backproject}(\boldsymbol{p}; \boldsymbol{w}, K, R, \boldsymbol{t})$ be the back–projection of image point $\boldsymbol{p}$ onto the plane $\boldsymbol{x} \cdot \boldsymbol{w} = 0$ given camera intrinsics K and extrinsics $R, \boldsymbol{t}$. To compute this we solve for $\boldsymbol{y}$ in

$$P\boldsymbol{y} = \boldsymbol{0} \tag{4.55}$$

where

$$P = \begin{bmatrix} & KR & & K\boldsymbol{t} - \boldsymbol{p} \\ 0 & 0 & 1 & -z_f \end{bmatrix} . \tag{4.56}$$

We will usually omit the camera parameters and simply write $\text{backproject}(\boldsymbol{p}; \boldsymbol{w})$. Furthermore, since we will often be back–projecting onto planes orthogonal to the z axis we adopt the short–hand

$$\text{backproject}(\boldsymbol{p}; z) = \text{backproject}(\boldsymbol{p}; \begin{bmatrix} 0 & 0 & 1 & -z \end{bmatrix}) . \tag{4.57}$$

To recover a floorplan F from a scene M we simply need to back–project $\boldsymbol{q_i}, \boldsymbol{s_i}$ pairs onto the floor plane. This is formalised in Algorithm 4.1.

Algorithm 4.1 Recovering a metric 3D scene from the vertex representation M.

Require: $M = (x_1, y_1, o_1, \ldots, x_n)$ {a scene in vertex representation}
Ensure: $F = \{(\boldsymbol{u_i}, \boldsymbol{v_i})\}$
  $F \leftarrow \emptyset$
  for $i = 1 \ldots n-1$ **do**
    $\boldsymbol{u_i} = \text{backproject}(\boldsymbol{s_i}; z_f)$
    $\boldsymbol{u_i} = \text{backproject}(\boldsymbol{r_i}; z_f)$
    $F \leftarrow F \cup (\boldsymbol{u_i}, \boldsymbol{v_i})$
  end for

4.5.3 Recovering Orientation and Depth

We say that an indoor Manhattan scene M predicts the depth $d_{\boldsymbol{p}}$ of each pixel $\boldsymbol{p}$ because we can compute the depth of each $\boldsymbol{p}$ given the hypothesis M. All depths are recovered within the coordinate system given to us by structure–from–motion. Similarly, a scene predicts an orientation $a_{\boldsymbol{p}} \in \{1, 2, 3\}$ for each pixel, which is the orientation of the 3D surface that projects to $\boldsymbol{p}$.

To compute either the orientation $a_{\boldsymbol{p}}$ or depth $d_{\boldsymbol{p}}$ for an image point $\boldsymbol{p}$ we first need to identify a wall that contains $\boldsymbol{p}$ within its (image–domain) outline. If there is such a wall then $\boldsymbol{p}$ has the orientation of that wall and we back–project $\boldsymbol{p}$ onto the wall in 3D to recover depth. If $\boldsymbol{p}$ is not contained by any wall then $\boldsymbol{p}$ must be on the floor or ceiling and therefore has the horizontal orientation. In this case we recover depth by back–projecting onto the floor or ceiling plane,

Algorithm 4.2 Recovering orientation and depth for an image location $\boldsymbol{p}$ under a scene hypothesis M.

Require: $M = (x_1, y_1, o_1, \ldots, x_n)$ {a scene in vertex representation}
Require: $\boldsymbol{p} = (x, y) \in \mathbb{R}^2$
Require: $x_1 \leq x < x_n$
Ensure: $i_{\boldsymbol{p}} \in [1, n], a_{\boldsymbol{p}} \in \{1, 2, 3\}, d_{\boldsymbol{p}} > 0$
  for $i = 1 \ldots n - 1$ **do**
    if $x_i \leq x < x_{i+1}$ **then**
      {Compute the floor–wall and ceiling–wall seam in column x}
      $s_f \leftarrow \boldsymbol{e}_2 \cdot (\boldsymbol{s_i} \times \boldsymbol{r_i}) \times \begin{bmatrix} 1 & 0 & -x \end{bmatrix}^T$
      $s_c \leftarrow \boldsymbol{e}_2 \cdot (\boldsymbol{s_i} \times \boldsymbol{r_i}) \times \begin{bmatrix} 1 & 0 & -x \end{bmatrix}^T$
      if $y < s_c$ **then**
        $a_{\boldsymbol{p}} \leftarrow$ "$vertorient$"
        $X_{\boldsymbol{p}} \leftarrow \text{backproject}(\boldsymbol{p}; z_c)$
      else if $s_c < y < s_f$ **then**
        $a_{\boldsymbol{p}} \leftarrow o_x$
        $w_{\boldsymbol{p}} \leftarrow \begin{bmatrix} 1 & 0 & 0 & -\text{backproject}(\boldsymbol{x_f}; z_f) \cdot \boldsymbol{e}_1 \end{bmatrix}^T$
        $X_{\boldsymbol{p}} \leftarrow \text{backproject}(\boldsymbol{p}; w_{\boldsymbol{p}})$
      else
        $a_{\boldsymbol{p}} \leftarrow$ "$vertorient$"
        $X_{\boldsymbol{p}} \leftarrow \text{backproject}(\boldsymbol{p}; z_f)$
      end if
      $d_{\boldsymbol{p}} \leftarrow (RX_{\boldsymbol{p}} + \boldsymbol{t}) \cdot \boldsymbol{e}_3$
      return
    end if
  end for

according to whether $\boldsymbol{p}$ is above or below the horizon respectively. This process is formalised in Algorithm 4.2.

These calculations are considerably simpler in the seam representation, which is why it proves useful in following chapters. Suppose we are given a scene in seam representation S and an integer pixel location $\boldsymbol{p} \in \mathbb{Z}^2$. We first look up the the pair $(s_j, o_j) \in S$ for the column j in which the pixel $\boldsymbol{p}$ falls. Denote this pair (s_x, o_x). Then the floor–wall seam in column x is at $s_f = s_x$ and the ceiling–wall seam can be recovered using the Manhattan homology. From here the orientation and depth at $\boldsymbol{p}$ are obtained using the procedure shown in Algorithm 4.3.

Algorithm 4.3 Recovering orientation and depth for an image location $\boldsymbol{p}$ under the seam representation S.

Require: $S = \{(s_j, o_j)\}$ {a scene in seam representation}
Require: $\boldsymbol{p} = (x, y) \in \mathbb{Z}^2$ {a query pixel}
Ensure: $a_{\boldsymbol{p}} \in \{1, 2, 3\}, d_{\boldsymbol{p}} > 0$
  {Compute the floor–wall and ceiling–wall seam in column x}
  $s_f \leftarrow s_x$
  $\boldsymbol{x_f} \leftarrow \begin{bmatrix} x & s_f & 1 \end{bmatrix}^T$
  $\boldsymbol{x_c} \leftarrow H_a \boldsymbol{x_f}$
  $s_c \leftarrow \frac{\boldsymbol{x_c} \cdot \boldsymbol{e}_2}{\boldsymbol{x_c} \cdot \boldsymbol{e}_3}$
  if $y < s_c$ **then**
    $a_{\boldsymbol{p}} \leftarrow$ "$vertorient$"
    $X_{\boldsymbol{p}} \leftarrow \text{backproject}(\boldsymbol{p}; z_c)$
  else if $s_c < y < s_f$ **then**
    $a_{\boldsymbol{p}} \leftarrow a_x$
    $\boldsymbol{w}_{\boldsymbol{p}} \leftarrow \begin{bmatrix} 1 & 0 & 0 & -\text{backproject}(\boldsymbol{x_f}; z_f) \cdot \boldsymbol{e}_1 \end{bmatrix}^T$
    $X_{\boldsymbol{p}} \leftarrow \text{backproject}(\boldsymbol{p}; \boldsymbol{w}_{\boldsymbol{p}})$
  else
    $a_{\boldsymbol{p}} \leftarrow$ "$vertorient$"
    $X_{\boldsymbol{p}} \leftarrow \text{backproject}(\boldsymbol{p}; z_f)$
  end if
  $d_{\boldsymbol{p}} \leftarrow (RX_{\boldsymbol{p}} + \boldsymbol{t}) \cdot \boldsymbol{e}_3$

4.5.4 Column–wise Decomposability

We have so far shown that the vertex representation suffices to recover metric scene structure up to scale, and that the depth and orientation predicted for each pixel can be computed directly from either the vertex or seam representation. One property of particular significance for the algorithms to be presented in the remainder of this thesis is that the procedure of Algorithm 4.3 only requires access to the pair (s_j, o_j) for the image column j that contains the query pixel. That is, the depth and orientation predicted for a pixel $\boldsymbol{p}$ are functionally independent of the location of the floor–wall seam in columns other than the one containing $\boldsymbol{p}$.

4.6 Conclusion

We have presented the indoor Manhattan model, in which the world is represented by floor, ceiling, and wall planes. We have motivated this model in terms of its salience, compactness,

and the simple parametrisations it permits. The vertex and seam representations are the primary contributions of this chapter; their specific structure is crucial to all following chapters. In particular, we will make repeated use of the decomposability property described in Section 4.5.4. While this chapter has described the geometry of ideal indoor Manhattan environments, the system that we develop in this thesis is not restricted to such sterile conditions; rather, the model presented in this chapter describes the scene structure that we seek to recover *despite* clutter and sensor noise.

5

Identifying Manhattan Orientations

In order to make use of the Manhattan world assumption we must first discover the orientation of the Manhattan world with respect to the camera. This chapter focuses on estimating a 3D rotation that transforms the three cardinal Manhattan orientations onto the x, y, and z axes. In contrast to much previous work, we seek to recover this rotation given a sequence of calibrated images, such as may be provided by a structure–from–motion or SLAM system. Where previous multiple–view approaches have focused on surface normal estimates derived from a reconstructed point cloud, we build upon ideas from single–view vanishing point detection and cast estimation in terms of photometric information. We develop a probabilistic model relating observed line segments to the 3D rotation we seek, and solve maximum–likelihood inference using an Expectation–Maximisation algorithm. Our likelihoods are derived from principled error models, and estimation is performed as a single optimisation. We show that our approach substantially out–performs a state–of–the–art approach based on surface normals, while providing much greater robustness than single–view vanishing point estimation.[1]

[1]This work was published in part in:
Flint, Mei, Murray, and Reid, "Growing Semantically Meaningful Models For Visual SLAM", in *Proceedings of the 2010 Conference on Computer Vision and Pattern Recognition*[22]

5.1 Introduction

Many man–made environments contain numerous surfaces oriented in three mutually orthogonal directions. In order to leverage the special structure of these Manhattan scenes we must identify these three canonical directions. Since these directions are assumed to be orthogonal to one another, identifying them is equivalent to finding a 3–dimensional rotation R_w that maps them onto the x, y, and z axes.

We assume that an estimate of the camera pose for each frame is available, such as might be provided by a structure–from–motion system. We will not use any point cloud generated from structure–from–motion in this chapter. We assume that the provided camera poses are measured in a fixed but arbitrary coordinate frame. Determining R_w in the context of a single image is equivalent to detecting vanishing points since three vanishing points and a calibrated camera are sufficient to recover R_w. However, in the multiple view context it makes sense to estimate R_w jointly using all available information, rather than to merge single–view estimates post–hoc. One view of the contribution of this chapter is therefore as a generalisation of vanishing point detection to multiple calibrated views.

We estimate R_w using the assumption that a significant number of the observed line segments correspond to one of three Manhattan orientations. We present a graphical model relating line segments to R_w, then we present an Expectation–Maximisation algorithm for inference within this model. Our likelihoods are derived from a well–defined model of image formation, and we optimise jointly with respect to all line segments in all views in a single optimisation. Our approach parallels ideas presented in the context of single–view vanishing point detection, particularly those of Andrew Zisserman [29] and Frank Dellaert [60]. Our contribution is a principled way to incorporate multiple calibrated views into a single optimisation, and an empirical demonstration that doing so significantly out–performs both single–view vanishing point estimation and surface–normal–based estimators.

5.2 Background

Vanishing point detection has a long history in the computer vision literature, beginning with the seminal work of Barnard *et al.* [4]. In this section we survey key contributions within this literature and discuss their relationship to our work.

5.2.1 Single View Approaches

Several approaches to single–image vanishing point detection have been proposed in the literature [4, 42, 62]. Common among all such approaches is the use of line segments as the fundamental observation from which inference is performed. The vanishing points under consideration are assumed to generate several associated line segments, all of which meet at the vanishing point (modulo measurement errors). The estimation of vanishing points is approached in various ways. The classic approach due to Barnard [4] was to project images onto the Gaussian sphere and use the Hough transform to identify vanishing points. Several authors have proposed similar voting schemes under different parametrisations of the accumulator space that improve statistical robustness.

Shufelt [62] introduced explicit error models for observed line segments, but retained the voting–based estimation strategy. Hartley and Zisserman [29] first proposed a generative model relating vanishing point to line segments and cast maximum likelihood estimation as a non–linear estimation problem. We make similar modelling assumptions in the present work. Kanatani [39] minimised the algebraic deviation of vanishing points from observed line segments, which leads to an efficient linear least–squares solution at the cost of a less precise error model. Schinder and Dellaert [60] laid out an integrated Bayesian approach to the estimation of multiple vanishing points.

The approaches discussed thus far estimate vanishing points independently, using K–means clustering or the expectation maximisation algorithm to resolve the assignment of line segments to vanishing points. Coughlan and Yuille [12] observed that under the Manhattan world

assumption the three cardinal vanishing points are mutually orthogonal and hence their locations in the image plane are highly correlated. Rather than estimating three independent vanishing points, the authors cast the estimation problems in terms of Euler angles corresponding to R_w, resulting in a three–DoF estimation problem in place of the 6 for independent vanishing point estimation. Kosecká and Zhang [42] showed that the Manhattan world assumption can be exploited even in the case of an uncalibrated camera. Their approach used a prior on camera intrinsics to condition the estimation process, though the estimation of three vanishing points was not explicitly coupled after this stage.

Denis *et al.* [16] took this a step further by exploiting a prior on the rotation R_w learned from training data. Whereas Coughlan and Yuille used a discretisation of the space of rotations to identify R_w, they showed how to exploit the Manhattan world assumption under the more principled Expectation–Maximisation approach of Schindler and Dellaert [60]. The M–step in their approach is a non–linear optimisation over rotations, leveraging the maximum likelihood reprojection error of Hartley and Zisserman[29].

Sinha *et al.* [63] show how vanishing points in different views can be optimised jointly with structure and motion inside a single bundle adjustment. Their approach fixes the line/vanishing–point associations using multi–hypothesis RANSAC in individual views. Structure, motion, and vanishing directions are then optimised jointly while holding the data associations fixed. Our approach differs from theirs in that (1) we optimise the data association variables linking lines to vanishing points jointly with the vanishing point locations; and (2) we do not refine structure and motion using the vanishing points.

Mirzaei and Roumeliotis [50] showed that minimising the algebraic error for three mutually orthogonal vanishing points can be solved globally using a polynomial solver. Their approach assumes the algebraic error; it is not clear whether the reprojection error leads to a likelihood that is amenable to a polynomial solution.

Bazin *et al.* [5] recently proposed a novel globally–optimal vanishing point algorithm based on branch–and–bound. They search over partitions of the observed line segments, constrained by

the requirement that each partition must be consistent with some vanishing point to a tolerance τ. This approach is attractive because it is guaranteed to find the global optimum. The authors optimise an objective function based on the number of consistent line segments, whereas most previous approaches optimise a log–likelihood.

5.2.2 Multiple View Approaches

The literature concerning vanishing point estimation from multiple views is sparse, and generally involves non–photometric approaches to recover R_w. Furukawa and Curless [26] use multiple–view stereo to recover a dense point cloud, then estimate R_w by clustering surface normals on the unit hemisphere. Werner and Zisserman [73] identify vanishing points independently in several uncalibrated views, then resolve associations between views using a combinatorial search.

5.3 Overview of Proposed Approach

Reliable vanishing point detection from single images is fundamentally challenging in environments in which axis–oriented edges are rare, or in which one or two cardinal orientations have very few associated edges. Both scenarios are common in video sequences of indoor environments since the camera often views only a small portion of the scene. On the other hand, obtaining a dense reconstruction is a complex and computationally expensive pre–requisite for a three–parameter estimation problem. Furthermore, the point cloud provided by on–line structure–from–motion is too sparse to obtain accurate surface normal estimates.

We overcome these difficulties by reasoning in terms of line segments and integrating observations from many frames into the estimation. Since R_w is fixed for all frames it makes sense to leverage all available data during estimation. Whereas previous approaches often estimate vanishing points as a precursor to reconstructing camera poses [42, 73], we prefer to rely on the structure–from–motion system to provide camera poses, then recover vanishing points after-

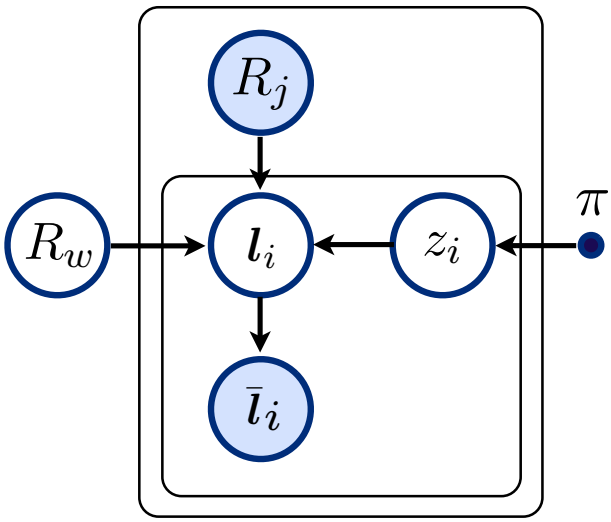

Figure 5.1: A graphical model relating line segments to vanishing points.

wards. Under this problem setup we can relate line segments in all views directly to R_w and therefore incorporate all available evidence into a joint estimation. We show that this is both computationally efficient and avoids the fragile single–view estimation scenario.

The structure–from–motion system we have chosen to work with is the parallel tracking and mapping (PTAM) approach of Klein and Murray [40]. This approach is suitable for online experiments, although this comes at the cost of reduced accuracy compared to global bundle adjustment. Importantly, PTAM can encounter scale and orientation drift, so the maps it builds may not be perfectly metric. While our results with this system are promising, we do notice small vanishing point inconsistencies between frames, which can lead to errors in our reconstructions. When operating offline, this could be alleviated by running global bundle adjustment prior to executing our system.

5.4 Generative Model

We assume the graphical model shown in Figure 5.1. The generative process operates as follows. First we sample a scene orientation R_w and the rotation component of the camera pose, R_j for each frame. (Camera translation plays no part when reasoning about vanishing points.) Next we sample a discrete variable z_i from a categorical distribution with mixing parameters

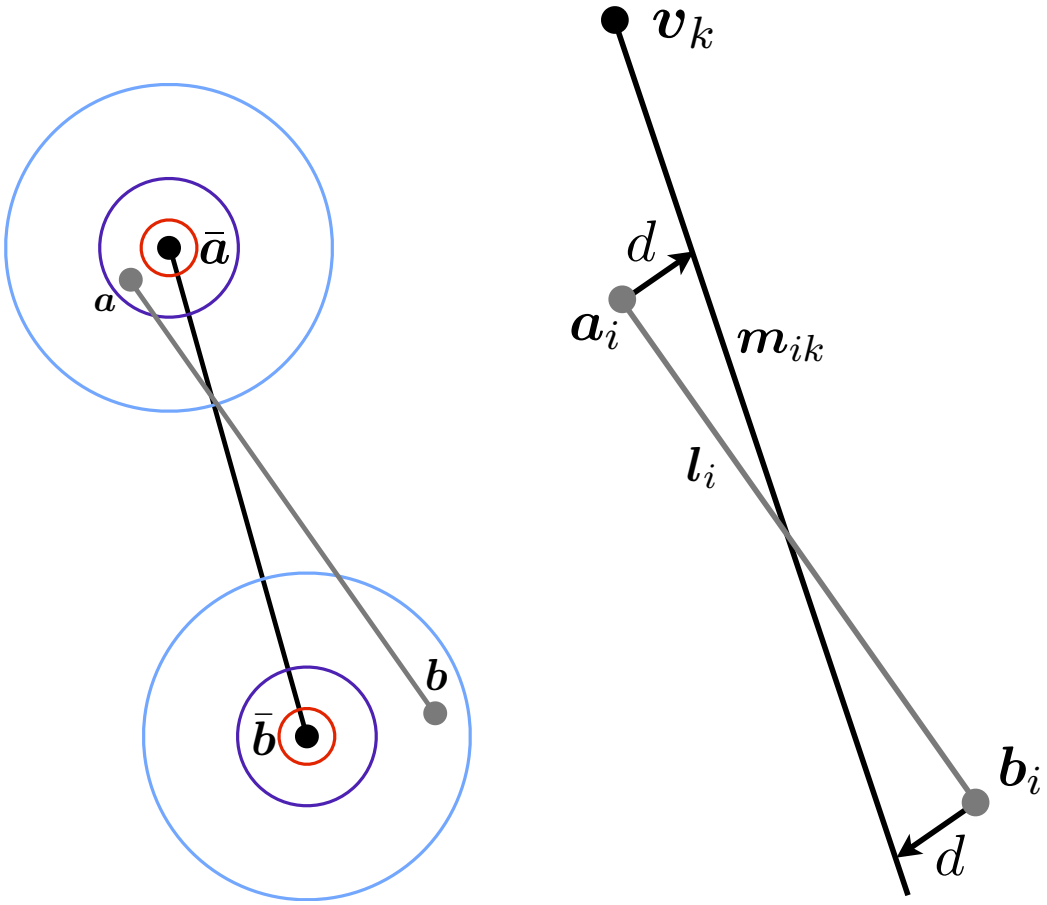

(a) Error model for line observations.

(b) The reprojection error, d.

Figure 5.2: Illustration of our error model and various geometric quantities involved in the derivations in the main text.

π. The variable z_i is a binary vector of length 4 indicating which vanishing point each line segment is associated with. Exactly one element is set to 1, the other three are 0. The first three elements correspond to the three vanishing points, the fourth to a spurious observation not associated with any of the three Manhattan directions. We denote the (binary) value of the k^{th} element z_{ik}, but we will also write $z_i = k$ as shorthand for the event that z_i is the binary vector with the k^{th} element set to 1. For clarity we write $z_i = \mathsf{sp}$ in place of $z_i = 4$. If $z_i = \mathsf{sp}$ then the line segment $\bar{\boldsymbol{l}}_i$ is sampled uniformly from the image. Otherwise, $\bar{\boldsymbol{l}}_i$ is associated with the vanishing point $\boldsymbol{v}_{z_i}$ and is sampled as follows.

The vanishing point corresponding to z_i is

$$\boldsymbol{v}_{z_i} = R_j R_w \boldsymbol{e}_{z_i} \ . \tag{5.1}$$

We sample a ray through $\boldsymbol{v}$, then sample a line segment $\bar{\boldsymbol{l}} = (\bar{\boldsymbol{a}}, \bar{\boldsymbol{b}})$ along the ray. We add isotropic Gaussian noise to arrive at the measured line segment $\boldsymbol{l} = (\boldsymbol{a}, \boldsymbol{b})$:

$$\boldsymbol{a} \sim \mathcal{N}(\bar{\boldsymbol{a}}, \Sigma) \tag{5.2}$$

$$\boldsymbol{b} \sim \mathcal{N}(\bar{\boldsymbol{b}}, \Sigma) \ . \tag{5.3}$$

This process is illustrated by the graphical model in Figure 5.1.

The likelihood for line segments is

$$P(\boldsymbol{l}_i \mid z_i, R_w) = \mathcal{N}(d(\boldsymbol{l}_i, \boldsymbol{v}_{z_i}); 0, \sigma) \tag{5.4}$$

where $d(\boldsymbol{l}, \boldsymbol{v})$ is the reprojection error illustrated in Figure 5.2. d is computed as follows. First, draw a line between the vanishing point $\boldsymbol{v}$ and the mid–point of the line segment $\boldsymbol{l}$,

$$\boldsymbol{m}_{ik} = \boldsymbol{v}_k \times \frac{\boldsymbol{a}_i + \boldsymbol{b}_i}{2} \tag{5.5}$$

Now, d is the distance between the line $\boldsymbol{m}$ and either of the two end points of $\boldsymbol{l}$ (the two quantities are equal, as evident by inspecting Figure 5.2). So

$$d(\boldsymbol{l}_i, \boldsymbol{v}_k) = \frac{\boldsymbol{a}_i \cdot \boldsymbol{m}_{ik}}{(\boldsymbol{a}_i \cdot \boldsymbol{e}_3)\eta_{ik}} \tag{5.6}$$

$$\eta_{ik} = \sqrt{(\boldsymbol{m}_{ik} \cdot \boldsymbol{e}_1)^2 + (\boldsymbol{m}_{ik} \cdot \boldsymbol{e}_2)^2} \ . \tag{5.7}$$

5.5 Estimating the Manhattan Coordinate Frame

We now turn to the inference algorithm that we use to find the maximum–likelihood estimate of R_w under the probabilistic assumptions described in the previous section. We begin by

running the Canny edge detector [9], followed by an edge linking algorithm [42] to identify a set of straight line segments $\boldsymbol{l}_j = \{\boldsymbol{p} : \boldsymbol{l}_j \cdot \boldsymbol{p} = 0\}$.

Under the model presented in the previous section, the likelihood of R_w is

$$P(L \mid R_w, \{R_i\}) = \int P(L, Z \mid R_w, \{R_i\}) \, \mathrm{d}Z \, . \tag{5.8}$$

For brevity we will omit the camera poses $\{R_i\}$ in the remainder of this section; it may be assumed that all probabilities to follow are conditioned on $\{R_i\}$.

The indicators Z are latent variables over which we need to marginalise in order to perform inference on R_w. Integrating explicitly is intractable so we turn to the expectation–maximisation (EM) algorithm, which alternately refines estimates of the posterior on Z (the "E–step") and R_w (the "M–step").

Due to the iterative nature of the EM algorithm we adopt superscript notation for the scene rotation and indicators to make clear the dependence between successive time steps. R_w^t is the estimate of the scene rotation at time t and q^t is the estimate for the posterior on Z at time t. Note that the former is an estimate of a variable but the latter is an estimate of a distribution. For notational convenience we will treat q as a continuous function, though of course in practice we really just store sufficient statistics for q. Also note that we never actually store or estimate the values of the indicators Z, so we have no need for superscripts on this variable. Although Z does appear in the derivations to follow, in every equation we are either marginalising it out, or defining a function over it.

5.5.1 Complete Data Likelihood

In sections to follow we will need to deal with the complete data likelihood,

$$P(L, Z \mid R_w) = \prod_i P(\boldsymbol{l}_i, z_i \mid R_w) \tag{5.9}$$

The likelihood terms $P(\boldsymbol{l}_i, z_i \mid R_w)$ depend on z_i in a complicated way, since $\boldsymbol{l}_i$ is drawn from a different distribution depending on z_i:

$$P(\boldsymbol{l}_i, z_i \mid R_w) = P(z_i \mid R_w)\, P(\boldsymbol{l}_i, \mid z_i, R_w) \tag{5.10}$$

$$= \begin{cases} \pi_1 \mathcal{N}\big(d(\boldsymbol{l}_i, R_i R_w \boldsymbol{e}_1); 0, \sigma\big), & \text{if } z_i = 1 \\ \pi_2 \mathcal{N}\big(d(\boldsymbol{l}_i, R_i R_w \boldsymbol{e}_2); 0, \sigma\big), & \text{if } z_i = 2 \\ \pi_3 \mathcal{N}\big(d(\boldsymbol{l}_i, R_i R_w \boldsymbol{e}_3); 0, \sigma\big), & \text{if } z_i = 3 \\ \pi_{\mathsf{sp}} \frac{1}{Z_{\mathsf{sp}}}, & \text{if } z_i = \mathsf{sp}\ . \end{cases} \tag{5.11}$$

Due to our definition of z_i as a binary vector we can express this likelihood in the following analytic form,

$$P(\boldsymbol{l}_i, z_i \mid R_w) = \prod_{k=1}^{4} \Big(P(\boldsymbol{l}_i \mid z_i = k, R_w) P(z_i = k \mid R_w) \Big)^{z_{ik}}\ . \tag{5.12}$$

5.5.2 The E–step

During this phase we compute sufficient statistics for the posterior on the indicators given a fixed estimate of R_w. This posterior is

$$q^t(Z) = P(Z \mid L, R_w^t) \tag{5.13}$$

$$= \frac{\prod_i P(\boldsymbol{l}_i, z_i \mid R_w^t)}{\int \prod_i P(\boldsymbol{l}_i, z_i \mid R_w^t)\, \mathrm{d}Z} \tag{5.14}$$

Consider the term on the top line,

$$P(\boldsymbol{l}_i, z_i \mid R_w^t) = P(\boldsymbol{l}_i \mid z_i, R_w^t) P(z_i \mid R_w^t)\ . \tag{5.15}$$

As a function of z_i this is simply a categorical distribution: z_i can take on 3 possible values, and we can compute each explicitly since R_w^t and $\boldsymbol{l}_i$ are fixed. Now since equation (5.14) is a normalised concatenation of categorical distributions, it is itself a categorical distribution,

meaning that the sufficient statistics for q^t are the expectations

$$\begin{aligned}
\mathbb{E}_{q^t}\left[z_{ik}\right] &= \int z_{ik} q^t(Z)\,\mathrm{d}Z && (5.16)\\
&= \sum_{z_{ik}\in\{0,1\}} z_{ik} P(z_{ik} \mid \boldsymbol{l}_i, R_w^t) && (5.17)\\
&= P(z_i = k \mid \boldsymbol{l}_i, R_w^t) && (5.18)\\
&= \frac{P(\boldsymbol{l}_i, z_i = k \mid R_w^t)}{\sum_{j=0}^{4} P(\boldsymbol{l}_i, z_i = j \mid R_w^t)} && (5.19)
\end{aligned}$$

where in the third line we have expanded the sum over the two possible values for z_{ik} and cancelled the one in which z_{ik} is 0. Substituting the specific forms for the the complete data likelihood (5.12),

$$\begin{aligned}
\mathbb{E}_{q^t}\left[z_{ik}\right] &= \frac{\prod_{k=1}^{4}\Big(P(\boldsymbol{l}_i \mid z_i = k, R_w^t)P(z_i = k \mid R_w^t)\Big)^{z_{ik}}}{\sum_{z_i=1}^{4}\prod_{k=1}^{4}\Big(P(\boldsymbol{l}_i \mid z_i = k, R_w^t)P(z_i = k \mid R_w^t)\Big)^{z_{ik}}} && (5.20)\\
&= \frac{\Big(\pi_{\mathsf{sp}} P(\boldsymbol{l}_i \mid z_i = \mathsf{sp}, R_w^t)\Big)^{z_{ik}} \prod_{k=1}^{3}\Big(\pi_k P(\boldsymbol{l}_i \mid z_i = k, R_w^t)\Big)^{z_{ik}}}{\sum_{z_i=1}^{4}\left[\Big(\pi_{\mathsf{sp}} P(\boldsymbol{l}_i \mid z_i = \mathsf{sp}, R_w^t)\Big)^{z_{ik}} \prod_{k=1}^{3}\Big(\pi_k P(\boldsymbol{l}_i \mid z_i = k, R_w^t)\Big)^{z_{ik}}\right]}. && (5.21)
\end{aligned}$$

We now define

$$\begin{aligned}
\rho_i &= \pi_{\mathsf{sp}} P(\boldsymbol{l}_i \mid z_i = \mathsf{sp}, R_w^t) && (5.22)\\
s_i &= \begin{cases} 1, & \text{if } z_i = \mathsf{sp} \\ 0, & \text{otherwise} \end{cases} && (5.23)
\end{aligned}$$

and substituting into (5.21) we have

$$\mathbb{E}_{q^t}\left[z_{ik}\right] = \frac{\rho_i^{s_i}\left(\pi_{z_i}\mathcal{N}(d(\boldsymbol{l}, R_i R_w^t \boldsymbol{e}_k); 0, \sigma)\right)^{1-s_i}}{\sum_{z_i=1}^{4} \rho_i^{s_i}\left(\pi_{z_i}\mathcal{N}(d(\boldsymbol{l}, R_i R_w^t \boldsymbol{e}_{z_i}); 0, \sigma)\right)^{1-s_i}} \tag{5.24}$$

$$= \frac{\rho_i^{s_i}\left(\pi_{z_i}\mathcal{N}(d(\boldsymbol{l}, R_i R_w^t \boldsymbol{e}_k); 0, \sigma)\right)^{1-s_i}}{\rho_i + \sum_{z_i=1}^{3}\left(\pi_{z_i}\mathcal{N}(d(\boldsymbol{l}, R_i R_w^t \boldsymbol{e}_{z_i}); 0, \sigma)\right)}\,. \tag{5.25}$$

The E–step therefore consists of computing the expectations for each indicator according to (5.25), which are sufficient statistics for the posterior on Z. The expression above can be evaluated for each indicator in constant time, leading to a complexity for the E–step linear in the number of observed line segments.

5.5.3 M–step

During this phase we compute R_w^{t+1} as the maximiser of the expectation of the complete data log–likelihood under the (fixed) distribution q^t. The logarithm of the complete data log–likelihood (5.12) is

$$\log P(L, Z \mid R_w) = \sum_i \sum_{k=1}^{4} z_{ik}\Big(\log P(\boldsymbol{l}_i \mid z_i = k, R_w) + \log P(z_i = k \mid R_w)\Big) \tag{5.26}$$

$$= \sum_i \sum_{k=1}^{4} z_{ik}\Big(\log \mathcal{N}(d(\boldsymbol{l}_i, R_i R_w \boldsymbol{e}_k); 0, \sigma) + \log \pi_k\Big) \tag{5.27}$$

$$= \sum_i \sum_{k=1}^{4} z_{ik}\Big(\frac{-d(\boldsymbol{l}_i, R_i R_w \boldsymbol{e}_k)^2}{2\sigma^2} + \log \pi_k\Big) + c \tag{5.28}$$

where c is a constant arising from the logarithm of the normal distribution, which we now drop since it plays no part in the maximisation to follow. The expectation of the above with respect

to the distribution q^t is

$$\mathbb{E}_{q^t}\Big[\log P(L, Z \mid R_w)\Big] = \sum_i \sum_{k=1}^{4} \mathbb{E}_{q^t}\big[z_{ik}\big]\Big(\frac{-d(\boldsymbol{l}_i, R_i R_w \boldsymbol{e}_k)^2}{2\sigma^2} + \log \pi_k\Big) \tag{5.29}$$

$$= \sum_i \sum_{k=1}^{4} r_{ik}^t\Big(\frac{-d(\boldsymbol{l}_i, R_i R_w \boldsymbol{e}_k)^2}{2\sigma^2} + \log \pi_k\Big) \tag{5.30}$$

where in the last line we have defined and substituted

$$r_{ik}^t = \mathbb{E}_{q^t}\big[z_{ik}\big] \,. \tag{5.31}$$

The maximisation we wish to perform is

$$R_w^{t+1} = \operatorname*{argmax}_{R_w} \mathbb{E}_{q^t}\Big[\log P(L, Z \mid R_w)\Big] \,. \tag{5.32}$$

It is worth examining the expression being maximised and noting which variables it is and is not a function of. During each M–step, the distribution q^t, as represented by the sufficient statistics computed in the E–step, is held fixed. The expectation is over all possible values of the indicators Z, each weighted according to q^t, which was computed from the previous estimate R_w^t but does not depend on the quantity R_w being maximised in this step. Hence the expression being maximised in (5.32) is a function of R_w alone. Substituting (5.30),

$$R_w^{t+1} = \operatorname*{argmax}_{R_w} f(R_w) \tag{5.33}$$

$$f(R_w) = \sum_i \sum_{k=1}^{4} r_{ik}^t\Big(\frac{-d(\boldsymbol{l}_i, R_i R_w \boldsymbol{e}_k)^2}{2\sigma^2} + \log \pi_k\Big) \,. \tag{5.34}$$

Importantly, note that r_{ik}^t is a constant with respect to R_w in the above. We perform the maximisation (5.32) by gradient descent. Differentiating (5.34) with respect to R_w,

$$\frac{\partial f}{\partial R_w} = \sum_i \sum_{k=1}^{4} r_{ik}^t\Big(\frac{-d_{ik}}{\sigma^2}\frac{\partial d_{ik}}{\partial R_w}\Big) \tag{5.35}$$

$$\frac{\partial d_{ik}}{\partial R_w} = \frac{1}{\boldsymbol{a}_i \cdot \boldsymbol{e}_3}\left(\frac{(\boldsymbol{m}_{ik})_1 \boldsymbol{e}_1 + (\boldsymbol{m}_{ik})_2 \boldsymbol{e}_2}{{\eta_{ik}}^3}(\boldsymbol{m}_{ik} \cdot \boldsymbol{a}_i) - \frac{\boldsymbol{a}_i}{\eta_{ik}}\right)\Big[\frac{\boldsymbol{a}_i + \boldsymbol{b}_i}{2}\Big]_\times \frac{\partial \boldsymbol{v}_k}{\partial R_w} \tag{5.36}$$

where

$$d_{ik} = d(\boldsymbol{l}_i, R_i R_w \boldsymbol{e}_k) \tag{5.37}$$

$$\eta_{ik} = \sqrt{(\boldsymbol{m}_{ik} \cdot \boldsymbol{e}_1)^2 + (\boldsymbol{m}_{ik} \cdot \boldsymbol{e}_2)^2} \tag{5.38}$$

and

$$[\boldsymbol{x}]_\times = \begin{bmatrix} 0 & -x_3 & x_2 \\ x_3 & 0 & -x_1 \\ -x_2 & x_1 & 0 \end{bmatrix} \tag{5.39}$$

is the matrix form for the cross product.

For the purpose of optimisation we write R_w as the product of a fixed part R_0 and a variable part R_δ, the latter of which is represented in the Lie algebra for the special orthogonal group $SO(3)$, so

$$R_w = R_0 R_\delta \tag{5.40}$$

$$R_\delta = \exp\Big(\sum m_i G_i\Big) \tag{5.41}$$

where the G_i are the generator matrices for $SO(3)$ and the m_i provide a minimal representation for the 3D rotation matrix group. The advantage of using this representation is that after each gradient step we are guaranteed that R_w remains a pure rotation, unlike under other representations such as optimising the elements of the 3×3 rotation matrix directly. Differentiating $\boldsymbol{v}$ with respect to $\boldsymbol{m}$ yields

$$\frac{\partial \boldsymbol{v}_k}{\partial \boldsymbol{m}} = R_i \frac{\partial R_w}{\partial \boldsymbol{m}} \boldsymbol{e}_k \,. \tag{5.42}$$

The division of R_w into fixed and variable parts allows us to evaluate the gradient at $\boldsymbol{m} = 0$ without loss of generality. In this case,

$$\left.\frac{\partial \boldsymbol{v}_k}{\partial \boldsymbol{m}}\right|_{\boldsymbol{m}=0} = \begin{bmatrix} R_i R_0 G_1 \boldsymbol{e}_k & R_i R_0 G_2 \boldsymbol{e}_k & R_i R_0 G_3 \boldsymbol{e}_k \end{bmatrix} \,. \tag{5.43}$$

This completes the derivation of the gradient of the error function f with respect to the parametri-

sation $\boldsymbol{m}$. We proceed as normal with gradient steps of the form

$$\boldsymbol{m}^{t+1} = \boldsymbol{m}^t - \gamma \frac{\partial f}{\partial \boldsymbol{m}} \,. \tag{5.44}$$

Due to the low dimensionality of the search space and relatively low curvature of the error function we found that a simple instantiation of the gradient descent algorithm converged quickly and robustly. Our algorithm initialises the step size γ to a fixed constant γ_0 at the beginning of each M–step, then divides γ by 2 each time that an update leads to an increase in the error function. Convergence is detected when $\gamma < \epsilon_1$ and the value of the error function decreases by less than ϵ_2 in any one update.

5.5.4 Initialisation

We initialise our EM algorithm using the clustering approach described by Koseckà and Zhang [42]. This process begins by clustering observed line segments according to their orientation in the image plane, the basis for this being that Manhattan environments often contain Manhattan–oriented lines that are close to one another (relative to the distance to the vanishing point), and hence appear almost parallel. We run K–means clustering on all line segments in each image separately (with $K = 5$) then we estimate a least–squares vanishing point for each cluster that has at least 5 associated line segments. Finally we project vanishing points from all frames onto the plane at infinity and pick three that are close to mutually orthogonal (by enumerating all combinations). We initialise the EM algorithm with an (orthonormalized) rotation matrix containing the chosen vanishing points as columns.

5.5.5 Summary

To obtain R_w we iterate between updating q (the E–step) and optimising R_w (the M–step). Each M step consists of a gradient descent in the Lie group $SO(3)$. In practice we find that our system converged in around 25 iterations of the EM algorithm, and that approximately 10 steps were

required for each gradient descent.

5.6 Results

We evaluated our approach using a dataset of 18 video sequences of 8 unique places, which we collected in indoor environments such as homes and office spaces. We ran an off–the–shelf bundle adjuster on each sequence to yield calibrated views, then transformed each sequence by a random 3D rotation to eliminate any bias in the initial conditions for our optimisation that might have been introduced by structure–from–motion. We manually provided the ground truth scene orientation R_w for each sequence. We sampled frames at regular intervals of approximately one second, then divided all sequences into successive 7–frame blocks. Each such block is a single "evaluation instance" in our dataset.

We compared four approaches including our own. First, the surface–normal–based approach of [26] described at the beginning of this chapter, which we refer to by symbol "NRM". For each evaluation instance, this algorithm received as input all reconstructed 3D points that were visible in any of the 7 views in that instance. We were generous to this approach here since the reconstruction of some of these points may have relied upon data from other frames. Second, we tested a system identical to ours but in which the reconstruction error was replaced by the algebraic error — we refer to this system as "ALG" below. Finally, we evaluated our own system using both a single input view ("SIN"), and all 7 views ("MUL"). The former approach is hence similar to that of Schindler and Dellaert [60].

The metric we used to compare the estimated and ground truth rotations was

$$\|R_1^T R_2 - I\|_{\mathcal{F}} \,. \tag{5.45}$$

where $\|\cdot\|_{\mathcal{F}}$ denotes the Frobenius norm. We chose this metric because it was shown by Huynh [36] to be iso–equivalent to many 3D rotation metrics in common usage within the computer vision literature, including quaternion norms and inner products, and metrics based on Euler

angles and the Lie algebra $so(3)$.

Table 5.1 summarises the performance of each algorithm. Unsurprisingly, the surface normal approach fails under the sparse structure–from–motion point clouds — it was proposed in the context of dense reconstructions. Strikingly, the multiple–view algebraic minimiser performs consistently worse than single–image estimation. Our investigations suggest that this is because the algebraic error is an even poorer approximation to the reprojection error in the multiple view context than in the single–view context, since among many frames there is a high likelihood of observing a vanishing point close to infinity. As a vanishing point moves towards infinity, the algebraic error diverges from the reprojection error, and the error terms for vanishing points near infinity to dominate the objective function. This leads to poorly reconstructed vanishing points since the optimisation focuses almost exclusively on these very large error terms, ignoring the majority of the image evidence.

We ran a separate experiment to explore the relationship between the number of frames used for estimation and the quality of the estimated rotation; these results are shown in Figure 5.3. As the number of frames used for estimation increases, the quality of the estimator described in this chapter improves as expected. However, it is interesting to note that the algebraic minimiser actually degrades for more than 5 input frames. This supports our hypothesis above that the algebraic error is an even poorer choice in the multiple–view context than for single images.

Our third experiment explored the convergence properties of the gradient descent component of our optimisation. Starting from an initial rotation a specified distance from the ground truth, we plotted the progress of our algorithm after each gradient step (Figure 5.4). In this experiment the indicators Z were assumed known. Progress was measured both in terms of the log–likelihood, which the optimiser itself has access to (lower figure), and distance to ground truth, which the optimiser obviously does not have access to (upper figure). This experiment shows two things. First, that the basin of attraction is very wide — convergence is robust for distances up to 1.0, which is a large distance in the metric (5.45). Second, that the log-likelihood accurately tracks the ground truth error in practice, since the runs that did not converge to the

Sequence	Error for NRM	Error for ALG	Error for SIN	Error for MUL
Kitchen	0.53	0.59	0.037	**0.019**
Foyer 1	0.72	0.77	0.054	**0.039**
Foyer 2	0.81	0.75	0.070	**0.021**
Bursary	0.50	0.53	0.067	**0.030**
Ground	0.90	0.68	**0.55**	0.66
Atrium	0.84	1.00	0.31	**0.16**
MCR	0.56	0.56	0.06	**0.04**
Corridor	0.58	0.78	**0.20**	0.21

Table 5.1: Distance between estimated and ground truth rotation for four algorithms. Each cell shows the average error over all frames within a given sequence. From left to right the algorithms are the point–cloud procedure of [26] (NRM), Expectation–Maximisation using the algebraic error (ALG), Expectation–Maximisation using the geometric error applied to single (SIN) and multiple (MUL) images. All algorithms other than SIN were given 7 input frames in this experiment.

ground truth also terminated at much lower log–likelihoods.

Finally, examples of the output from the four systems described above are shown in Figures 5.5, 5.6, and 5.7.

5.7 Identifying The Vertical Direction

Of the three dominant directions defined by R_w, two correspond to horizontal directions and the third to the vertical direction. The latter is semantically distinct since it defines the orientation of the ground and ceiling planes, as well as the direction in which gravity operates. It is easy to identify the vertical axis since humans necessarily move over the ground plane when capturing video sequences, and have limited scope for moving the camera in the up–down direction. We therefore set the vertical axis to that over which camera positions range the least. Having identified R_w there are only three possible choices, and we found this heuristic to work correctly in all of our evaluation sequences.

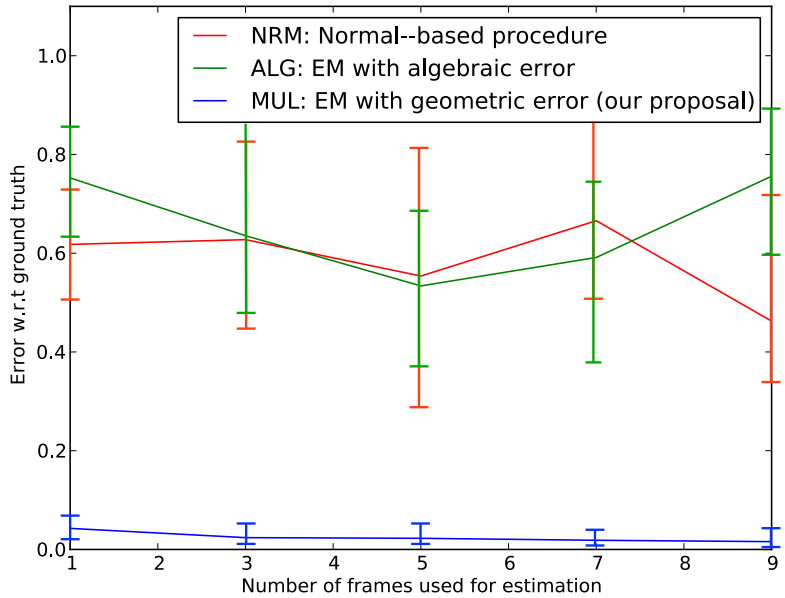

(a) Estimation error versus number of input frames.

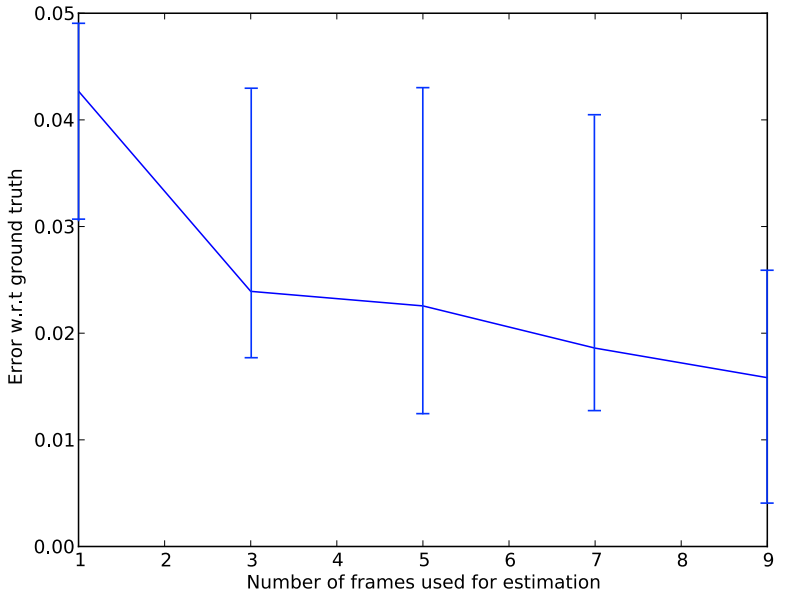

(b) A magnification of the third series above.

Figure 5.3: Plots showing the performance of three algorithms as the number of input frames is increased. We compute each data point by executing the relevant algorithm on sets of n consecutive frames drawn from our dataset, where n is the value shown on the x–axis. The y–axis shows the average distance between the estimated and ground truth rotation, with error bars showing 90% confidence intervals for the observed error distributions.

5.8 Identifying The Floor And Ceiling Planes

An indoor Manhattan scene has exactly one floor and one ceiling plane, both with normal $\boldsymbol{v_v}$. It will be useful in the following chapters to have available the mapping H_a between the image locations of ceiling points the floor points that are vertically below them (see Figure 5.8). H_a is a planar homology with axis $\boldsymbol{h} = \boldsymbol{v_l} \times \boldsymbol{v_r}$ and vertex $\boldsymbol{v_v}$ [13] and can be recovered given the image location of any pair of corresponding floor/ceiling points $(\boldsymbol{p_f}, \boldsymbol{p_c})$ as

$$H_a = I + \mu \frac{\boldsymbol{v_v} \boldsymbol{h}^T}{\boldsymbol{v_v} \cdot \boldsymbol{h}} \,, \tag{5.46}$$

where

$$\mu = \left\langle \boldsymbol{v_v}, \boldsymbol{p_c}, \boldsymbol{p_f}, \boldsymbol{p_c} \times \boldsymbol{p_f} \times \boldsymbol{h} \right\rangle \tag{5.47}$$

is the characteristic cross ratio of H_a. Although we do not have *a priori* any such pair $(\boldsymbol{p_f}, \boldsymbol{p_c})$, we can recover H_a using the following sampling algorithm. First we identify edges in the image using one of the many available edge detection algorithms. Next we sample one edge pixel $\hat{\boldsymbol{x}}_{\boldsymbol{c}}$ from the region above the horizon, then we sample a second point $\hat{\boldsymbol{x}}_{\boldsymbol{f}}$ collinear with the first and $\boldsymbol{v_v}$ from the region below the horizon. We then compute a hypothesis for $\hat{H}_a$ as described above, and then assign a score by counting the number of edge pixels that $\hat{H}_a$ maps onto other edge pixels. After repeating this for a fixed number of iterations we return the hypothesis with greatest score.

Many images contain either no view of the floor or no view of the ceiling. In such cases H_a is unimportant since there are no corresponding points in the image. If the best H_a output from the sampling process has a score below a threshold k_t then we set μ to a large value that will transfer all pixels outside the image bounds. H_a will then have no impact on the estimated model.

In the context of multiple views we resolve scale by identifying λ with either the maximum or minimum z component of any point in the point cloud reconstructed by structure–from–motion.

5.9 Extension: Relaxing The Manhattan World Assumption

The strong Manhattan assumption states that any pair of surfaces of interest are either parallel or orthogonal to one another. One common deviation from this is scenes with walls that are orthogonal to the floor and ceiling but not to one another. We define the weak Manhattan assumption as "the environment consists of a horizontal ground plane and corresponding ceiling plane, and a set of vertical wall segments extending continuously between them." Weakly Manhattan environments contain much of the regularity of strongly Manhattan environments, and here we discuss how to extending the approach taken in chapter to such scenes. We have not implemented this approach; we discuss these ideas as inspiration for future work.

We can deal with the weak Manhattan assumption as follows. First, we run the EM algorithm described above to obtain R_w. Next, for each line $\boldsymbol{l}_j$ marked as spurious by the EM algorithm we find its intersection with the horizon,

$$\boldsymbol{u}_j = R_w^{-T} R_i^{-T} \boldsymbol{l}_j \times \boldsymbol{e}_3 \,, \tag{5.48}$$

which would be its vanishing point if it were horizontal in the world. Vertical surfaces of a given orientation will generate identical $\boldsymbol{u}_j$ (modulo measurement error), so we may identify additional vertical orientations by clustering the intersections $\{\boldsymbol{u}_j\}$. This should be possible even with few such intersections, since the fact that all intersections are on the horizon reduces this to a one–dimensional estimation problem.

5.10 Conclusion

We have proposed a principled approach to discovering the dominant Manhattan directions given multiple calibrated views. Our likelihoods are derived from a well–defined model of image generation, and we solve inference as a single optimisation. Our work is strongly influenced by the literature on vanishing point detection and our approach parallels ideas previously proposed in the single–view context. Our contribution is a principled way to incorpo-

rate multiple calibrated views into a single optimisation, and an empirical demonstration that doing so significantly out–performs both single–view vanishing point estimation and surface–normal–based estimators.

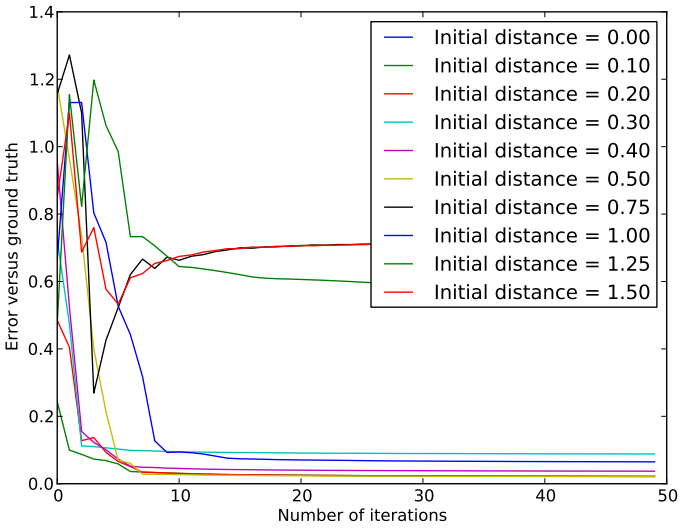

(a) Convergence of error (with respect to ground truth)

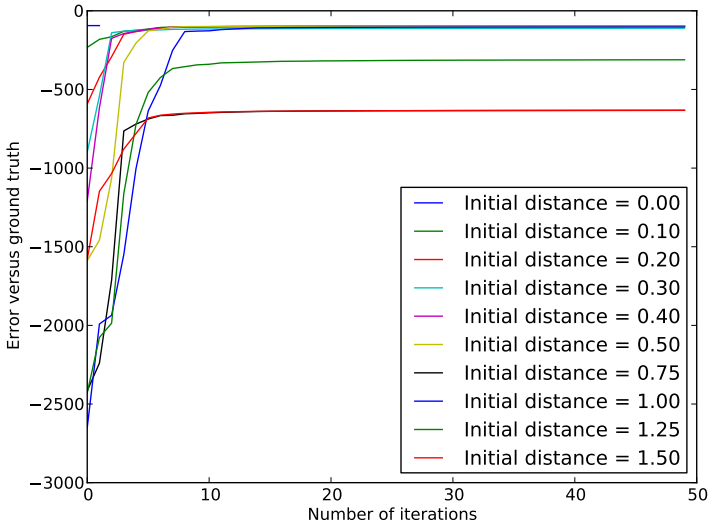

(b) Convergence of log–likelihood

Figure 5.4: Illustration of the convergence properties of our gradient descent algorithm. We measure the distance from the estimated rotation to the ground truth after each gradient step. Each series above shows this evolution when our algorithm is initialised a particular distance from the ground truth. We see that for distances less than 1 convergence is robust. This corresponds to a large offset under the metric (5.45), indicating that the optima has a wide basin of attraction. Note that for this experiment the labels Z are assumed known.

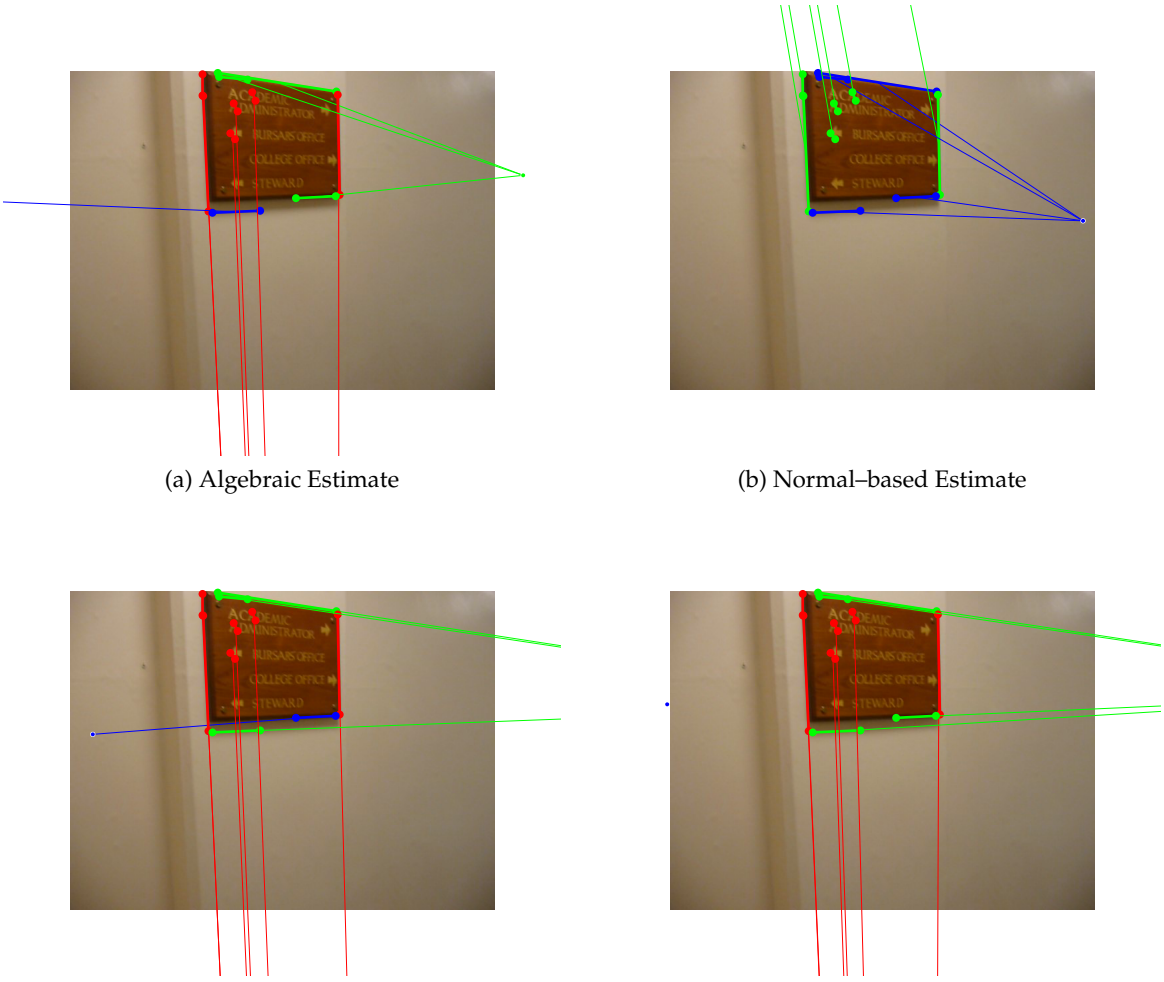

(a) Algebraic Estimate

(b) Normal–based Estimate

(c) Single Image Estimate

(d) Geometric (Proposed) Estimate

Figure 5.5: Comparison of rotation estimation algorithms for an example drawn from the "Bursary" sequence. Though only one frame is shown here, each algorithm other than (c) was provided with 7 input frames.

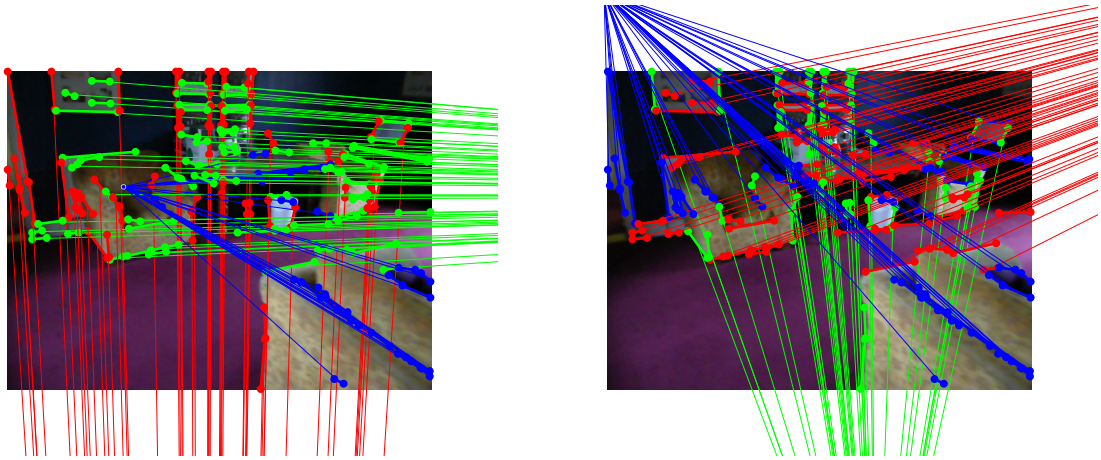

(a) Algebraic Estimate

(b) Normal–based Estimate

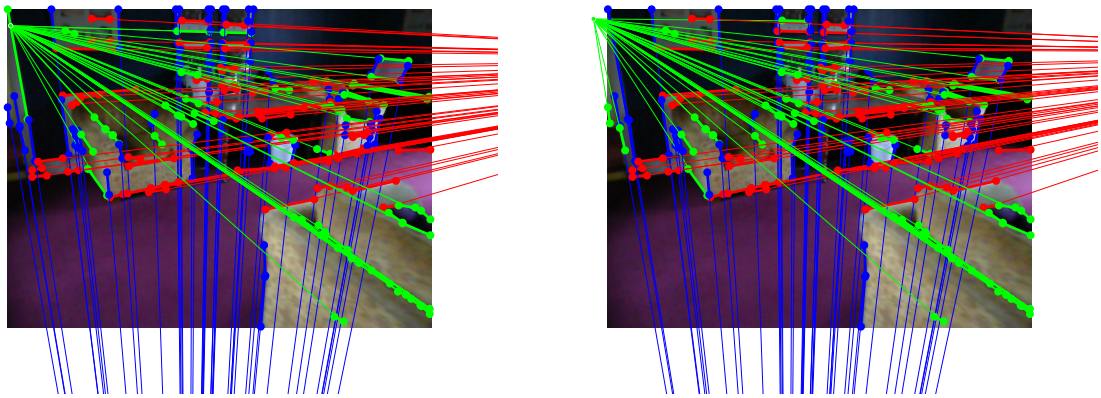

(c) Single Image Estimate

(d) Geometric (Proposed) Estimate

Figure 5.6: Comparison of rotation estimation algorithms for an example drawn from the "MCR" sequence. Though only one frame is shown here, each algorithm other than (c) was provided with 7 input frames.

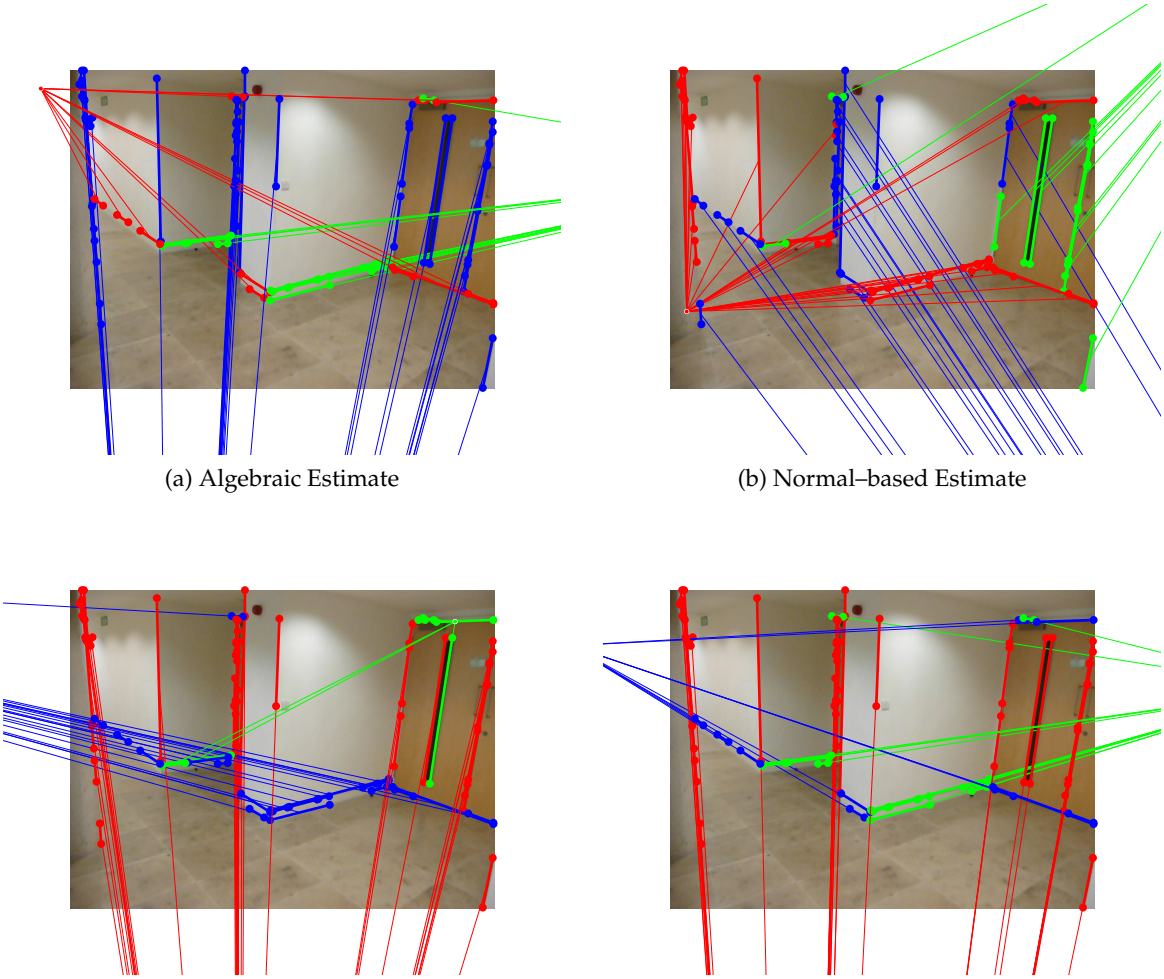

(a) Algebraic Estimate

(b) Normal–based Estimate

(c) Single Image Estimate

(d) Geometric (Proposed) Estimate

Figure 5.7: Comparison of rotation estimation algorithms for an example drawn from the "Ground1" sequence. Though only one frame is shown here, each algorithm other than (c) was provided with 7 input frames.

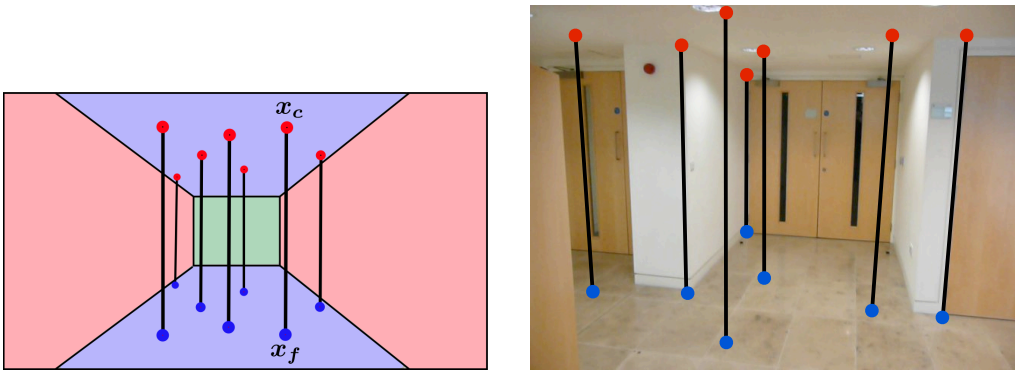

(a)

(b)

Figure 5.8: The mapping H_a transfers points between the ceiling and floor in the image domain. H_a is a planar homology.

6

Inference From Single and Multiple Views

This chapter addresses the recovery of indoor Manhattan models in the context of single and multiple views of a scene. We describe a Bayesian approach to reasoning about indoor Manhattan models in the face of ambiguous image evidence. To achieve this we present a graphical model that relates photometric cues, stereo photo–consistency, and depth cues to the scene model discussed in previous chapters. We show how to solve MAP inference using dynamic programming, allowing exact, global inference in $\sim$100 ms without using specialised hardware. Our approach is applicable to both the single– and multiple–view settings by selecting various combinations of sensor models. Experiments show our system out–performing the state–of–the–art in the domain of indoor Manhattan reconstruction.[1]

[1]This work was published in part in:
Flint, Mei, Murray, and Reid, "A Dynamic Programming Approach To Reconstruction Building Interiors", in *Proceedings of the 2010 European Conference on Computer Vision*[21]
Flint, Murray, and Reid, "Manhattan Scene Understanding Using Monocular, Stereo, and 3D Features", in *Proceedings of the 2011 International Conference on Computer Vision*[24]

Figure 6.1: Scene structure recovered by the system described in this chapter.

6.1 Introduction

Over the past decade, computer vision researchers working with monocular images have pursued substantially different research agendas to those working with multiple views. The focus for monocular images has increasingly been to infer high–level facts about the world, such as the locations of and interactions between objects, semantic scene categories, and the spatial layout of the environment. In contrast, much of the work concerning multiple views has focused on reconstructing metric scene structure and camera poses using techniques such as structure–from–motion, stereo, and multiple–view stereo.

In this chapter we leverage multiple view geometry for image understanding purposes. We assume a moving camera with a structure–from–motion system estimating its trajectory, and show how to infer semantically meaningful models of the environment. We focus on the *indoor Manhattan representation*[43, 21] that we described in Chapter 4.

Our approach is to define a probabilistic model that relates the unknown scene layout to three types of observations: photometric image features, stereo photo–consistency, and 3D point clouds. These three quantities are commonly available in a moving camera setup, but our system can be used unchanged with any combination of the three, including a single–view setting. The second part of this chapter then focuses on finding the most likely explanation for a set of observations given the assumptions made by our model. A major focus of this chapter is the development of an efficient and exact dynamic programming that solves both

maximum–aposteriori (MAP) and maximum–likelihood (ML) inference in our model.

To present these two components (model and inference algorithm) clearly, we begin by describing a class of optimisation problem that we call the payoff formulation. This optimisation problem provides the connection between the model we present first and the inference algorithm we present second. In particular, we will show during the development of the probabilistic model that MAP inference can be written as an optimisation problem in payoff form. After we have presented our model, we will thereafter be interested only in solving general payoff–form problems, which allows us to decouple the development of our dynamic programming algorithm from the specifics of our probabilistic model — we will simply show that we can solve all optimisation problems in the payoff formulation. A further advantage is that other sensor models that can be similarly reduced to payoff form will also be amenable to our dynamic programming algorithm. Although the presentation of an abstract class of optimisation problem may seem an abstruse way to begin this chapter, we believe that it leads to the clearest presentation overall.

6.2 The Payoff Formulation

In this section we describe a class of optimisation problems that we will refer to as the *payoff formulation*. Throughout the remainder of this chapter it will become clear that a range of inference problems in the context of indoor Manhattan scenes can be expressed in this form, and that this particular formulation permits a general and efficient dynamic programming solution.

Let $\mathcal{M}$ be the set of indoor Manhattan scenes in vertex representation. Let $M \in \mathcal{M}$ be a scene in vertex representation and let S be the corresponding scene in seam representation.

A payoff function $\pi : \mathcal{D} \times \mathcal{A} \to \mathbb{R}$ maps integer pixel coordinates $\boldsymbol{p} \in \mathcal{D}$ together with orientations $a \in \mathcal{A}$ to real numbers. The payoff for a scene M is defined in terms of the seam representation,

$$\Pi(M) = \Pi(S) = \sum_{j=1}^{W} \pi(j, s_j, o_j) \tag{6.1}$$

where $S = \{(s_j, o_j)\}$. This sum consists of one term for each image column. It is computed by adding together the value of the payoff function at each pixel along the floor/wall seam in M. The form of the payoff function is problem–specific; all we require is that it is a function of j, s_j, and o_j. Later we will describe specific payoff functions π for the likelihoods in our model. In cases where the payoff function is independent of o_j we will write

$$\pi(\boldsymbol{p}) = \pi(x, y, \cdot) \tag{6.2}$$

Note that the value of $\pi(\boldsymbol{p})$ is *not* restricted in any way to dependence on the image evidence at pixel $\boldsymbol{p}$, nor even to a local region about $\boldsymbol{p}$; indeed, the payoff functions described in the following sections incorporate image evidence from widely separated image regions.

A penalty function $\Gamma : \mathcal{M} \to \mathbb{R}$ maps scenes in the vertex representation to real numbers and takes the form,

$$\Gamma(M) = \sum_{i=0}^{K-1} \gamma(i; M) \tag{6.3}$$

where K is the number of walls contained in M and γ may be interpreted as a regulariser related to the meeting between the i^{th} wall in M and its successor. Once again, we have not defined any particular γ; any that takes the the form (6.3) is suitable for the optimisation problem to follow. Later we will describe specific forms for γ corresponding to particular choices of prior in our model.

Given any such Π and Γ, the associated optimisation problem is as follows. Let

$$\begin{aligned} f(M) &= \Pi(M) - \Gamma(M) && (6.4) \\ &= \sum_{j=1}^{W} \pi(j, s_j, o_j) - \sum_{i=0}^{K-1} \gamma(i; M)\ . && (6.5) \end{aligned}$$

then we seek

$$M^* = \operatorname*{argmax}_{M \in \mathcal{M}} f(M)\ . \tag{6.6}$$

Note that the objective f is defined partially in the scene representation and partially in the ver-

tex representation. This poses no difficulty to evaluating f in the vertex representation since we can readily obtain the seam representation via equation (4.47). However, as discussed in Section 4.4.3, the mapping from the vertex representation to seam representation is not invertible, so the objective above cannot be evaluated in the seam representation. For this reason we will work in the vertex representation for the presentation of the optimisation algorithm, but for convenience we will work in seam representation to define Π.

6.3 Probabilistic Model

In this section we develop a probabilistic model for estimating indoor Manhattan scenes from observations. We assume that three types of observations are available: photometric image features, calibrated stereo image pairs, and 3D point clouds. These quantities might be acquired, for example, as the output of a SLAM or structure–from–motion system. We now describe probabilistic relationships between each type of observation and the indoor Manhattan scene structure that we wish to infer.

6.3.1 Scene Prior

We turn first to the prior on scenes, $P(M \mid \boldsymbol{\lambda})$, which is governed by a set of hyper–parameters $\boldsymbol{\lambda}$. As discussed in Section 4.5.1, corners between successive walls can be classified as concave, convex, or occluding. Let n_1, n_2, and n_3 be the number of corners in M of each category respectively. Our prior on scenes is a geometric distribution in $\boldsymbol{n} = (n_1, n_2, n_3)$,

$$P(M \mid \boldsymbol{\lambda}) \quad = \quad \frac{1}{Z} {\lambda_1}^{n_1} {\lambda_2}^{n_2} {\lambda_3}^{n_3} \,, \tag{6.7}$$

where Z is a normalising term that we will not need to compute in order to perform maximisation. Our choice of (6.7) is motivated by the desire to penalise scenes for additional complexity, where we measure complexity by the number of distinct walls. We discuss other priors, and some of the problems they raise in Section 6.7.1.

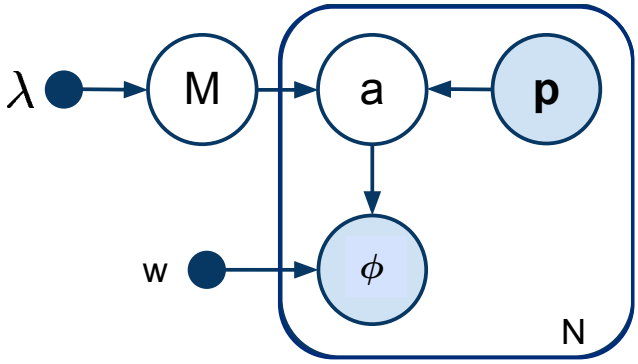

Figure 6.2: The graphical model relating scenes M to monocular image features ϕ. $\boldsymbol{p} = (x, y)$ is a pixel location and a is the orientation predicted (deterministically) by M at $\boldsymbol{p}$.

Taking logarithms yields

$$\log P(M \mid \boldsymbol{\lambda}) = -\log Z + n_1 \log \lambda_1 + n_2 \log \lambda_2 + n_3 \log \lambda_3 \,. \tag{6.8}$$

Comparison with (6.3) suggests the following penalty function:

$$\gamma(i; M) = \begin{cases} \log \lambda_1, & \text{if the } i^{\text{th}} \text{ corner in } M \text{ is concave} \\ \log \lambda_2, & \text{if the } i^{\text{th}} \text{ corner in } M \text{ is convex} \\ \log \lambda_3, & \text{if the } i^{\text{th}} \text{ corner in } M \text{ is occluding} \end{cases} \tag{6.9}$$

The cases above can be decided by the algorithm described in Section 4.5.1. Substituting (6.9) into (6.3) yields

$$\Gamma(M) = \log P(M \mid \boldsymbol{\lambda}) + \log Z \,. \tag{6.10}$$

We can safely ignore the constant term since our ultimate goal is the optimisation expressed in (6.6).

6.3.2 Photometric Sensor Model

We now introduce a model relating indoor Manhattan scenes to observed image features. We begin with the single–view scenario in which we observe a feature $\boldsymbol{\phi} \in \mathbb{R}^n$ at each pixel $\boldsymbol{p}$.

We assume the graphical model shown in Figure 6.2. The generative process begins by sam-

pling a scene M, then samples pixels $\boldsymbol{p}$ and computes their orientation $a \in \{1, 2, 3\}$ (*c.f.* Algorithm 4.2), which is deterministic given M and is included in the graphical model for notational convenience only. Finally a feature $\boldsymbol{\phi}$ is sampled from a distribution that is conditionally independent of M given a. In practice we use the following features: three RGB colour components, three HSV colour components, two binary line sweep features described by Lee *et al.* [43], and twelve Gabor responses (three scales, four orientations). In Chapter 7 we drop the Gabor responses for efficiency reasons.

We assume a exponential–family likelihood for pixel features,

$$P(\boldsymbol{\phi} \mid a) \propto \exp(\boldsymbol{\omega}_a \cdot \boldsymbol{\phi}) \,. \tag{6.11}$$

Denoting the set of all observed pixel features Φ, pixels $\boldsymbol{P}$, and orientations A, the joint distribution is

$$P(\Phi, \boldsymbol{P}, A, M, \boldsymbol{\lambda}, \boldsymbol{\omega}) = P(M \mid \boldsymbol{\lambda}) \prod P(\boldsymbol{p}_i) P(a_i \mid M, \boldsymbol{p}_i) P(\boldsymbol{\phi}_i \mid a_i, \boldsymbol{\omega}) \,. \tag{6.12}$$

We do not model the distribution $P(\boldsymbol{p}_i)$ and for the remainder of this section it may be assumed that all probabilities are conditioned on this quantity.

We now derive MAP inference. The likelihood for M is

$$P(\Phi \mid M) \propto \int \prod_i P(\boldsymbol{\phi}_i \mid a_i) P(a_i \mid M) \mathrm{d}A \,. \tag{6.13}$$

In the integration over the latent variables, the only non–zero term is the one for which all a_i are equal to that predicted by Algorithm 4.2. Therefore, denoting by a_i^* the orientation output by Algorithm 4.2 for pixel $\boldsymbol{p}_i$ under M we have

$$P(\Phi \mid M) \propto \prod_i P(\boldsymbol{\phi}_i \mid a_i^*) \,. \tag{6.14}$$

Taking logarithms gives

$$\log P(\Phi \mid M) = \sum_i \log P(\boldsymbol{\phi}_i \mid a_i^*) + c \tag{6.15}$$

where c corresponds to the constant of proportionality in (6.14), which we henceforth drop since it makes no difference to the optimisation to come.

At this point we use the crucial observation of Section 4.5.4 that the orientation a_i^* is functionally dependent only on the pair (s_j, o_j) for the column j containing $\boldsymbol{p}_i$. Let $\bar{a}(x, y; s_j, o_j)$ be the orientation output by Algorithm 4.2 for pixel (x, y) under the hypothesis (s_j, o_j). We define

$$\pi_{\mathsf{mono}}(x, y, o) = \sum_{r=0}^{H} \log P(\boldsymbol{\phi}_{xr} \mid \bar{a}(x, r; y, o)\ ) \tag{6.16}$$

where the double–subscript in $\boldsymbol{\phi}_{xr}$ is a result of separately indexing rows and columns in (6.16).

Now consider the scene payoff,

$$\begin{aligned} \Pi(M) &= \sum_{j=0}^{W} \pi_{\mathsf{mono}}(j, s_j, o_j) && (6.17)\\ &= \sum_{j=0}^{W} \sum_{r=0}^{H} \log P(\boldsymbol{\phi}_{jr} \mid \bar{a}(j, r; s_j, o_j)\ ) && (6.18)\\ &= \log P(\Phi \mid M) + O(1)\ . && (6.19) \end{aligned}$$

This is simply the log–likelihood (6.15) up to a constant, so maximising (6.19) is equivalent to maximising (6.15). In this sense we have placed our model in the payoff formulation outlined in the previous section since by substituting the particular payoff function π_{mono} into (6.6) we obtain an optimisation problem in payoff formulation that is equivalent to maximum–likelihood inference under the graphical model of Figure 6.2. (Later we will show that this result extends easily to MAP inference also.)

6.3.3 Multiple–View Sensor Model

We now formulate the payoff function π_{stereo} for the case that multiple views of the scene are available. We assume that one image is identified as the base view I_0; the remaining K images are denoted $I_1, \ldots, I_K$. All images have size $W \times H$. We assume that all cameras are calibrated

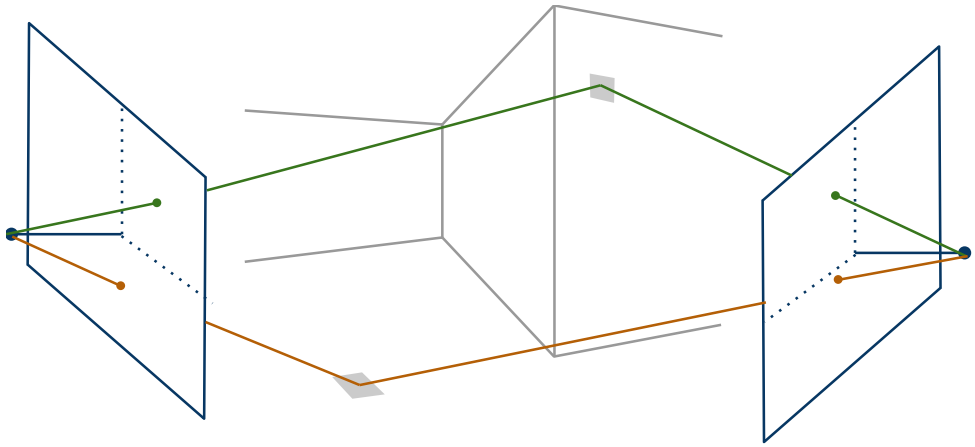

Figure 6.3: Pixel correspondences across multiple views are computed by back–projection onto the model M followed by re–projection into auxiliary views.

with the action of the i^{th} camera on a 3D point X being

$$K_i(R_i X + \boldsymbol{t}_i) \; . \tag{6.20}$$

Intuitively, we treat inference in this settings as follows. We consider models M in terms of their projection into I_0. We explained in Section 7.3 that models parametrised in image coordinates specify unique 3D models. Any model hypothesised in I_0 can therefore be re–projected into the auxiliary views, giving pixel–wise correspondences between frames (*c.f.* Figure 6.3). From this we compute a photo–consistency measure $\mathrm{PC}(\cdot)$, which provides the likelihood $P(I_0, \ldots, I_M \mid M)$.

Optimising over photo–consistency has been standard in the stereo literature for several decades [59]; our contribution is to show that (i) in the particular case of indoor Manhattan models, photo–consistency can be expressed as a payoff matrix; (ii) that we can therefore perform efficient and exact global optimisation; and (iii) that this fits naturally within a Bayesian framework alongside monocular and 3D features. Our approach also bears some similarity to Cornells *et al.* [10], who reconstruct building facades from a moving vehicle by analysing a related cost function derived from stereo pairs. Like us, they employ dynamic programing, although they do not constrain the arrangement of the vertical facades.

In Section 4.5.2 we showed how to convert a scene in vertex representation to a 3D reconstruc-

tion. Since all cameras are calibrated we can use this reconstruction to re–project any pixel $\boldsymbol{p}$ from the base view into all auxiliary views, as illustrated in Figure 6.3. Let $\boldsymbol{q}_k(\boldsymbol{p}; M)$ be the re–projection of $\boldsymbol{p}$ into view k via the scene hypothesis M. Let each pixel $\boldsymbol{p}_i$ in the base image be associated with a feature vector $\boldsymbol{\phi}_i \in \mathbb{R}^n$ and let each pixel $\boldsymbol{q}_{ki}$ in the k^{th} auxiliary view be similarly associated with a feature $\boldsymbol{\theta}_{ki} \in \mathbb{R}^n$. Let Φ be the set of all features in the base view and let Θ_k be the set of all features in the k^{th} auxiliary view. Finally, let

$$\bar{\boldsymbol{\theta}}_k(\boldsymbol{p}_i; M) = \boldsymbol{\theta}(\boldsymbol{q}_k(\boldsymbol{p}_i; M)) \tag{6.21}$$

be the feature associated with the reprojection of $\boldsymbol{p}_i$ into the k^{th} auxiliary view under the scene hypothesis M. Then the likelihood for M under our model is

$$P(\Phi, \Theta_1, \ldots, \Theta_K \mid M) = \prod_i \prod_{k=0}^{K} P(\boldsymbol{\phi}_i, \bar{\boldsymbol{\theta}}_k(\boldsymbol{p}_i; M) \mid \Sigma)\ . \tag{6.22}$$

and following the standard approach [59], the feature likelihood is a zero–mean Gaussian:

$$P(\boldsymbol{\phi}_i, \bar{\boldsymbol{\theta}}_k(\boldsymbol{p}_i; M) \mid \Sigma) = \mathcal{N}(\boldsymbol{\phi}_i - \bar{\boldsymbol{\theta}}_k(\boldsymbol{p}_i; M); \Sigma) \tag{6.23}$$

Taking logarithms we recognise a simple sum over pixel–wise photo–consistency terms,

$$\log P(\Phi, \Theta_1, \ldots, \Theta_K \mid M) = \sum_i \sum_{k=0}^{K} \|\boldsymbol{\phi}_i - \bar{\boldsymbol{\theta}}_k(\boldsymbol{p}_i; M)\|_\Sigma + c \tag{6.24}$$

We now write equation (6.24) in payoff form. To this end we leverage the observation made in Section 4.5.4 that the depth of a pixel $\boldsymbol{p}$ under a scene hypothesis M is functionally dependent only on the pair (s_j, o_j) for the column j containing $\boldsymbol{p}$. Let $\bar{d}(\boldsymbol{p}; s_j)$ be the depth of $\boldsymbol{p}$ under the hypothesis s_j, as output by Algorithm 4.3.

Furthermore, re–projecting a pixel into an auxiliary view requires only the depth at that pixel. Therefore we can identify all correspondences for any pixel $\boldsymbol{p}$ from the value s_j alone. Specifi-

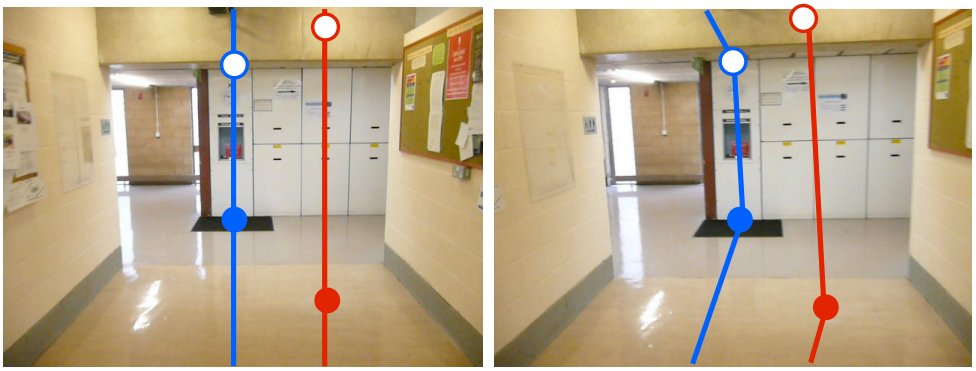

Figure 6.4: Two hypotheses for the location of the seam and the reprojections they imply for each image column in an auxiliary image. The blue dot happens to be a correct hypothesis (unbeknown to the system), while the red dot is incorrect. As a result, the blue line corresponds to the same set of 3D locations in both images but the red line does not.

cally, the re–projection of $\boldsymbol{p}$ into the k^{th} view under the hypothesis s_j is

$$\boldsymbol{q}_k(\boldsymbol{p}; s_j) = K_k(R_k X_i + \boldsymbol{t}_k) \tag{6.25}$$

where

$$X_i = R_0^{-1}\left(\bar{d}(\boldsymbol{p}; s_j) K_0^{-1}\boldsymbol{p} - \boldsymbol{t}_0\right) . \tag{6.26}$$

We can now re–write the correspondence function $\bar{\boldsymbol{\theta}}_{ki}$ in terms of s_j alone,

$$\bar{\boldsymbol{\theta}}_k(\boldsymbol{p}; s_j) = \boldsymbol{\theta}(\boldsymbol{q}_k(\boldsymbol{p}; s_j)) . \tag{6.27}$$

Finally, the payoff function is

$$\pi_{\text{stereo}}(x, y) = \sum_{r=0}^{H}\sum_{k=1}^{K} \|\boldsymbol{\phi}_{xr} - \bar{\boldsymbol{\theta}}_k([x, r]^T; y)\|_\Sigma \tag{6.28}$$

where as in (6.16) we have switched to a separate indexing scheme for rows and columns, so $\boldsymbol{\phi}_{xy}$ is the feature for the pixel at (x, y) and $\bar{\boldsymbol{\theta}}_k(x, r; y)$ the the feature for the reprojection of (x, r)

into the k^{th} view under the hypothesis $s_j = y$. Substituting (6.28) into (6.1),

$$\begin{aligned}
\Pi(M) &= \sum_{j=0}^{W} \pi_{\mathsf{stereo}}(j, s_j) && (6.29)\\
&= \sum_{j=0}^{W}\sum_{r=0}^{H}\sum_{k=1}^{K} \|\boldsymbol{\phi}_{jr} - \bar{\boldsymbol{\theta}}_k([j,r]^T; s_j)\|_\Sigma && (6.30)\\
&= \log P(\Phi, \Theta_1, \ldots, \Theta_K \mid M) - c && (6.31)
\end{aligned}$$

The completes the reduction of the stereo sensor model to payoff form, since we have shown that maximising the likelihood (6.22) is equivalent to the payoff optimisation problem (6.6) for a particular instantiation of the payoff function π.

A Different View

Our approach could also be cast as solving the general stereo problem in terms of disparity maps, where in place of priors based on pixel–wise smoothness constraints, our prior is (6.7) for those disparity maps that correspond to valid indoor Manhattan reconstructions, and zero for others. Inference under this model would be intractable if cast directly in terms of disparity maps because determining whether a given disparity map corresponds to some indoor Manhattan reconstruction is difficult. Nevertheless, our approach shows that by re–parametrising in the vertex representation the problem becomes tractable.

Note that the column–wise decomposition (6.28) neither commits us to optimising over columns independently, nor to ignoring interactions between columns. By inspecting (6.22) one sees immediately that our model assumes no independence between image columns (only conditional independence given M), and indeed correlations do come into effect when we optimise over the full payoff matrix later in this chapter. Our results will show that widely separated image regions often interact strongly. The derivations in this section follow deductively from the indoor Manhattan assumption; the only approximation is that concerning occlusions, which we discuss below.

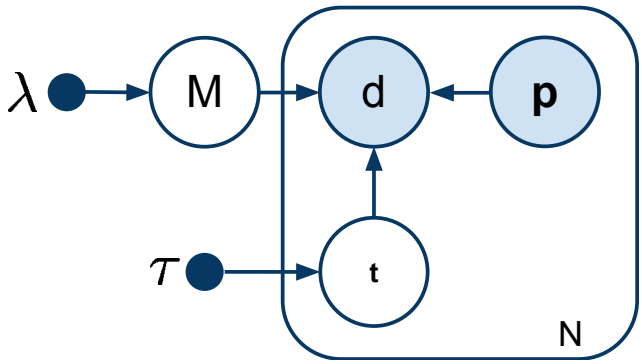

Figure 6.5: The graphical model relating indoor Manhattan models to 3D points. The hidden variable t indicates whether the point is inside, outside, or coincident with the model.

Occlusions

We have ignored self–occlusions in (6.22). For short baselines, such as frames sampled over a few seconds from a moving camera, this is unproblematic since indoor environments tend to be mostly convex from any single point of view. Even in highly non–convex environments our system achieves excellent results by integrating 3D and monocular features, and enforcing strong global consistency, as will be shown in our experimental section. Further discussion of this issue is in the final section of this chapter.

6.3.4 Point Cloud Sensor Model

In this section we explore the context in which a 3D point cloud is available during inference. The point clouds generated by structure–from–motion systems are typically too sparse for direct reconstruction, but can provide useful cues alongside monocular and stereo data.

Our graphical model for 3D data is depicted in Figure 6.5. The model M is sampled according to the prior (6.7), then depth measurements d_i are generated for pixels $\boldsymbol{p}_i$. Many such measurements will correspond to clutter or measurement errors, rather than to the walls represented by M. Our model captures this uncertainty explicitly through the latent variable t_i, which has the following interpretation. If $t_i = \mathsf{ON}$ then d_i corresponds to some surface represented explicitly in M. Otherwise, either $t_i = \mathsf{IN}$, meaning some clutter object within the room was measured, or $t_i = \mathsf{OUT}$, in which case an object outside the room was measured, such as through a window.

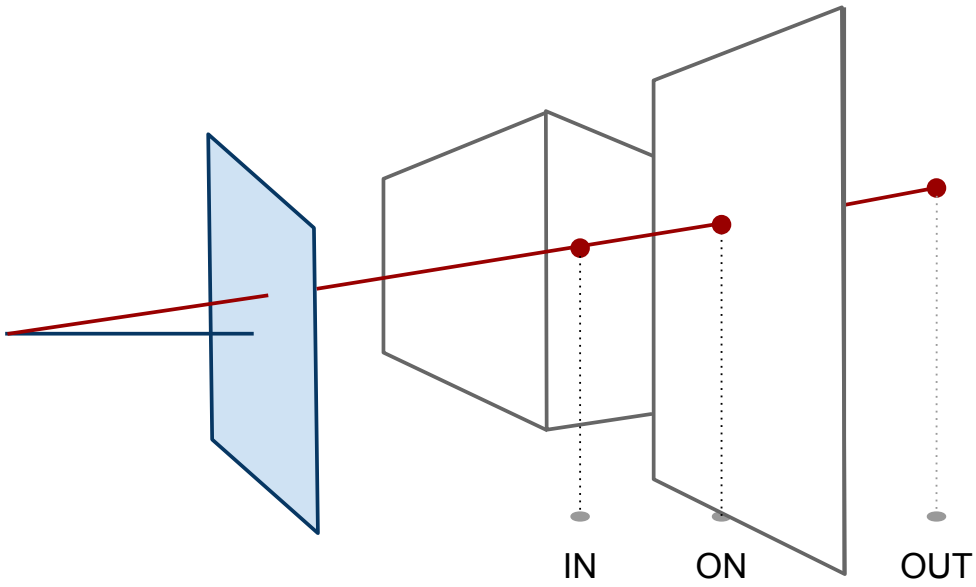

Figure 6.6: Depth measurements d_i might be generated by a surface in our model (represented by $t_i = \mathsf{ON}$) or by an object inside or outside the environment (in which case $t_i = \mathsf{IN}, \mathsf{OUT}$ respectively).

The likelihoods we use are

$$P(d \mid \boldsymbol{p}, t = \mathsf{IN}, M) = \begin{cases} \alpha, & \text{if } 0 < d < \bar{d}(\boldsymbol{p}; M) \\ 0, & \text{otherwise} \end{cases} \tag{6.32}$$

$$P(d \mid \boldsymbol{p}, t = \mathsf{OUT}, M) = \begin{cases} \beta, & \text{if } \bar{d}(\boldsymbol{p}; M) < d < d_{\text{max}} \\ 0, & \text{otherwise} \end{cases} \tag{6.33}$$

$$P(d \mid \boldsymbol{p}, t = \mathsf{ON}, M) = \mathcal{N}(d\,;\, \bar{d}(\boldsymbol{p}; M), \sigma)\,. \tag{6.34}$$

where α and β are determined by the requirement that the probabilities sum to 1 and $\bar{d}(\boldsymbol{p}; M)$ denotes the depth predicted by M at $\boldsymbol{p}$. We compute likelihoods on d by marginalising over t,

$$P(d \mid \boldsymbol{p}, M, \boldsymbol{\tau}) = \sum_t P(d \mid \boldsymbol{p}, M, t) P(t \mid \boldsymbol{\tau})\,. \tag{6.35}$$

where $P(t \mid \boldsymbol{\tau})$ is a categorical distribution with parameters τ_{IN}, τ_{OUT}, and τ_{ON}. Equation (6.35) can be readily evaluated for any d and $\boldsymbol{p}$ since the sum is over just the three possible values for

t. Denoting the set of all depth measurements D, the full likelihood for M is

$$P(D \mid \boldsymbol{P}, M) = \prod_i P(d_i \mid \boldsymbol{p}_i, M) \tag{6.36}$$

$$\log P(D \mid \boldsymbol{P}, M) = \sum_i \log P(d_i \mid \boldsymbol{p}_i, M) \tag{6.37}$$

We now utilise the same observation as we did in the previous section, namely that the depth at $\boldsymbol{p}$ is functionally dependent only on the seam pair in the column containing $\boldsymbol{p}$. Retaining the notation under which $\bar{d}(\boldsymbol{p}; s_j)$ is the depth at $\boldsymbol{p}$ computed by Algorithm 4.3 for M, we define the payoff function

$$\pi_{\mathsf{3D}}(x, y) = \sum_{i \in D_x} \log P(d_i \mid \boldsymbol{p}_i, \bar{d}(\boldsymbol{p}_i; y)) \tag{6.38}$$

where D_x contains indices for all depth measurements in column x. We verify that (6.38) does in fact correspond to the log–likelihood (6.36) by substituting the above into (6.1), giving

$$\Pi(M) = \sum_{j=0}^{W} \pi_{\mathsf{3D}}(j, s_j) \tag{6.39}$$

$$= \sum_{j=0}^{W} \sum_{i \in D_j} \log P(d_i \mid \boldsymbol{p}_i, \bar{d}(\boldsymbol{p}_i; s_j)\ ) \tag{6.40}$$

$$= \log P(D \mid \boldsymbol{P}, M)\ . \tag{6.41}$$

6.3.5 Joint Model

We combine photometric, stereo, and 3D data into a joint model by assuming conditional independence given M,

$$P(X_{\mathsf{mono}}, X_{\mathsf{stereo}}, X_{\mathsf{3D}} \mid M) = P(X_{\mathsf{mono}} \mid M) P(X_{\mathsf{stereo}} \mid M) P(X_{\mathsf{3D}} \mid M)\ . \tag{6.42}$$

Taking logarithms leads to summation over payoffs,

$$\log P(X_{\mathsf{mono}}, X_{\mathsf{stereo}}, X_{\mathsf{3D}} \mid M) = \Pi_{\mathsf{joint}}(M) \tag{6.43}$$

where

$$\pi_{\mathsf{joint}}(\boldsymbol{p}) = \pi_{\mathsf{mono}}(\boldsymbol{p}) + \pi_{\mathsf{stereo}}(\boldsymbol{p}) + \pi_{\mathsf{3D}}(\boldsymbol{p}) \,. \tag{6.44}$$

Finally, the log posterior is

$$\begin{aligned} \log P(M \mid X_{\mathsf{mono}}, X_{\mathsf{stereo}}, X_{\mathsf{3D}}) &\propto \log P(X_{\mathsf{mono}} \mid M) + \log P(X_{\mathsf{stereo}} \mid M) \\ &\quad + \log P(X_{\mathsf{3D}} \mid M) + \log P(M) \\ &\propto \Pi_{\mathsf{joint}}(M) - \Gamma(M) \,. \end{aligned} \tag{6.45}$$

The relation above is a proportionality rather than an equality because we have omitted the evidence $P(X)$. For the purpose of maximisation this term is irrelevant since it is independent of the quantity that we are maximising. We can now cast maximum–likelihood and maximum–aposteriori inference in the form (6.4),

$$M^*_{\mathtt{ML}} = \operatorname*{argmax}_{M \in \mathcal{M}} \Pi_{\mathsf{joint}}(M) \tag{6.46}$$

$$M^*_{\mathtt{MAP}} = \operatorname*{argmax}_{M \in \mathcal{M}} \Pi_{\mathsf{joint}}(M) - \Gamma(M) \,. \tag{6.47}$$

This completes the task of writing inference for our model in payoff form. In particular, the above derivations show that for any set of observations (photometric, stereo, depth, or any combination thereof), there is a particular payoff function Π and penalty function Γ such that solving (6.6) is equivalent to solving MAP (or ML) inference under our model. In practice we only need to evaluate Π at integer pixel coordinates, so we represent it as a 2D array. The remainder of this chapter focuses on solving optimisation problems of the form (6.6).

6.4 MAP Inference Using Dynamic Programming

In this section we solve the optimisation problem (6.6). That is, given some π and γ, we wish to identify the maximiser M^* of

$$f(M) = \sum_{j=1}^{W} \pi(j, s_j, o_j) - \sum_{i=0}^{K-1} \gamma(i; M) \,, \tag{6.48}$$

where

$$M = (x_1, y_1, o_1,\ x_2, y_2, o_2,\ \ldots,\ x_{n-1}, y_{n-1}, o_{n-1},\ x_n) \tag{6.49}$$

is an indoor Manhattan scene in vertex representation.

We assume that the scene rotation R_w as well as the Manhattan homology H_a have been recovered as discussed in previous chapters. We further assume that all images are rectified as in (4.15). The algorithms presented in this section are valid without the rectification step, but assuming rectification considerably simplifies their presentation. Our solution uses dynamic programming to efficiently solve the maximisation (6.6). We develop the algorithm conceptually before formalising it.

In the optimisation (6.6), we wish to constrain solutions to valid indoor Manhattan scenes. In terms of individual pixel labels, such a constraint introduces complicated dependencies between large groups of pixels, since assigning a particular label to any one pixel restricts which labels can be assigned to other pixels in the same column. We therefore cast the optimisation directly in terms of the vertex representation introduced in Chapter 4.

We present our solution by first describing a simple but inefficient version, followed by three refinements that lead to an $O(N)$ algorithm (where N is the number of pixels). At each stage we describe our algorithm conceptually before formalising it.

6.4.1 Basic Algorithm

We have already seen that every indoor Manhattan scene can be represented as a left–to–right sequence of wall segments. Our approach is based on the construction of a graph over all possible indoor Manhattan scenes. This nodes in this graph represent pixels and the edges represent vanishing lines. Each path in this graph corresponds to a different indoor Manhattan scene, and by assigning certain weights to the edges we reduce the optimisation problem (6.6) to a graph search problem, which we solve using dynamic programming. The graph is depicted informally in Figure 6.8. In dynamic programming parlance, nodes are called states and the adjacency matrix is called the feasible set. We now describe the construction of this graph.

State space. Our state space contains two states for each pixel. Each state corresponds to a sub–problem of the form, *"What is the optimal indoor Manhattan scenes spanning the part of the image to the left of pixel $\boldsymbol{p}$?"*. There is one state for each pixel and each for of the two vertical orientations, giving the $2N$ state space. We write states as pairs, as in $\boldsymbol{s} = (\boldsymbol{p}, o)$.

Feasible set. The feasible set describes the connections between states. There is a separate feasible set $\mathcal{F}(\boldsymbol{s})$ for each state and $\boldsymbol{t} \in \mathcal{F}(\boldsymbol{s})$ if and only if there is an edge from $\boldsymbol{s}$ to $\boldsymbol{t}$. In our first algorithm the feasible set for a state $\boldsymbol{s} = (\boldsymbol{p}, o)$ consists of all pixels to the left of $\boldsymbol{p}$ that fall on the vanishing line connecting $\boldsymbol{p}$ and $\boldsymbol{v}_o$, as depicted in Figure 6.8. This leads to a search graph in which each path corresponds to an indoor Manhattan scene, as shown in Figure 6.7.

Value function. The value function describes the quantity being optimised at each state. Our value function maps *paths through the graph* to real numbers. That is, the domain of our value function is the set of paths from any pixel $\boldsymbol{p}$ to the left edge of the image. We define the value of such a path to be the sum of the entries in the payoff matrix along the path minus the penalty for the corners along the path, *i.e.*

$$f(M) = \sum \pi(j, s_j, o_j) - \sum_{i=0}^{|M|} \gamma(i; M) \; . \tag{6.50}$$

Figure 6.9 shows one such path and the elements of the payoff matrix that are summed to

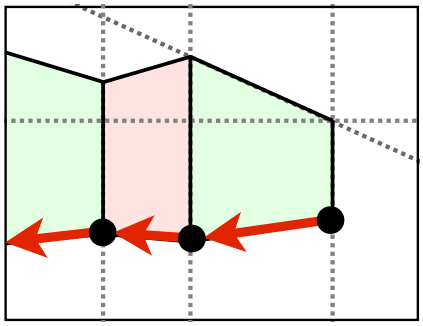

Figure 6.7: A path through the search graph and the indoor Manhattan scene that it corresponds to. The black dots are states, the red arrows are edges, and the rest is for illustration only.

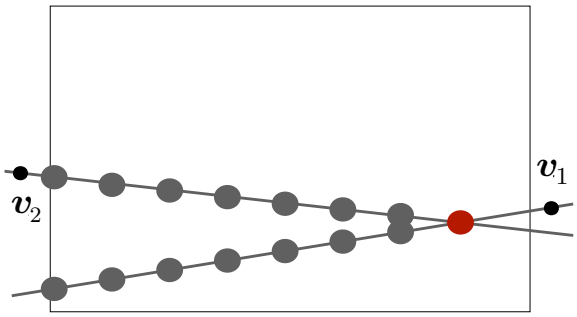

Figure 6.8: The search graph corresponding to the first version of our dynamic programming algorithm. This figure identifies one node (red circle) and shows all neighbours to which it is connected via outgoing edges (grey circle).

compute its value. The motivation for choosing this particular value function is that for pixels on the right edge of the image it is equal to the full objective function (6.6).

Optimisation step. We now show how to maximise the value function at each state. This is best explained by considering a single state s and assuming that we already know the solutions for all preceding states — that is, for each state t to the left of s, let us assume that we already

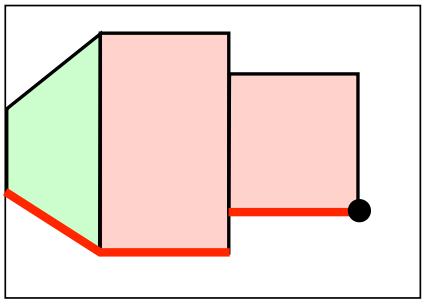

Figure 6.9: A path from the left edge of the image to a particular state s. The value of this path is the sum of all entries in the payoff matrix along the path highlighted in red.

know the optimal[2] path from $\boldsymbol{t}$ to the left edge of the image, and also the value of that path. We denote this quantity

$$V(\boldsymbol{t}) = \operatorname{argmax} f(M) \tag{6.51}$$

where the maximisation is over paths terminating at $\boldsymbol{t}$. Our task is to use the known solutions to the preceding states to discover the optimal path for the state $\boldsymbol{s}$ under consideration. We accomplish this as follows.

1. Enumerate all states $\boldsymbol{t}$ that are connected to $\boldsymbol{s}$; *i.e.* all $\boldsymbol{t} \in \mathcal{F}(\boldsymbol{s})$.

2. For each, compute

$$V(\boldsymbol{t}) + \Delta(\boldsymbol{t}, \boldsymbol{s}) \,, \tag{6.52}$$

   where

$$\Delta(\boldsymbol{t}, \boldsymbol{s}) = \sum \pi(x_i, y_i, o_i) - \gamma \tag{6.53}$$

   is the sum of payoffs along the line segment between $\boldsymbol{t}$ and $\boldsymbol{s}$, and λ is the penalty associated with the new corner at $\boldsymbol{t}$ (see Figure 6.10). Δ can be thought of as the marginal value for the wall segment added between $\boldsymbol{t}$ and $\boldsymbol{s}$.

3. Set $V(\boldsymbol{s})$ to the maximum over the terms computed in step 2. We summarise this in the following recurrence relation.

$$V(\boldsymbol{s}) = \max_{\boldsymbol{t} \in \mathcal{F}(\boldsymbol{s})} V(\boldsymbol{t}) + \Delta(\boldsymbol{t}, \boldsymbol{s}) \tag{6.54}$$

Full algorithm. We are now ready to describe our first algorithm that solves the optimisation problem (6.6). The basic idea is to recursively apply the procedure above to compute the value $V(\boldsymbol{s})$ for all states. We start at the pixels on the right edge of the image and begin executing the procedure above. During step 2 we will encounter some states $\boldsymbol{t}$ for which we do not know the value of $V(\boldsymbol{t})$. At this point we recursively apply the procedure to that state, and so on each time we need to evaluate $V(\boldsymbol{t})$ for any state not yet encountered. The recursion terminates when we encounter a pixel on the left edge of the image since for these states $V(\boldsymbol{s})$ is always

[2]Optimality here means the path that maximises the value function described above.

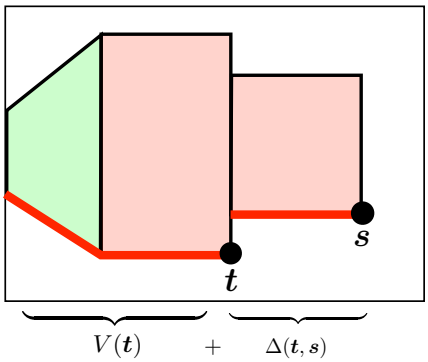

Figure 6.10: The computation of the value function at $\boldsymbol{s}$. This figure shows just one term in the maximisation (6.52); computing $V(\boldsymbol{s})$ involves maximisation over all possible states $\boldsymbol{t}$.

zero. There are no circular dependencies because our search graph is acyclic by construction. Each time we complete the computation of some $V(\boldsymbol{t})$, we cache the result in a lookup table for re–use next time the same state is encountered [3]. After applying this procedure recursively we will have computed the the value of the optimal path for every state. The final solution to our optimisation problem is obtained by identifying the largest value among all states on the right edge of the image. Back–tracking allows us to recover the optimal path through the graph, which is precisely the vertex representation for the indoor Manhattan scene maximising (6.6). We formalise and prove the correctness of this algorithm in a section below.

Complexity. Analysing the complexity of dynamic programming algorithms is trivial because computation is bounded by the product of (1) the number of states and (2) the amount of computation per state[4]. For an image of size $L \times L$ the algorithm described above consists of $2L^2$ states and each state involves a maximisation over $O(L)$ preceding states. Each term in the maximisation costs $O(L)$ to compute, giving an overall complexity of $O(L^4)$.

Limitations. The algorithm described thus far does not consider occluding corners, so if the true indoor Manhattan scene contains occluding corners, this algorithm will not find it. We rectify this in the following section.

[3] Far from being a minor optimisation, the caching of intermediate results makes the difference between an exponential and polynomial–time algorithm.

[4] excluding computation associated with recursive evaluations of V to avoid double–counting

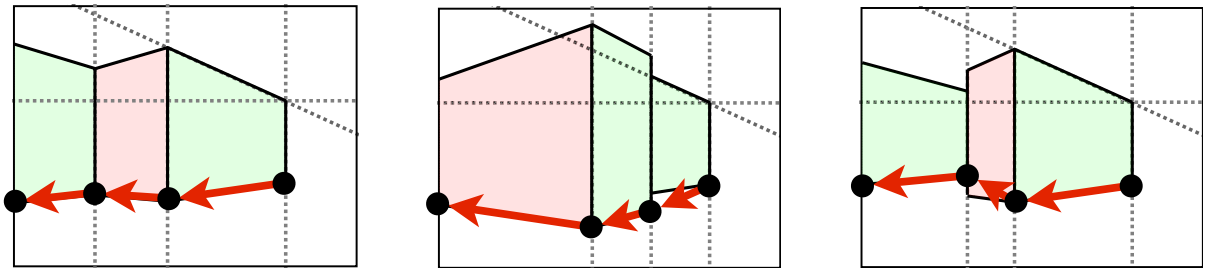

Figure 6.11: Three paths through the search graph after making the changes described in Section 6.4.2 to permit occluding corners. The two right–most scenes cannot be represented in the previous search graph. Note that there is a state at the bottom–right of each wall segment.

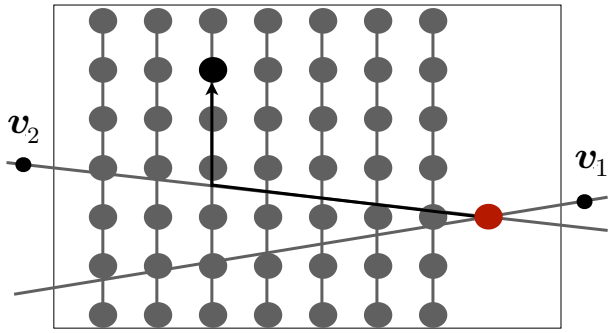

Figure 6.12: The search graph corresponding to the second version of our dynamic programming algorithm (Section 6.4.2). Here we have highlighted a single node (red circle), which has outgoing edges to every pixel to its left (grey circles). One neighbouring state (black dot) is singled out to show that the edges between states represents displacement along a vanishing direction followed by displacement in the vertical direction.

6.4.2 First Refinement: Occluding Corners

In order to account for occluding corners we need to amend both the feasible set and the optimisation step from Section 6.4.1.

Feasible set. The feasible $\mathcal{F}(\boldsymbol{s})$ set described in the previous section consisted of the set of states along the vanishing line associated with $\boldsymbol{s}$. Here we revise the feasible set to include *all* states to the left of $\boldsymbol{s}$, where for states $\boldsymbol{t}$ not on the vanishing line, stepping from $\boldsymbol{s}$ to $\boldsymbol{t}$ corresponds to moving first along the vanishing and then vertically up or down to $\boldsymbol{t}$, as shown in Figure 6.12 and Figure 6.11.

Optimisation step. Our optimisation step remains very similar to that described in Section 6.4.1. For each state $\boldsymbol{s}$ we consider all preceding states $\boldsymbol{t}$. We add the value for $\boldsymbol{t}$ to the value

associated with the edge between $\boldsymbol{t}$ and $\boldsymbol{s}$, which is now computed by summing entries from the payoff matrix along the vanishing line from $\boldsymbol{s}$ to the column containing $\boldsymbol{t}$.

The introduction of occluding corners means that our algorithm can now generate configurations that are physically impossible. We detect and exclude such configurations by checking each state in the feasible set against the rules described by Lee *et al.* [43], and, if violated, excluding that state from the feasible set. The revised optimisation routine is therefore:

1. Enumerate all states $\boldsymbol{t}$ in the feasible set for $\boldsymbol{s}$.
2. For each $\boldsymbol{t}$, check whether connecting $\boldsymbol{s}$ to $\boldsymbol{t}$ would yield a physically unrealisable configuration.
3. If not, compute
$$V(\boldsymbol{t}) + \Delta(\boldsymbol{t}, \boldsymbol{s}) \,, \tag{6.55}$$
where Δ is the sum over the payoff function along the vanishing line from $\boldsymbol{s}$ to the column containing $\boldsymbol{t}$ minus the penalty associated with the new corner at $\boldsymbol{t}$ (see Figure 6.12).
4. Set $V(\boldsymbol{s})$ to the maximum value computed in step 3.

Algorithmic complexity. The only change introduced in this section that is relevant to computational complexity is the expansion of the feasible set by a factor of $O(L)$, meaning that the maximisation in step 4 is now over $O(L^2)$ terms. The physical realisability conditions can be evaluated in constant time so do not affect computational complexity. This brings the computation complexity of the revised algorithm to $O(L^5)$.

6.4.3 Correctness of Section 6.4.2

We now pause to prove the correctness of the algorithm presented thus far. All dynamic programming algorithms are associated with an optimal substructure property of the underlying optimisation problem. Here we prove the optimal substructure property corresponding to the inference of indoor Manhattan scenes.

Preliminaries

We begin by formalising several concepts introduced in the preceding sections. What we have heretofore called a "path from the left edge of the image to $\boldsymbol{s}$" will henceforth be called a *partial scene*. In vertex representation, a partial scene is identical to an ordinary scene except that the last x–coordinate might be smaller than the image width. Partial scenes have a seam representation mirroring that for full scenes.

The *truncation* of the partial scene M is obtained by removing the right–most wall from M, for which we will write M_{-1}. The *concatenation* of M with the wall (x_a, y, o, x_b) is defined if and only if M terminates at column x_a and equals

$$M +\!\!+ W = (x_1, y_1, o_1, \ldots,\ x_{n-1}, y_{n-1}, o_{n-1},\ x_a, y, o,\ x_b) \tag{6.56}$$

We will also refer to the *terminating state* of a scene, which is the state for the lower–right corner of the rightmost wall (the black dot in Figure 6.9, for example).

The correctness of our algorithm depends in part on the structure of the physical realisability constraints described by Lee *et al.* [43]. We do not wish to repeat their work here, but for completeness we re–state some properties of the conditions they derived.

Lemma 1. *The realisability of the i^{th} corner of the scene M is a function of the four values:*

$$y,\ o_i,\ x_{i+1},\ y_{i+1},\ o_{i+1} \tag{6.57}$$

where the i^{th} wall in M terminates at (x_{i+1}, y, o_i).

Proof. See [43] □

Lemma 2. *M is realisable if and only if all corners in M are realisable.*

Proof. See [43] □

Lemma 3. *Let M be a realisable scene. Then its truncation M_{-1} is realisable.*

Proof. The truncation M_{-1} consists of a subset of the corners in M, all of which are realisable by assumption. □

Lemma 4. *Let $W = (x_b, y_b, o_b, x_c)$ be a wall and let M and Q be feasible scenes terminating at (x_b, y_a, o_a). Then $M +\!\!+ W$ is realisable if and only if $Q +\!\!+ W$ is realisable.*

Proof. Suppose $M +\!\!+ W$ is realisable. Then we need to show that each corner in $Q +\!\!+ W$ is realisable. By assumption the first $|Q|$ corners are realisable. According to Definition 1, the feasibility of the last corner is a function of the values

$$y_a,\ o_a,\ x_b,\ y_b,\ o_b, \tag{6.58}$$

But these values are identical to the last corner in $M +\!\!+ W$, which is realisable by assumption, so $Q +\!\!+ W$ is realisable. The other direction of implication is obtained by a symmetric argument.

□

Optimal Substructure

Proving that our algorithm solves the optimisation problem (6.6) hinges on an optimal substructure property of indoor Manhattan scenes. Roughly, this property states that if a particular hypothesis is optimal for a particular sub–problem, then its "predecessors" (truncations) are each optimal for their corresponding sub–problems. We formalise this below.

Definition 1. *Let the sub–problem* **Best** *be defined as follows.*

A scene M satisfies **Best**(x, y, o) *if M is realisable and M terminates at (x, y, o). A scene M solves the sub–problem* **Best**(x, y, o) *if it satisfies* **Best**(x, y, o) *and there is no other scene satisfying* **Best**(x, y, o) *that obtains a greater value.*

Figure 6.13 shows three scenes satisfying one sub–problem.

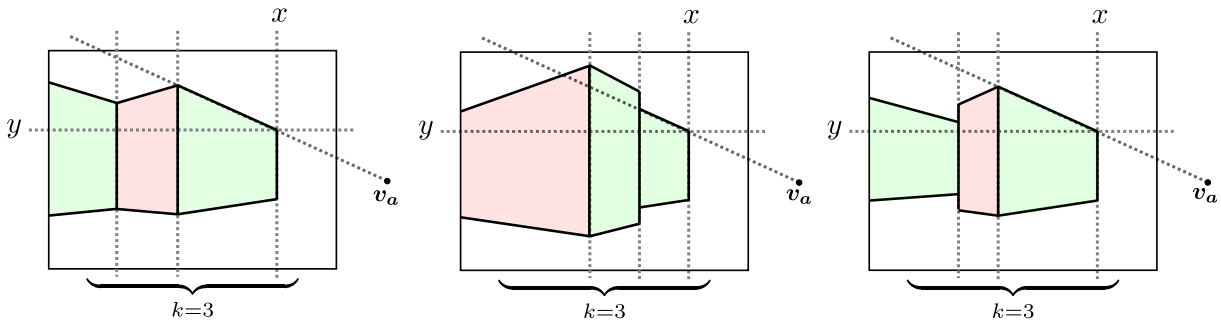

Figure 6.13: Three models satisfying the sub–problem $\mathsf{Best}(x, y, o)$.

We now turn to the optimal substructure theorem, which is the central theorem of this chapter. Figure 6.14 gives a graphical sketch of the proof.

Theorem 1. *Let M be a scene terminating at (x, y, o). Let M' be the 1–truncation of M and let (x', y', o') be the terminating state of M'. If M solves $\mathsf{Best}(x, y, o)$ then M' solves $\mathsf{Best}(x', y,' o')$.*

Proof. First note that M' satisfies $\mathsf{Best}(x', y', o')$ since it terminates at (x', y', o') and is realisable by Lemma 3.

We show that M' solves $\mathsf{Best}(x', y', o')$ by appeal to *reductio*. If M' does not solve $\mathsf{Best}(x', y', o')$ then there exists a scene Q' satisfying $\mathsf{Best}(x', y', o')$ such that

$$f(Q') > f(M') \,. \tag{6.59}$$

Let W be the right–most wall in M and let $Q = Q' +\!\!+ W$. We have that Q satisfies $\mathsf{Best}(x, y, o)$ because:

1. Q terminates at (x, y, o) since its right–most wall is W, which terminates at (x, y, o) by assumption.

2. Q is realisable by Lemma 4.

Next we use expand the values obtained by M and Q,

$$\begin{aligned} f(M) &= f(M') + \Delta(M', M) \\ f(Q) &= f(Q') + \Delta(Q', Q) \end{aligned} \tag{6.60}$$

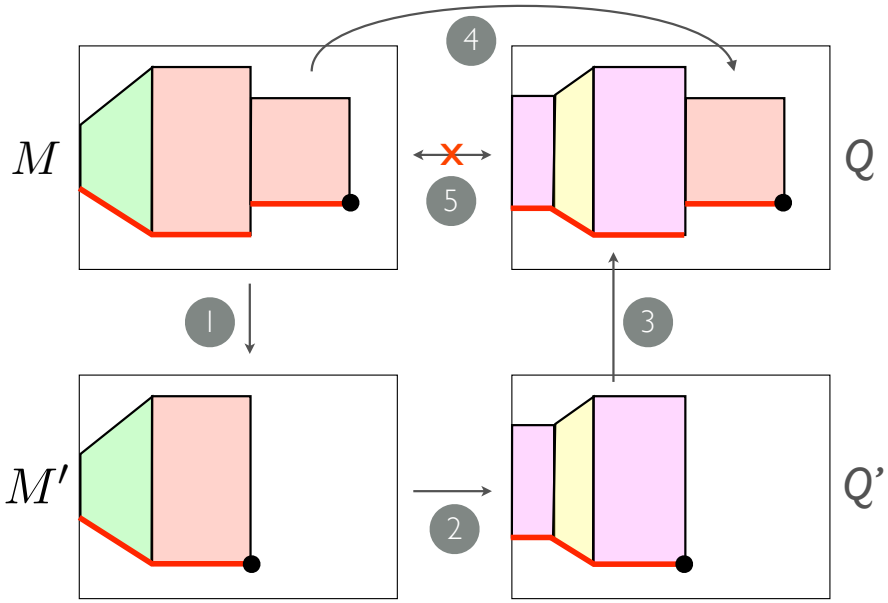

Figure 6.14: A graphical sketch of the proof of Theorem 1. The proof proceeds counter–clockwise from top left. First we let M be an optimal scene for some sub–problem, then (1) define M' to be its truncation. We then (2) postulate some Q' with value greater than M', and then from this we (3,4) construct Q. The contradiction follows by (5) comparing M and Q.

But by an analogous argument to the proof of Lemma 4, the corner produced by appending W to M' is the same as that produced by appending W to Q' since M' and Q' terminate at the same state. Therefore

$$\Delta(M', M) = \Delta(Q', Q) \; . \tag{6.61}$$

Combining (6.59), (6.60), and (6.61), we have

$$f(Q) > f(M) \; , \tag{6.62}$$

but this contradicts the assumption of M as a solution to $\mathsf{Best}(x, y, o)$. □

Algorithm 6.1 formalises the procedure that we described informally in Section 6.4.2.

6.4.4 Second Refinement: Auxiliary Sub–problems

The basic algorithm described thus far iterates over all pixels to the left of $\boldsymbol{s}$ for each state $\boldsymbol{s}$. In this section we show how to reduce this $O(L^2)$ operation to $O(L)$. Our approach is to expand

Algorithm 6.1 Solution to (6.6) [version 1]

Require: Π is a payoff function
Require: γ is a penalty function
Ensure: M^* is the solution to (6.6)
  $\texttt{cache} = \emptyset$
  $\texttt{source} = \emptyset$
  $f^* = -\infty$
  for $y = 1$ to H **do**
    for $o \in \{1, 2\}$ **do**
      $f_{cur} \leftarrow \text{Solve}(W, y, o)$
      if $f_{cur} > f^*$ **then**
        $f^* \leftarrow f_{cur}$
        $\boldsymbol{s}^* \leftarrow \{W, y, o\}$
      end if
    end for
  end for
  $M^* \leftarrow (W)$
  while $\boldsymbol{s}^* \neq \emptyset$ **do**
    $M^* \leftarrow (\boldsymbol{s}_x^*, \boldsymbol{s}_y^*, \boldsymbol{s}_o^*) +\!\!+ M^*$
    $\boldsymbol{s}^* \leftarrow \texttt{source}[\boldsymbol{s}^*]$
  end while

Subprocedure Solve:

Require: $\boldsymbol{s} = (x, y, o) \in \mathcal{S}$
Ensure: $\texttt{cache}[\boldsymbol{s}] = f_{in}(\boldsymbol{s})$
  if $\boldsymbol{s} \notin \texttt{cache}$ **then**
    if $x = 0$ **then**
      $\texttt{cache}[\boldsymbol{s}] \leftarrow 0$
      $\texttt{source}[\boldsymbol{s}] \leftarrow \emptyset$
    else
      for all $\boldsymbol{s}' \in \mathcal{F}(\boldsymbol{s})$ **do**
        $W \leftarrow (\boldsymbol{s}'_x, \boldsymbol{s}_y, \boldsymbol{s}_o, \boldsymbol{s}_y)$
        $f_{cur} \leftarrow \text{Solve}(\boldsymbol{s}') + \Pi(W) - \gamma(\boldsymbol{s}', W)$
        if $f_{cur} > \texttt{cache}[\boldsymbol{s}]$ **then**
          $\texttt{cache}[\boldsymbol{s}] \leftarrow f_{cur}$
          $\texttt{source}[\boldsymbol{s}] \leftarrow \boldsymbol{s}'$
        end if
      end for
    end if
  end if
  return $\texttt{cache}[\boldsymbol{s}]$

the state space in a way that allows us to reduce the number of connections between states. It will be shown that with only a constant factor increase in the number of states, we can decrease the size of the realisable set by a factor of $O(L)$, which leads to a corresponding speedup of the optimisation step. In the previous section we enforced physical realisability by explicitly testing each $\boldsymbol{t}$ and omitting any that lead to an impossible scene. In this section we show that by introducing auxiliary states we can deal with realisability constraints while avoiding the expensive optimisation over $O(L^2)$ terms.

State space. The new state space contains four states for each state in the old state space (Section 6.4.1), giving a total of 8 states per pixel. We identify the new states with the labels $(\texttt{IN}, \texttt{UP}, \texttt{DOWN}, \texttt{OUT})$, which are depicted in Figure 6.15 and have the following meanings:

- States of the form $(\boldsymbol{p}, o, \texttt{IN})$ correspond to the set of scenes that terminate at $\boldsymbol{p}$ with orientation o, just as in Section 6.4.1.
- States of the form $(\boldsymbol{p}, o, \texttt{UP})$ correspond to the set of scenes that terminate at or above $\boldsymbol{p}$ with orientation o.
- States of the form $(\boldsymbol{p}, o, \texttt{DOWN})$ correspond to the set of scenes that terminate at or below $\boldsymbol{p}$ with orientation o.
- States of the form $(\boldsymbol{p}, o, \texttt{OUT})$ correspond to the set of scenes such that appending a wall starting at $\boldsymbol{p}$ with orientation o would not contradict any physical realisability constraints.

Feasible set. The revised feasible sets are shown graphically in Figure 6.15.

- States of the form $(\boldsymbol{p}, o, \texttt{IN})$ are connected to states labelled `OUT` that lie along the vanishing direction o to the left of $\boldsymbol{p}$. This closely mirrors the situation in Section 6.4.1.
- States of the form $(\boldsymbol{p}, o, \texttt{UP})$ are connected to exactly two other states: the `IN` state for pixel $\boldsymbol{p}$ and the `UP` state for the pixel immediately above $\boldsymbol{p}$. If $\boldsymbol{p}$ is at the top of the image then the latter connection is omitted.

- States of the form $(\boldsymbol{p}, o, \texttt{DOWN})$ are connected to exactly two other states: the `IN` state for pixel $\boldsymbol{p}$ and the `DOWN` state for the pixel immediately below $\boldsymbol{p}$. If $\boldsymbol{p}$ is at the bottom of the image then the latter connection is omitted.
- States of the form $(\boldsymbol{p}, o, \texttt{OUT})$ are connected to exactly three other states: the `IN`, `UP`, and `DOWN` states for $\boldsymbol{p}$.

The motivation for this arrangement of states and feasible sets is that it allows us to solve per–state optimisation problems in terms of the solutions to preceding states. Furthermore, three of the four states now have just a constant number of outgoing edges, while the fourth (states labelled `IN`) have $O(L)$ outgoing edges. In comparison, the feasible sets described in Section 6.4.2 contained $O(L^2)$ states. The value function remains unchanged from the previous sections; all that remains to describe is the per–state optimisation step.

Optimisation step. Let us once again select a particular state $\boldsymbol{s}$ and assume that all preceding states $\boldsymbol{t}$ are already solved — that is, for each $\boldsymbol{t}$ to the left of $\boldsymbol{s}$, we know which indoor Manhattan scene maximises the value function at $\boldsymbol{t}$ and we have also have the output of the value function for that scene (this value will once again be written $\mathsf{Best}(\boldsymbol{t})$). The procedure for computing $\mathsf{Best}(\boldsymbol{s})$ is as follows:

- If $\boldsymbol{s}$ is labelled `UP` or `DOWN` then the optimisation step consists simply of taking the maximum of the value at the two connected states, as depicted in Figure 6.15.
- If $\boldsymbol{s}$ is labelled `IN` then the maximisation is over states along one of the vanishing directions, with an edge cost added. This is identical to the procedure of Section 6.4.1 except that at each pixel we take the value from the state labelled `OUT`.
- For states $(\boldsymbol{p}, o, \texttt{OUT})$, the maximisation is over three predecessor states:

$$(\boldsymbol{p}, o, \texttt{IN})$$

$$(\boldsymbol{p}, o, \texttt{UP})$$

$$(\boldsymbol{p}, o, \texttt{DOWN})$$

One or more of these may be omitted if the physical realisability rules indicate that such a connection would generate a physically impossible wall segment.

Full algorithm. Now that the states, feasible sets, and optimisation steps have been specified, the complete procedure for finding the indoor Manhattan scene maximising (6.6) is as follows. As in Section 6.4.2 we begin at the right edge of the image (specifically with states labelled `IN`). At each state we compute $\mathsf{Best}(\boldsymbol{s})$ using the procedure described above. Each time we need the value for a state that has not yet been evaluated we recursively apply the procedure to that state, terminating this recursive process when we reach the left edge of the image. The only difference between this procedure and that of Section 6.4.2 is that the structure of the state space has changed.

Algorithmic complexity. By introducing auxiliary sub–problems we have increased the total number of sub–problems by a factor of 4. However, the sub–problems `UP`, `DOWN`, and `OUT` have $O(1)$ complexity and the maximisation for `IN` states is now over $O(L)$ terms. Furthermore, the edge costs can now be computed incrementally in constant time. The number of states remains $O(L^2)$ so the complexity of the algorithm presented here is $O(L^3)$.

6.4.5 Third Refinement: From $O(L^3)$ to $O(L^2)$

Evaluating states labelled `IN` remains an $O(L)$ operation because the associated feasible set contains $O(L)$ states. In this section we reduce this to $O(1)$. We will make an approximation in which, as we walk along vanishing lines, we will permit non–integer pixel locations to be replaced by nearby integer pixel locations if the round–off error is smaller than a parameter ϵ. We will show that for any $\epsilon > 0$, we only ever have to consider at most R pixels along the vanishing line before encountering one with a sufficiently small round–off error (where R is a function of ϵ). When we do encounter such a pixel we may terminate the line search, delegating instead to a related sub–problem. Figure Figure 6.16 depicts this modification schematically. After this modification the feasible set for each `IN` state contains a bounded number of states, giving the desired $O(1)$ complexity.

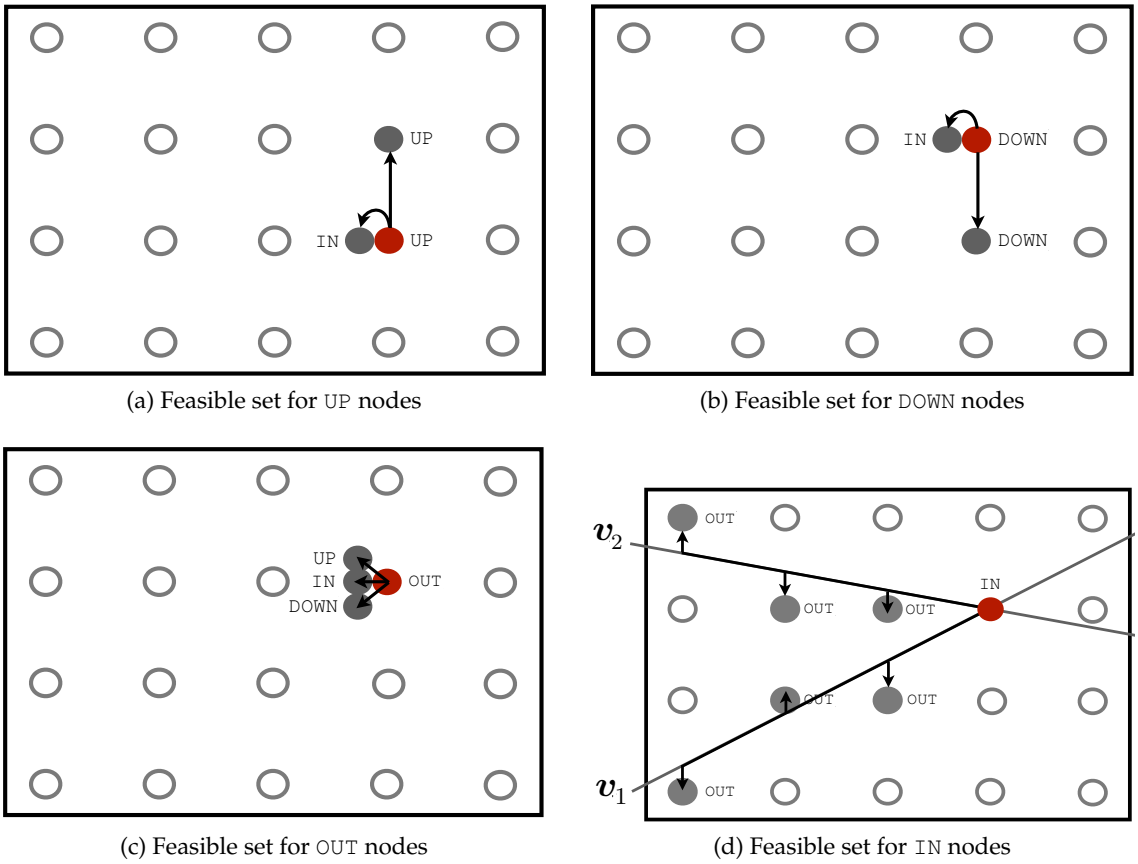

(a) Feasible set for UP nodes

(b) Feasible set for DOWN nodes

(c) Feasible set for OUT nodes

(d) Feasible set for IN nodes

Figure 6.15: The feasible sets for each of the four new node labels introduced in Section 6.4.4. Each panel highlights one node and shows the outgoing edges for just that node. These are repeated for every pixel and orientation.

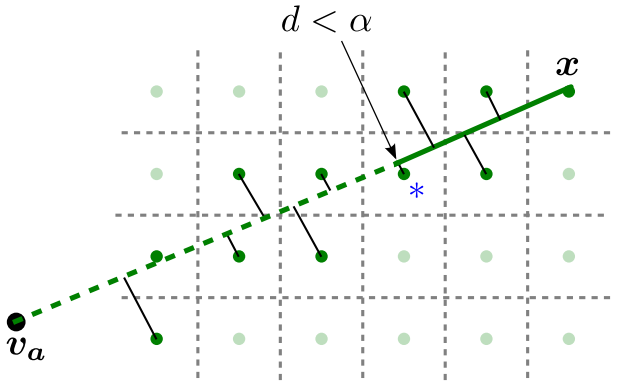

Figure 6.16: Each time we evaluate an IN node we walk along a vanishing line from some state $\boldsymbol{x}$ to a vanishing point $\boldsymbol{v}$ (green line), examining each state we encounter (green dots). The approximation described in Section 6.4.5 permits us to terminate this search when we first encounter a node within a threshold distance of the line (blue asterisk).

To explain this modification, we will first describe how it is that we terminate the line search and which sub–problem we delegate to. We then show that there is an upper bound on the number of steps we must take before finding a state satisfying the termination criteria.

The line search can be terminated

Let us first review the algorithm as presented in Section 6.4.4. There is one IN node for each pixel in the image. Each time such a node is evaluated, we walk from that node to the left edge of the image along a vanishing line, identifying at each column the closest OUT node as depicted in Figure 6.16 and Figure 6.15. In the worst case, the number of steps equals the width of the image so this is an $O(L)$ operation.

Suppose we are evaluating $\mathsf{Best}(\boldsymbol{x}, o, \texttt{IN})$ where $\boldsymbol{x}$ is the node at the top right of Figure 6.16. This evaluation involves walking along the vanishing line shown in green. Consider the node marked with a blue asterisk. If this node lay precisely on the vanishing line then we could make the following substitution. When we reach this node, rather than continuing to walk along the line evaluating $\mathsf{Best}(\boldsymbol{p}, o, \texttt{OUT})$ at each column, we could instead make a single call to $\mathsf{Best}(\boldsymbol{p}^*, o, \texttt{IN})$ where $\boldsymbol{p}^*$ is the node marked with the asterisk. This substitution is valid for the following reason. The sub–problem $\mathsf{Best}(\boldsymbol{p}^*, o, \texttt{IN})$ consists of a maximisation over all nodes along the vanishing line to its left, but these nodes are precisely the nodes that we would

have enumerated had we continued the original line search. Hence the substitution replaces a maximisation over $O(L)$ nodes with a single evaluation — an $O(1)$ operation.

Now in actuality the node marked with an asterisk in Figure 6.16 does not lie precisely on the vanishing line and in general we cannot expect to find integer–valued pixels that do. Hence we introduce the following approximation. Whenever a pixel falls within a distance ϵ of a vanishing line we treat it as though it fell precisely on the vanishing line and apply the substitution described above. How many steps might we have to take before encountering a sufficiently close pixel? We show below that there is a global upper bound on the number of steps that we ever have to take. In our experiments we found that even a threshold as small as $\epsilon = 0.01$ produced a significant speedup.

The feasible set contains a bounded number of states.

A bound on number of steps that we might have to take when evaluating an `IN` node is provided by the following lemma.

Lemma 5. *For all $\epsilon > 0$ there exists $R > 0$ such that for any $(x, y) \in \mathbb{Z}^2$ and any $(v_x, v_y) \in \mathbb{R}^2$ there is some $(p, q) \in \mathbb{Z}^2$ with $x - R \leq p < x$ such that*

$$\frac{|(v_y - y)(p - x) - (v_x - x)(q - y)|}{\sqrt{(v_x - x)^2 + (v_y - y)^2}} \leq \epsilon \tag{6.63}$$

Further, the above holds for

$$R = \epsilon\sqrt{2} + \frac{1}{\epsilon} \tag{6.64}$$

Proof. First we substitute $r = p - x, s = q - y, a = \frac{v_y - y}{\sqrt{(v_y-y)^2+(v_y-y)^2}}$, and $b = \frac{v_x - x}{\sqrt{(v_x-x)^2+(v_y-y)^2}}$,

$$|ar - bs| < \epsilon \tag{6.65}$$

Next, noting that $[a, b]$ is a unit vector and without loss of generality letting $a \geq b$ we have

$$\left|\frac{b}{a}s - r\right| \leq \frac{\epsilon}{a} \leq \epsilon\sqrt{2}\,. \tag{6.66}$$

Dirichlet's theorem [44] guarantees the existence of a pair (r, s) with $1 \leq s \leq \frac{1}{\epsilon}$. Rearranging the above we get

$$|r| \leq \epsilon\sqrt{2} + \left|\frac{b}{a}s\right| \tag{6.67}$$

$$\leq \epsilon\sqrt{2} + \frac{1}{\epsilon}\,. \tag{6.68}$$

Without loss of generality we assume $r < 0$ (since we may multiply both r and s by -1), yielding

$$-\epsilon\sqrt{2} - \frac{1}{\epsilon} \leq r < 0 \tag{6.69}$$

$$-\epsilon\sqrt{2} - \frac{1}{\epsilon} \leq p - x < 0 \tag{6.70}$$

$$x - R \leq p < x\,. \tag{6.71}$$

where $R = \epsilon\sqrt{2} + \frac{1}{\epsilon}$. □

Algorithmic Complexity

For fixed ϵ, the number of terms required to evaluate a `IN` node is bounded by a constant independent of the problem size. Since the other three sub–problems are unchanged, all sub–problems are now $O(1)$ operations and the overall complexity of the algorithm is given by the total number of unique sub–problems, which is $O(L^2)$.

6.5 Results

Our data–set consists of 18 manually annotated video sequences of 8 unique indoor locations averaging 59 seconds in duration. We sample frames at one second intervals and divide frames into consecutive blocks of 3 (one base frame and two auxiliary frames). Our evaluation set consists of 150 such triplets generated from 8 different sequences.

To acquire ground truth data we reconstructed camera trajectories using structure–from–motion

software, then manually specify the ground truth floor–plan. Recall that we seek to recover the *boundaries* of the environment, whether or not they are visible at every pixel. When our algorithm ignores clutter within a room, we consider that a *success*.

The monocular features ϕ_i consist of 3 RGB channels, 3 HSV channels, 24 Gabor filters (4 scales, 6 orientations), and 3 binary line sweep features [43]. For stereo we use patches of size 5×5 and when computing photoconsistency terms we normalise all images to zero mean and unit variance.

For these experiments, we fixed the various hyper–parameters using a simple bootstrapping algorithm evaluated on a separate training set. This approach is discussed in a published paper [24]; we omit it here because it is superseded by the more principled and effective learning algorithm described in the following chapter, and because in later experiments we found that it did not substantially improve upon manually chosen values. Qualitatively, the discriminative power of our model comes from the strong geometric feasibility constraints, the global inference algorithm, and the Bayesian sensor models.

We compute two error metrics: the labelling accuracy, which is the proportion of all pixels that were labelled with the correct surface orientation, and the mean relative depth error, computed per–pixel with respect to ground truth. While the latter better captures similarity to the ground truth, one of the systems we compared with did not have a direct 3D interpretation, so we compared on labelling accuracy.

To the best of our knowledge, there is no previously published work other than our own on precisely this problem (indoor–Manhattan reasoning from multiple views), so we compare with three different systems, though neither comparison is ideal. Our first comparison is with the approach of Brostow *et al.* [7], who performed semantic segmentation by training a per–pixel classifier on structure–from–motion cues. Our implementation of their system uses exactly the features they describe, with classes corresponding to the three Manhattan orientations. While they trained a randomised forest, we trained a multi–class SVM because a reliable SVM library was more readily available to us. Given the margin between our results it is unlikely that a

different classifier would significantly change the outcome. The second comparison is with the monocular approach of Lee *et al.* [43]. One would of course expect a multiple view approach to outperform a monocular approach, but as one of the very few previous approaches to have explicitly leveraged the indoor Manhattan assumption we feel this comparison is important to demonstrate the benefit of a Bayesian framework and integration of stereo and 3D cues.

Our third comparison is with the stereo approach of Zeisl *et al.* [75], which leverages a "vertical structure" prior that is similar to our own indoor Manhattan assumption. Their payoff function is identical to our stereo payoff function, but they employ a different prior, and hence a different optimisation algorithm. Like the indoor Manhattan assumption, their prior insists on a floor and ceiling plane with vertical surfaces extending continuously between them. Unlike the indoor Manhattan assumption, they allow surfaces at any vertical orientation and they allow these surfaces to bend and curve arbitrarily (although they do penalise changes in orientation and depth with pair–wise potentials). The assumption of a floor and ceiling plane allows the authors to adopt a column–wise labelling scheme similar to the seam representation we described in Chapter 4. The relationship between their dynamic programming formulation and our own is that we reason in terms of discrete wall segments in the vertex representation (and hence our regularisation is in terms of discrete wall segments), while they reason directly in the seam representation and restrict themselves to regularisation potentials defined over neighbouring image columns. We implemented the first extension described in their paper ("slope based smoothness terms") but not the second ("model selection") since the latter permits non–Manhattan structure yet all ground truth data in our dataset contains only Manhattan structure.

The performance of each system is shown in Figure 6.1. Even when restricted to monocular features, our system outperforms [7], which has access to 3D cues. This reflects the utility of global consistency and the indoor Manhattan representation in our approach. The initialisation procedure of [43] fails for 31% of our training images, so at the bottom of Figure 6.1 we show results for their system after excluding these images. Labelling accuracy increases to within 3% of our monocular–only results, though on the depth error metric a margin of 10% remains. Figure

6.1 also shows that joint estimation is superior to using any one sensor modality alone. Anecdotally we find that using 3D cues alone often fails within large textureless regions in which the structure–from–motion system failed to track any points, whereas stereo or monocular cues alone often perform better in such regions but can lack precision at corners and boundaries.

We found that the the system of Zeisl *et al.* was most likely to produce incorrect reconstructions at image columns where multiple vertical surface were observed, such as when looking through a window or doorway, or when cabinets or other box–structured furniture was visible. The vertical surfaces on these objects are strong attractors for the stereo likelihood and often caused this system to mistake, for example, the front of a cabinet for a wall. A similar observation was made by Zeisl *et al.* of their own system [75]. Our own stereo–only experiments showed similar errors, though the addition of 3D and monocular features often resolved these ambiguities. We note that even when restricted to stereo clues alone, in which case the systems are differentiated only by their priors, our system out–performed that of Zeisl *et al.*. One thing to note here is that our ground truth data always considers room boundaries to be the correct reconstruction, even when a wall is completely occluded by a piece of furniture. This reflects our goal of extracting simple and meaningful geometric summaries from images, and means that our system (which explicitly models floorplans) has an advantage on this dataset. In contrast, for robot navigation, which is one of the goals stated by Zeisl *et al.*, it may instead be more important to identify all vertical surfaces in the scene, whether walls or objects.

We have noticed that one source of errors is vanishing points that are slightly mis–estimated, which is often due to errors in the underlying reconstruction provided by structure–from–motion. When vanishing points deviate slightly from their true position, our reconstruction system inserts very narrow wall segments to "correct" for the mis–localisation, forming small zig–zags in order to track the observed image gradients. Examples of this phenomenon are shown in rows 6 and 7 of Table 6.2. Although this does not pose a major concern for our system, one way to correct for it would be to jointly refine structure, motion, and vanishing points, as in [63].

Figure 6.17 shows timing results for our system. For each triplet of frames, our system requires

Algorithm	Mean depth error (%)	Labelling accuracy (%)
Our approach (full)	**14.5**	**75.5**
Stereo only	17.4	69.5
3D only	15.2	71.1
Monocular only	24.8	69.2
Brostow *et al.* [7]		40.6
Zeisl *et al.* [75]	18.0	
Lee *et al.* [43]	79.8	45.5
excluding failures[5]	34.1	66.2

Table 6.1: Performance on our data–set. Labelling accuracy is the percentage of correctly labelled pixels over the data–set, and depth error is the mean relative depth error. There is no depth error in row 5 because that system does not generate 3D models, and there is no labelling error in row 6 because that system does constrain surfaces to the three Manhattan orientations.

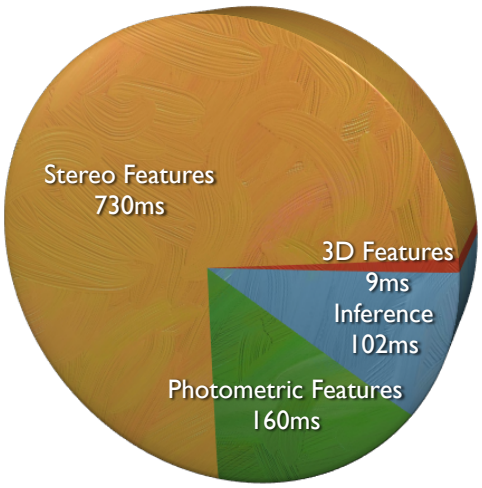

Figure 6.17: Processing time for feature computation and inference in our system, averaged over all evaluation instances. The mean total processing time was 997ms.

on average less than one second to compute features for all three frames and less than 100 milliseconds to perform optimisation.

[5]This row excludes cases for which [43] was unable to find overlapping lines during initialisation.

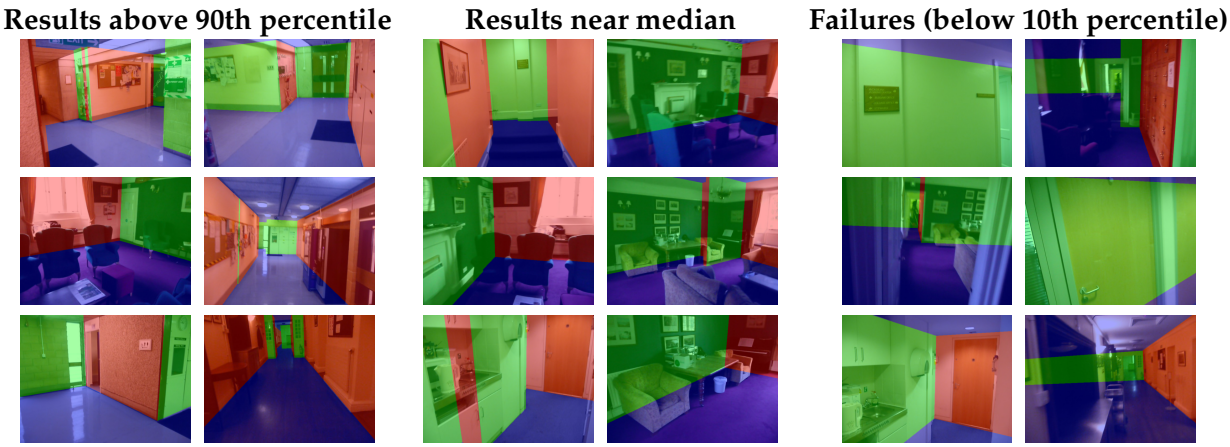

Figure 6.18: Scenes output from our system. The left column shows results above the 90th percentile of performance (relative depth error), the middle column shows results near median performance, and the right column shows failure cases.

Table 6.2: Here we show further examples of scenes inferred by our system. In the table below, the left panel shows the base input view, the middle panel shows the two auxiliary views used for photo–consistency calculations, and the right panel shows the MAP scene M inferred by our system.

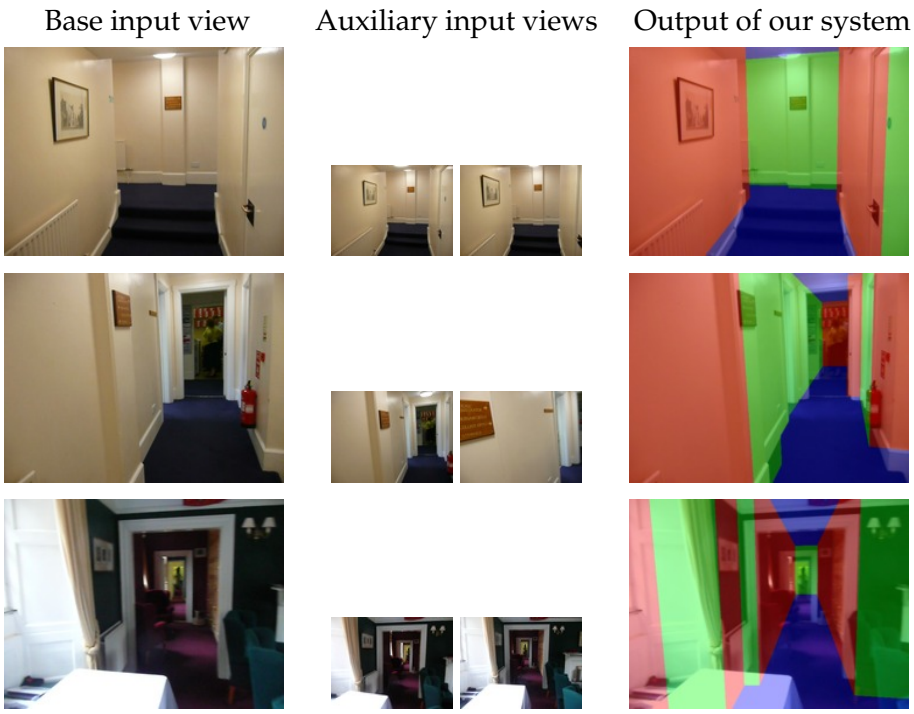

Continued on next page

Continued on next page

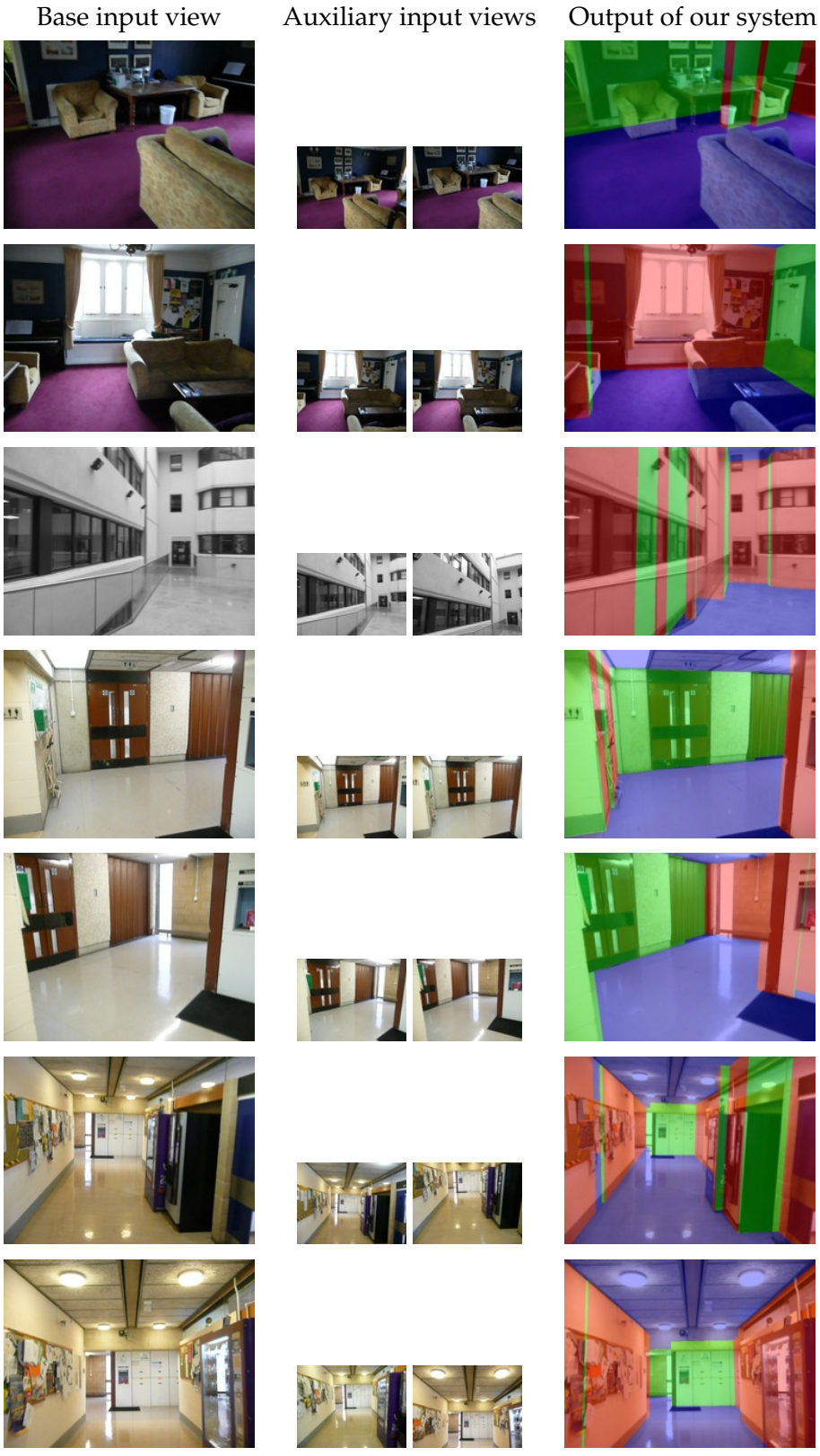

Continued on next page

Continued on next page

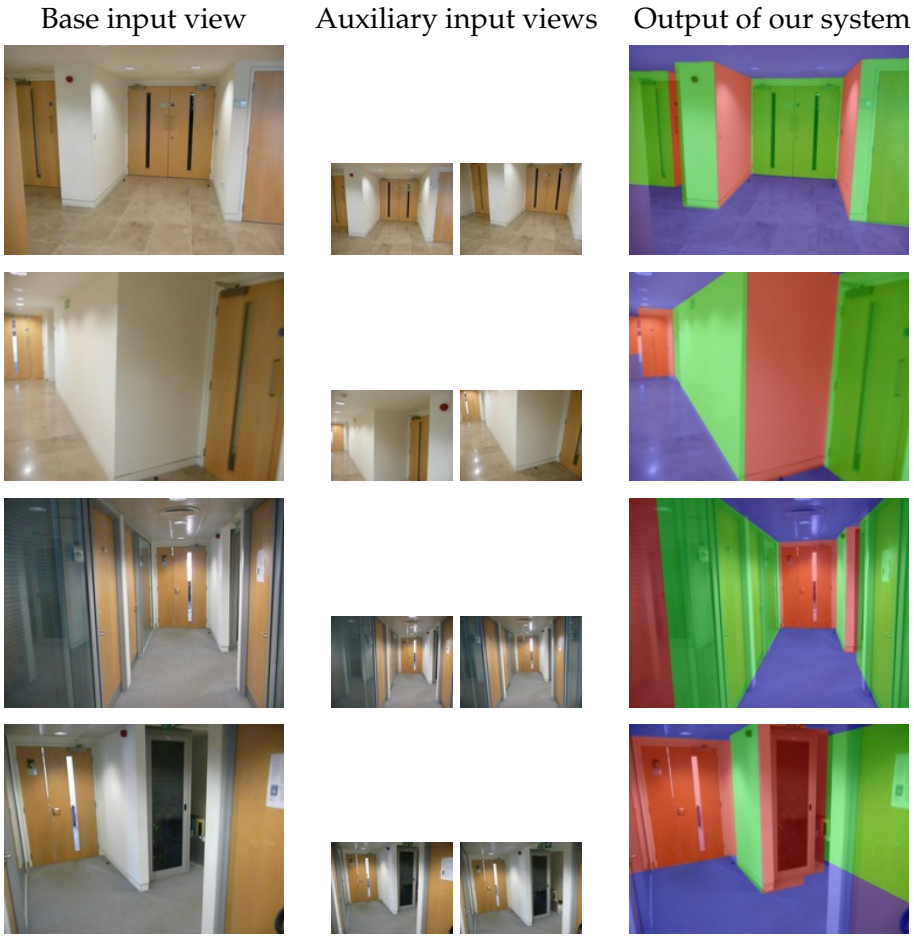

6.5.1 Payoff Matrices

In this section we provide some visualisations of the payoff matrices discussed above in order to give extra insight into the structure of each sensor modality.

The raw image provided as input to our system.

The ground truth segmentation for this image. Horizontal surfaces are shaded blue. Vertical surfaces are shaded red and green. We will refer to these as the "red" and "green" orientations.

The MAP indoor manhattan model $\boldsymbol{w}$ output by our system for this input.

Payoffs π_{mono} derived from monocular image features, for the "green" orientation. Pixels of higher intensity correspond to larger values in the payoff matrix. The MAP model is shown in wireframe using red lines. Intuitively, the optimisation over models can be thought of as finding the minimal cost path through the payoff matrix, where higher intensity pixels correspond to lower costs. This is only a rough picture, however; the real optimisation situation is more complex since models are penalised for each additional corner.

As above, for the "red" surface orientation.

Auxiliary images used for stereo photo–consistency. In our experiments we used two image auxiliary images for each base image, which were sampled one second before and one second after the base image in the video sequence.

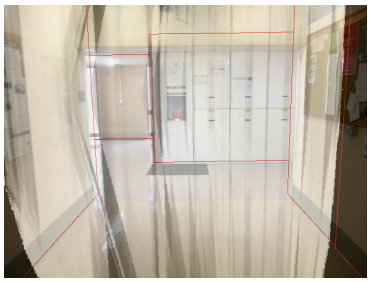

Payoffs π_{stereo} corresponding to the auxiliary images above. Each pixel represents the photo–consistency score for a wall segment with floor/wall (or ceiling/wall) intersection that point at that pixel. Notice the repeated "pizza slice" patterns in which one tip of the triangle is located at the floor/wall intersection.

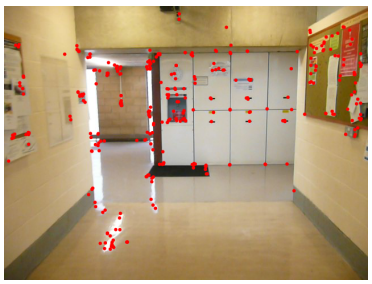

Here we show the structure–from–motion point cloud. The points are shown projected into the image, but the system has access to their 3D locations. Notice how the points are not uniformly distributed in the image.

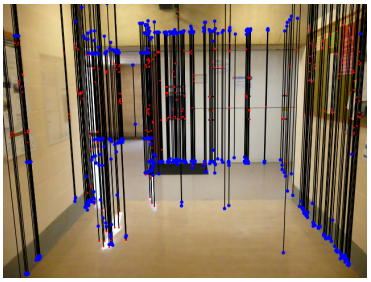

Here we show the structure–from–motion point cloud projected onto the floor and ceiling planes, which were recovered as a separate step as described in the main paper. The red dots show the original 3D point cloud and the blue dots show the projections onto the floor and ceiling.

This shows the component of the payoffs π_{3D} intended to provide a bias towards models that explain the observed 3D points. This is the component corresponding to $t = \mathsf{ON}$. Each bright spot corresponds to the projection of a 3D point onto the floor or ceiling plane.

This shows the component of the payoffs π_{3D} intended to penalise walls that occlude observed 3D points. This corresponds to the case that $t \in \{\mathsf{IN}, \mathsf{OUT}\}$. Notice that for each 3D point, payoffs are assigned to walls that pass between the floor and ceiling projection of that point. Such walls are precisely those which do *not* occlude the point.

Joint payoff matrix π_{joint}.

6.6 Other Approaches

In this section we briefly discuss the conceptual differences between our algorithm and two related approaches.

6.6.1 Branch and Bound

Lee *et al.* [43] proposed a branch–and–bound solution to a similar inference problem to that considered in this chapter. Their approach identifies straight lines in the image and then searches over all possible combinations, generating from each combination a scene hypothesis. The hypotheses are evaluated using a cost function similar to (6.50). Whereas the algorithmic complexity of their algorithm is exponential in the number of lines used to generate scene hypotheses, our approach is *independent* of scene complexity; yet our hypothesis class is a strict superset of theirs.

Their approach also differs from ours in that they only allow wall boundaries to occur where lines are observed in the image. We have found this to be unnecessary because the objective (6.4) already incorporates this information. Furthermore, our system avoids dependence on edge detection, whereas Lee *et al.* are unable to find the correct model if one or more structurally important edges are missed by the edge detector.

6.6.2 Graph Cuts

Many pixel–labelling problems can been solved using graph cuts. Kolmogorov and Zabih [41] showed that only regular functions (a subset of sub–modular functions) can be minimised via graph cuts. Interpreted as an energy, (6.4) is not regular because implicit in the optimisation is the hard constraint that labellings must form an indoor Manhattan model, which induces complicated dependencies between the pixels in each column. For example, if we were to optimise directly within a labelling representation then if some pixel $\boldsymbol{p}$ were assigned label a then $\boldsymbol{q} = H_a\boldsymbol{p}$ must be assigned the same label, even though the two may be arbitrarily far from one another in the image. Further, if a were either of the vertical orientations then no pixel in the same column can be assigned the opposing vertical orientation, leading to cliques of size equal to the height of the image. These constraints only capture a fraction of the full feasibility requirements.

Even if an appropriate relaxation of this constraint yielded a regular cost function, applying

graph cuts would entail using a technique such as α–expansion [41], which is both approximate and non–deterministic. In contrast, our approach is exact, deterministic, and highly efficient.

6.7 Discussion

In this section we discuss a possible generalisation of our model to relax the constraint on priors.

6.7.1 Non–memoryless Scene Priors

Recall that our prior on scenes (6.7) is

$$P(M \mid \boldsymbol{\lambda}) = \frac{1}{Z}{\lambda_1}^{n_1}{\lambda_2}^{n_2}{\lambda_3}^{n_3} \tag{6.72}$$

This prior is memoryless because it corresponds to the outcome of a series of independent trials. Intuitively, memorylessness means that the marginal probability of each additional wall is independent of the number of walls already added to a model. Formally, memorylessness is defined by the necessary and sufficient condition

$$P(n_i = k + m \mid n_i \geq k, \boldsymbol{\lambda}) = P(n_i = m \mid \boldsymbol{\lambda}) \, . \tag{6.73}$$

This property is important for the algorithm presented above because the logarithm of a memoryless prior is linear in the hyper–parameters, which we used to write the prior as a sum over independent penalties for each corner category in (6.9). On this basis we defined sub–problems independently of the number of corners and were able to incorporate penalties as additive terms in our algorithm. With a non–memoryless prior this is impossible because the marginal probability of an additional corner is no longer independent of the number of corners already added.

How well does (6.72) reflect our actual prior expectations for scenes? Certainly the provision

that complex scenes are apriori less likely than simple scenes matches our intuition, but the assertion that a scene composed of just one wall is more likely than a scene with two or three walls seems less justified. Here we show how one could incorporate any prior that can be written as a function of n_1, n_2, n_3 (memoryless or not), at the cost of introducing extra dimensions to the state space and a corresponding increase in the computational complexity of the algorithm. We have not implemented this algorithm.

Let $\boldsymbol{n} = [n_1,\ n_2,\ n_3]$ be a vector containing three integers. First we redefine the state space to incorporate $\boldsymbol{n}$,

$$\mathcal{S} = \{(x, y, o, \boldsymbol{n})\} \tag{6.74}$$

$$\mathcal{S} = [1, W] \times [1, H] \times \{1, 2\} \times \mathbb{Z}^3 \tag{6.75}$$

Next we refine the sub–problem definitions as follows.

Definition 2. *A scene M satisfies $f_{in}(x, y, o, n_1, n_2, n_3)$ iff it terminates at (x, y, o) and contains exactly n_1 concave corners, n_2 convex corners, and n_3 occluding corners.*

The other three sub–problems are redefined similarly.

Let ω be a function identifying the category of the corner resulting from concatenating a wall $W = (x_0, y_0, o_0, x_1)$ to a scene M terminating at (x_b, y_b, o_b). By Definition 1, ω is functionally dependent only on the values

$$x_b, o_b,\ o_0,\ \mathrm{Sign}(y_0 - y_b) \tag{6.76}$$

so we write

$$\omega(x, o_1, o_2, s) = \begin{cases} [1\ 0\ 0], & \text{for concave corners} \\ [0\ 1\ 0], & \text{for convex corners} \\ [0\ 0\ 1], & \text{for occluding corners} \end{cases} . \tag{6.77}$$

The only recurrence relation we need to update is that for nodes labelled OUT, which becomes

$$\begin{aligned}\textsf{Best}(x, y, o, \boldsymbol{n}, \texttt{OUT}) = \max_{o' \in \{l,r\}} \max\Big(&\textsf{Best}(x, y-1, o', \boldsymbol{n} - \omega(x, o', o, -1), \texttt{UP}), \\ &\textsf{Best}(x, y, o', \boldsymbol{n} - \omega(x, o', o, 0), \texttt{IN}), \\ &\textsf{Best}(x, y+1, o', \boldsymbol{n} - \omega(x, o', o, +1), \texttt{DOWN}) \Big)\end{aligned} \tag{6.78}$$

Comparison with the previous algorithm shows that we have replaced the penalty term with a transition from $\boldsymbol{n}$ to $\boldsymbol{n}' = \boldsymbol{n} - \omega(\cdot)$. This means our sub–problems no longer incorporate penalties at all, instead we have expanded our state space to incorporate that information in a different form. In order to solve for the optimal scene we will need to enumerate many terminating states:

$$f(M^*) = \max_{y,o,\boldsymbol{n}} f_{in}(W, y, o, \boldsymbol{n}) - P(\boldsymbol{n} \mid \boldsymbol{\lambda}) \; . \tag{6.79}$$

At the cost of a substantial expansion of the state space we are now able to optimise with respect to a larger class of priors.

6.7.2 Conclusion

We have presented a Bayesian framework for scene understanding in the context of a moving camera. Our approach draws on the indoor Manhattan assumption introduced for reasoning from single views and we have shown that techniques from monocular and stereo vision can be integrated with geometric observations in a coherent Bayesian framework. We have connected inference in our model to a class of optimisation problems that we labelled the payoff formulation, and we have presented an efficient and exact solution in the form of a dynamic programming algorithm. Our approach is able to model complex scenes, which would be intractable for previous methods that involved combinatorial searches in the space of models. Experiments show our system out–performing two similar systems for both single– and multiple–view inference.

7

Learning to Construct Indoor Manhattan Models

We develop a structured prediction approach to reconstructing 3D polygonal models from single and multiple images of a scene. Building on recent advances in single view reconstruction we adopt the indoor Manhattan hypothesis class — one of the most complicated output spaces (in terms of internal constraints) yet considered within a structured prediction framework. Our approach can learn in both the single– and multiple–view contexts. We show that the chosen hypothesis class permits optimising a variety of high–level loss functions, such as the relative depth error. Our results out–perform the state–of–the–art, including an improvement of more than 50% on one metric.[1]

7.1 Introduction

Previous chapters cast scene understanding as a fixed inference problem, with each input instance considered separately. Such systems have no capacity to improve their accuracy over time based on feedback from past predictions, since there is no information carried over from

[1] At the time of publishing, part of the work presented in this chapter was under review for the 2012 European Conference on Computer Vision.

one inference task to the next. This chapter considers the task of learning to recover indoor Manhattan models based on labelled training examples. We are given a series of input images together with ground truth reconstructions, and the goal is to discover a rule to recover the correct scene structure from future images.

We adopt the standard approach in machine learning of distinguishing a learning phase — a one–off computation performed ahead of time — from the inference phase — in which the results of the learning phase are used to label incoming training examples. This chapter focuses on the learning phase; we will show that under the learning scheme we propose, inference reduces to exactly the algorithm presented in the previous chapter. As a result, the approach described in this chapter is strictly complimentary to the inference algorithm described in Chapter 6.

In this chapter we emphasise a learning–based approach to recovering scene structure. Traditionally, neither the single– nor multiple–view reconstruction literature places learning at the heart of the reconstruction problem. Within single–view reconstruction, for example, few authors cast learning as a single optimisation with respect to a clearly defined loss function [34, 58, 43, 24]. On the other hand, multiple–view reconstruction techniques rarely learn from training data at all. In contrast, this chapter casts reconstruction fundamentally as a learning problem, with the goal being to learn a prediction function f mapping observed image features to indoor Manhattan reconstructions.

Using indoor Manhattan reconstructions as the hypothesis class brings a variety of attractive features such as a simple parametrisation, efficient and exact inference, and a balance between expressiveness and robustness, as has been discussed in preceding chapters. In this chapter we show that this hypothesis class also leads to a convenient decomposition of loss functions mirroring the likelihood decomposition described in Chapter 6, which permits efficient optimisation of several popular image–level losses.

For learning we employ the tools of structured prediction — in particular, the structured support vector machine [68]. The use of these tools is part of a long trend within computer vision

towards statistically rigorous, well–understood convex optimisation techniques. Recent successfully applications of the structured SVM include detection [6], segmentation [65, 66], and scene classification [74]. In the domain of reconstruction, structured prediction ideas have been applied to several simple model classes such as stereo disparities [45] and cuboids [31].

The application of structured prediction to the indoor Manhattan class of models constitutes one of the most complex output spaces yet considered within this framework. The indoor Manhattan model enforces hard geometric constraints that lack simple expressions in terms of individual pixel labels. These constraints are time–varying, being tied to quantities such as camera rotation and the location of vanishing points. We have learnt several valuable lessons of general relevance from this complex prediction task, to which we dedicate the final section of this chapter.

The contributions of this chapter are thus (i) a unified learning framework for single– and multiple–view reconstruction, utilising the indoor Manhattan model and the tools of structured prediction; (ii) the reduction of two image–level loss functions to a form amenable to efficient optimisation; (iii) an efficient separation procedure for identify the "most–violated constraint" during learning, (iv) an empirical demonstration of structured prediction in perhaps the most complex output space yet considered within this framework; and (v) a series of practical observations concerning the application of structured prediction techniques to complicated output spaces.

7.2 Background

The approach to learning adopted in this chapter has roots in the structural risk minimisation framework developed by Vapnik and Chervonenkis [70]. On this view, learning is framed in terms of a predictor f, which maps from an input space $\mathcal{X}$ to an output space $\mathcal{Y}$. Learning consists of minimising the expected loss

$$\mathbb{E}\big[\Delta(f(\boldsymbol{x}), \boldsymbol{y})\big] = \int \Delta\big(f(\boldsymbol{x}), \boldsymbol{y}\big)\, \mathrm{d}P(\boldsymbol{x}, \boldsymbol{y}) \tag{7.1}$$

with respect to the predictor f, where Δ is a loss function. Given training samples $(\boldsymbol{x}_i, \boldsymbol{y}_i) \in \mathcal{X} \times \mathcal{Y}$, the integral above is approximated by

$$\sum_i \Delta\big(f(\boldsymbol{x}_i), \boldsymbol{y}_i\big) \,. \tag{7.2}$$

Structural risk minimisation techniques add a regulariser $\mathcal{R}$:

$$\mathcal{R}(f) + \sum_i \Delta\big(f(\boldsymbol{x}_i), \boldsymbol{y}_i\big) \tag{7.3}$$

Structural risk minimisation does not specify any particular form for the input space, output space, predictor class, or loss function. Many machine learning algorithms can be viewed as instantiations of structural risk minimisation for particular predictor classes and loss functions. For example, the classic support vector machine (SVM) [11] is defined for Hilbert input spaces, binary output spaces, the hypothesis class of linear predictors, and the Hinge loss function. In this case equation (7.3) becomes

$$\|\boldsymbol{w}\|^2 + \sum h(\boldsymbol{y}_i, \boldsymbol{w} \cdot \boldsymbol{x}_i)) \tag{7.4}$$

where h is the hinge loss, and learning consists of minimisation with respect to $\boldsymbol{w}$. Rewriting the hinge loss as a penalised linear constraint leads to the well–known quadratic programming formulation for the SVM [11].

Extending binary classification to more general output spaces is a major research programme within machine learning; an excellent introduction to recent advances is given by Bakir *et al.* [2]. One recently successful approach is the structured support vector machine proposed by Tsochantaridis *et al.* [68], which reduces learning in non–binary ("structured") output spaces to a ranking problem. The structured SVM makes use of a joint feature space $\Psi(\boldsymbol{x}, \boldsymbol{y})$ mapping input/output pairs to real vectors. The hypothesis class consists of predictors of the form

$$f(\boldsymbol{x}; \boldsymbol{w}) = \operatorname*{argmax}_{\boldsymbol{y}} \big\langle \boldsymbol{w}, \Psi(\boldsymbol{x}, \boldsymbol{y}) \big\rangle \tag{7.5}$$

where $\boldsymbol{w}$ is a parameter vector and $\langle \cdot, \cdot \rangle$ denotes an inner product. As in the classic SVM, the hinge loss is used to define the objective function,

$$\|\boldsymbol{w}\|^2 + \sum h(\boldsymbol{y}_i, f(\boldsymbol{x}_i)) \; . \tag{7.6}$$

In order to optimise with respect to $\boldsymbol{w}$, Toschantaridis *et al.* showed how to write (7.6) as a constrained optimisation problem parallelling the classic SVM:

$$\begin{aligned} &\min_{\boldsymbol{w},\boldsymbol{\xi}} \; \frac{1}{2}\|\boldsymbol{w}\|^2 + C\sum_{i=1}^{n} \xi_i \\ &s.t. \; \forall k, \boldsymbol{y} \neq \boldsymbol{y}_i : \; \left\langle \boldsymbol{w}, \Psi(\boldsymbol{x}_i, \boldsymbol{y}_i) \right\rangle - \left\langle \boldsymbol{w}, \Psi(\boldsymbol{x}_i, \boldsymbol{y}) \right\rangle \geq \Delta(\boldsymbol{y}, \boldsymbol{y}_i) - \xi_i \; . \end{aligned} \tag{7.7}$$

Unfortunately the number of constraints in (7.7) is in general very large since there is a constraint for every element of the output space. Tsochantaridis *et al.* [68] showed how to overcome this by exploiting the sparsity structure of support vector machines. Their algorithm iteratively adds constraints beginning with zero constraints, and they showed that only a polynomial number of constraints need ever be added in order to achieve an ϵ–accurate solution. The remainder of this chapter shows how to use the structured SVM to learn to reconstruct indoor Manhattan models.

7.3 Model

In this section we describe three components of the model that we are trying to learn (and, at test time, infer): a hypothesis class, a feature space, and a loss function. In our setup these are, respectively, the class of indoor Manhattan models, a log–linear Bayesian likelihood, and either the relative depth error or a labelling error (we describe both).

7.3.1 Hypothesis Class

This chapter is concerned with the output space consisting of indoor Manhattan reconstructions as described in Chapter 4. For consistency with preceding chapters we use the following notation: our input space consists of observed image features denoted Φ, and the output space consists of indoor Manhattan reconstructions in the seam representation denoted S. A training sample is then a set of pairs $\{(\Phi_i, S_i)\}$.

7.3.2 Feature Space

In order to learn to reconstruct indoor Manhattan models we must define a family of prediction functions f mapping image features to indoor Manhattan models. Building on Chapter 6, we would like each predictor to implement MAP inference for some value of the hyper–parameters, *i.e.* we are interested in predictors of the form

$$f(\Phi) = \operatorname*{argmax}_S P(S \mid \Phi, \boldsymbol{w}) \tag{7.8}$$

for various $\boldsymbol{w} \in \mathbb{R}^n$. In other words, we would like to optimise over the set

$$\left\{ f \;\middle|\; f : \Phi \longmapsto \operatorname*{argmax}_S P(S \mid \Phi, \boldsymbol{w}), \boldsymbol{w} \in \mathbb{R}^n \right\} \tag{7.9}$$

consisting of MAP inference predictors for all possible hyper–parameter values, which we have grouped into the parameter $\boldsymbol{w}$. In order to employ the structured SVM we need to write f in the form (7.5), or equivalently, we need to write the logarithm of the posterior on scene structure in the form

$$\log P(S \mid \Phi, \boldsymbol{w}) = \left\langle \boldsymbol{w}, \Psi(\Phi, S) \right\rangle . \tag{7.10}$$

That is, we need to show that the posterior described in the previous chapter is log–linear. The remainder of this section is devoted to defining a joint feature map Ψ permitting such a representation. We now examine each term in the posterior (6.42), our goal being to show that each is log–linear in the relevant hyper–parameters.

Prior

Recall the log–prior (6.8), which is repeated below.

$$\log P(S \mid \boldsymbol{\lambda}) = -\log Z + n_1 \log \lambda_1 + n_2 \log \lambda_2 + n_3 \log \lambda_3 \,. \tag{7.11}$$

Defining $\boldsymbol{n} = \begin{bmatrix} n_1 & n_2 & n_3 \end{bmatrix}$ we have

$$\log P(S \mid \boldsymbol{\lambda}) = \left\langle \boldsymbol{\lambda}, \boldsymbol{n} \right\rangle \ + O(1) \,. \tag{7.12}$$

Photometric Likelihood

Combining (6.15) and (6.11), the log likelihood for photometric features that was described in Chapter 6 is

$$\log P(\Phi \mid S) = \sum_i \boldsymbol{\omega}_{a_i^*} \cdot \boldsymbol{\phi}_i \ + O(1) \,. \tag{7.13}$$

where the sum is over pixels, and, as defined in Chapter 6, a_i^* is the orientation predicted by S for pixel i, $\boldsymbol{\omega}_a$ is the model for photometric features given orientation a, and $\boldsymbol{\phi}_i$ is the feature observed at pixel i. We define

$$\boldsymbol{\omega} = \begin{bmatrix} \boldsymbol{\omega}_1 \\ \boldsymbol{\omega}_2 \\ \boldsymbol{\omega}_3 \end{bmatrix} \qquad \Psi_{\mathsf{mono}}(\Phi, S) = \begin{bmatrix} \sum_{i:a_i^*=1} \boldsymbol{\phi}_i \\ \sum_{i:a_i^*=2} \boldsymbol{\phi}_i \\ \sum_{i:a_i^*=3} \boldsymbol{\phi}_i \end{bmatrix} \,. \tag{7.14}$$

Finally we can write

$$\log P(\Phi \mid S) = \left\langle \boldsymbol{\omega}, \Psi_{\mathsf{mono}}(\Phi, S) \right\rangle \ + O(1) \,. \tag{7.15}$$

Photo–consistency Likelihood

The log likelihood for photo–consistency features given by equation (6.24) is

$$\log P(\Phi, \Theta_1, \ldots, \Theta_K \mid S) = \sum_i \sum_{k=0}^{K} \|\boldsymbol{\phi}_i - \bar{\boldsymbol{\theta}}_k(\boldsymbol{p}_i; S)\|_\Sigma \,. \tag{7.16}$$

Here we assume that

$$\Sigma^{-1} = \mathrm{diag}(\sigma_1, \ldots, \sigma_2) \,. \tag{7.17}$$

It follows that by defining

$$\boldsymbol{\sigma} = \begin{bmatrix} \sigma_1 \\ \vdots \\ \sigma_m \end{bmatrix} \qquad \Psi_{\text{stereo}}(\Phi, S) = \begin{bmatrix} \sum_i \sum_{k=1}^{K} \big((\boldsymbol{\phi}_i)_1 - (\bar{\boldsymbol{\theta}}_k(\boldsymbol{p}_i; S))_1\big)^2 \\ \vdots \\ \sum_i \sum_{k=1}^{K} \big((\boldsymbol{\phi}_i)_m - (\bar{\boldsymbol{\theta}}_k(\boldsymbol{p}_i; S))_m\big)^2 \end{bmatrix} \tag{7.18}$$

we can write the log likelihood (7.16) in the form

$$\log P(\Phi, \Theta_1, \ldots, \Theta_K) = \left\langle \boldsymbol{\sigma}, \Psi_{\text{stereo}}(\Phi, S) \right\rangle \ + O(1) \,. \tag{7.19}$$

Point Cloud Likelihood

The log–likelihood for point cloud features (6.35) is non–linear so for the purpose of learning we approximate it by a first order Taylor expansion about $\boldsymbol{\tau_0}$ as follows.

$$\log P(d \mid S, \boldsymbol{\tau}) \ \approx \ \frac{\sum_t P(d \mid S, t) P(t \mid \boldsymbol{\tau})}{\sum_t P(d \mid S, t) P(t \mid \boldsymbol{\tau_0})} + O(1) \tag{7.20}$$

$$\log P(D \mid S, \boldsymbol{\tau}) \ \approx \ \sum_i \sum_t \frac{P(d_i \mid S, t) P(t \mid \boldsymbol{\tau})}{\sum_t P(d_i \mid S, t_i) P(t \mid \boldsymbol{\tau_0})} + O(1) \,. \tag{7.21}$$

In our experiments we linearize about $\boldsymbol{\tau_0} = (\frac{1}{3}, \frac{1}{3}, \frac{1}{3})$. By defining

$$\Psi_{\mathsf{3D}}(D, S) = \frac{1}{\sum_t P(d_i \mid S, t) P(t \mid \boldsymbol{\tau_0})} \begin{bmatrix} \sum_i P(d_i \mid S, t = \mathsf{IN}) P(t = \mathsf{IN} \mid \boldsymbol{\tau}) \\ \sum_i P(d_i \mid S, t = \mathsf{OUT}) P(t = \mathsf{OUT} \mid \boldsymbol{\tau}) \\ \sum_i P(d_i \mid S, t = \mathsf{ON}) P(t = \mathsf{ON} \mid \boldsymbol{\tau}) \end{bmatrix} . \tag{7.22}$$

we can write

$$\log P(D \mid S, \boldsymbol{\tau}) = \left\langle \boldsymbol{\tau}, \Psi_{\mathsf{3D}}(D, S) \right\rangle \ + O(1) . \tag{7.23}$$

Posterior

We have now shown that the likelihoods we defined in Chapter 6 for each sensor modality are log–linear in the respective hyper–parameters. Combining equations (7.12), (7.15), (7.19), and (7.23) we have the following linear form for the log–posterior,

$$\log P(S \mid X, \boldsymbol{w}) = \left\langle \boldsymbol{w}, \Psi(X, S) \right\rangle \tag{7.24}$$

where X denotes all observations from all sensor modalities and we have defined

$$\boldsymbol{w} = \begin{bmatrix} \boldsymbol{\lambda} \\ \boldsymbol{\omega} \\ \boldsymbol{\sigma} \\ \boldsymbol{\tau} \end{bmatrix} \qquad \Psi(X, S) = \begin{bmatrix} \boldsymbol{n} \\ \Psi_{\mathsf{mono}} \\ \Psi_{\mathsf{stereo}} \\ \Psi_{\mathsf{3D}} \end{bmatrix} . \tag{7.25}$$

Discussion

We have shown in the derivations above that the posterior from Chapter 6 is log–linear (or can be approximated as such), so substituting (7.24) into (7.8) we are now interested in predictors of the form

$$f(\Phi) = \underset{S}{\operatorname{argmax}} \left\langle \boldsymbol{w}, \Psi(X, S) \right\rangle . \tag{7.26}$$

Feature	Dimensionality	Multi–view?	Single–view?	Reference
Stereo photo–consistency	4	yes	no	
Point cloud	2	yes	no	
Line sweeps	1	yes	yes	Lee *et al.* [43]
RGB+HSV	6	no	yes	
Gabor responses[2]	12	no	yes	

Table 7.1: The composition of our single– and multiple–view feature space. We omit colour and Gabor features from the multiple–view feature space for training efficiency.

One view of this result is that it is a convenient property of our chosen likelihoods that allows us to efficiently optimise the hyper–parameters in the graphical models of Chapter 6 using learning algorithm that we describe below. However, an alternative view is that the joint feature map is simply an arbitrary feature space with no special interpretation attached to any element. Each element of the feature space simply expands the range of predictors that can be expressed in the form (7.26), and we may add whichever features we believe will be helpful for reconstruction. The fact that our features are derived from a graphical model is suggestive of their relevance but not absolutely necessary.

Both views lead to the same learning objective, which is to optimise $\boldsymbol{w}$ with respect to an expected loss over a training set.

Features

The precise make–up of the feature space depends on the available sensor modalities. For our experiments we define separate feature spaces for the single– and multiple–view contexts; these are summarised in Figure 7.1.

7.3.3 Loss Functions

In this section we define a loss function $\Delta(S, \hat{S})$ measuring the cost of predicting some reconstruction $\hat{S}$ when in fact the true reconstruction is S. In the context of learning one often faces a trade–off between choosing a loss that leads to tractable optimisation, and choosing a loss

[2] 4 orientations, 3 scales

that measures the quantity that one "really" cares about. For example, Hoiem *et al.* [34] learn a per–segment orientation classifier, then pass this as input to a separate 3D reconstruction system [33]. However, what one "really" cares about is some loss defined on the output of the entire system rather than the output of individual components. This is not a criticism of those authors' choice, but an illustration of the trade–off faced when choosing a loss function. In this chapter we show how to learn efficiently with respect to loss functions defined on the final reconstruction.

The relative depth error has been the gold standard within the reconstruction community for more than a decade [29], and measures the average deviation between reconstructed and ground truth depths. In our notation,

$$\Delta_{\mathsf{depth}}(S, \hat{S}) = \frac{1}{N} \sum_{\boldsymbol{p}} \frac{|d(\boldsymbol{p}; \hat{S}) - d(\boldsymbol{p}; S)|}{d(\boldsymbol{p}; S)} \,, \tag{7.27}$$

where N is the number of pixels. Another reasonable choice is the labelling error, used widely within the semantic segmentation literature,

$$\Delta_{\mathsf{labelling}}(\hat{S}, S) = \frac{1}{N} \sum_{\boldsymbol{p}} \big[\, a(\boldsymbol{p}; \hat{S}) \neq a(\boldsymbol{p}; S) \,\big] \,, \tag{7.28}$$

where $[p]$ is 1 if p is true and 0 otherwise. An attractive characteristic of the indoor Manhattan class is that *both of these losses can be optimised exactly*. The algorithmic details are left to Section 7.4; the key result we establish here is that Δ_{depth} and $\Delta_{\mathsf{labelling}}$ can be written in a form resembling the payoff formulation (6.1) for the feature likelihoods.

First we invoke the independence between columns established in Section 4.5.4:

$$\Delta_{\mathsf{depth}}(\hat{S}, S) = \frac{1}{N} \sum_{x=1}^{W} \sum_{y=1}^{H} \frac{|\tilde{d}(x, y; \hat{s}_x) - d(x, y; S)|}{d(x, y; S)} \,. \tag{7.29}$$

Defining a real matrix δ_S,

$$\delta_S(x, j) = \frac{1}{N} \sum_{y=1}^{H} \frac{|\tilde{d}(x, y; j) - d(x, y; S)|}{d(x, y; S)} \,, \tag{7.30}$$

we see that we can write Δ_{depth} in the form

$$\Delta_{\mathsf{depth}}(\hat{S}, S) = \sum_{x=1}^{W} \delta_S(x, \hat{s}_x) \; . \tag{7.31}$$

There is a similar form for $\Delta_{\mathsf{labelling}}$, which we omit here because it follows almost identically to the derivations above.

Choosing a Loss Function

Neither of the above losses (relative depth or labelling error) is unequivocally the "correct" loss; the choice will depend on the application at hand. One might expect a strong correlation between the losses, and indeed one can show analytically that

$$\Delta_{\mathsf{depth}}(\hat{S}, S) = 0 \iff \Delta_{\mathsf{labelling}}(\hat{S}, S) = 0 \; . \tag{7.32}$$

However, in our experiments we found only a weak correlation between these losses away from the origin. For example, the scatter plot shown in figure Figure 7.1 shows a significant number of outliers that score very well on Δ_{depth} but poorly on $\Delta_{\mathsf{labelling}}$, and vice versa. This underscores the importance of choosing a loss function suitable for the problem at hand, and highlights the advantages of a learning scheme that can incorporate widely–used loss functions such as the two discussed above.

7.4 Learning Algorithm

We turn now to the problem of learning within the model described above. Our learning task is to identify a prediction function f mapping observed features Φ to reconstructions S. We seek the loss minimiser

$$f^* = \operatorname*{argmin}_f \mathbb{E}\Big[\Delta\big(f(\Phi), S\big)\Big] \; , \tag{7.33}$$

which we approximate in the framework of structural risk minimisation as

$$f^* = \operatorname*{argmin}_f \mathcal{R}(f) + \sum_k \Delta\big(f(\Phi_k), S_k\big) \;, \tag{7.34}$$

where k indexes a training set and $\mathcal{R}$ is a regulariser. To perform this optimisation we turn to the tools of structured prediction [2], and in particular the structured SVM [68]. Following [68] we cast the learning problem as a constrained optimisation problem,

$$\begin{aligned} &\min_{\boldsymbol{w},\boldsymbol{\xi}} \;\; \frac{1}{2}\|\boldsymbol{w}\|^2 + C\sum_{k=1}^{n}\xi_k \\ &s.t. \;\; \forall k, S \neq S_k : \; \big\langle \boldsymbol{w}, \Psi(\Phi_k, S_k)\big\rangle - \big\langle \boldsymbol{w}, \Psi(\Phi_k, S)\big\rangle \geq \Delta(S, S_k) - \xi_k \;. \end{aligned} \tag{7.35}$$

where C is a user–specified parameter that trades off between prediction accuracy and model complexity. Tsochantaridis *et al.* [68] described an algorithm for solving this minimisation that is now used extensively within machine learning and computer vision. To apply this algorithm here we must solve two inference problems:

1. *Prediction.* This is the maximisation described in (7.26).

2. *Separation.* The algorithm described in [68] requires a user–supplied procedure to find the "most–violated constraint" at each iteration. That is,

$$\operatorname*{argmax}_S \big\langle \boldsymbol{w}, \Psi(\Phi_k, S)\big\rangle + \Delta(S, S_k) \;. \tag{7.36}$$

Our solutions to both of the above build on the dynamic programming algorithm presented in Chapter 6, which solves problems of the form

$$\operatorname*{argmax}_S \sum_x \pi(x, s_x) - \sum_j \gamma(j; S) \;. \tag{7.37}$$

7.4.1 Inference (Prediction)

We showed in Section 7.3 that (7.37) can be written in the form (7.26), so the prediction problem is a straightforward application of the inference algorithm of Chapter 6. This is as expected since, as we have already remarked, (7.26) is equivalent to MAP inference on indoor Manhattan reconstructions, which was precisely the subject of Chapter 6.

7.4.2 Loss–Augmented Inference (Separation)

The separation problem can also be solved using the dynamic programming algorithm from Chapter 6, as the following proposition shows.

Proposition 1. *Let (Φ_k, S_k) be a training instance with payoff matrices $\{\pi_i\}$ as defined in Chapter 6. Let*

$$\pi_{\mathsf{aug}} = \delta_{S_k} + \sum_i \pi_i \,. \tag{7.38}$$

Then the solution to (7.37) *with $\pi = \pi_{\mathsf{aug}}$ is identical to the solution to* (7.36)*.*

Proof. Direct equivalence of the expressions to be maximised. First substitute (7.24) and (7.31) into (7.36):

$$\log P(S \mid \Phi) + \sum_{x=1}^{W} \delta_{S_k}(x, s_x) \tag{7.39}$$

Further substituting (6.45) and defining γ as in Chapter 6 gives

$$\sum_i \sum_{x=1}^{W} \pi_i(x, s_x) - \sum_j \gamma(j; S) + \sum_{x=1}^{W} \delta_{S_k}(x, s_x) \,. \tag{7.40}$$

Finally we see that substituting (7.38) gives

$$\sum_{x=1}^{W} \pi_{\mathsf{aug}}(x, s_x) - \sum_j \gamma(j; S) \,. \tag{7.41}$$

which is precisely (7.37) under the desired substitution $\pi = \pi_{\mathsf{aug}}$. □

7.5 Multiple View Results

We evaluated our approach on the same data–set used in Chapter 6, which consists of 18 sequences of six environments averaging 59 seconds in duration. We sampled key–frames at regular intervals. Each "instance" in our training and hold–out sets consists of one base frame together with four auxiliary frames.

Ground truth for this dataset was acquired by reconstructing the camera trajectory using a SLAM system (we worked with PTAM [40]). This system is designed for real–time operation and as such its reconstructs are not always perfect, so some errors in the training set arise from errors in the underlying structure from motion system. Furthermore, some environments in our dataset are not ideal indoor Manhattan scenes, and so there is some ambiguity in how we should construct the ground–truth floorplans. For example, there is a stairwell at the end of one sequence, which is shown near the bottom of Table 7.3. It is hard to define any sensible indoor Manhattan model for this environment, but rather than eliminating it from the dataset, we leave it in to understand the performance of our system in adverse conditions.

We compared with the bootstrapping approach described in [24] and outlined in the preceding chapter. Our metrics differ from those of the previous chapter in two ways. Firstly, the previous chapter computed relative depth error using the maximum of the ground truth and estimated depths in the denominator, whereas we always use the ground truth in the denominator. These metrics are separated by at most a monotonic transform but we must use the latter here in order to represent the loss function in the form (7.31). Secondly, when we compute labelling error we differentiate vertical and horizontal surfaces only, whereas the previous chapter also differentiate the two vertical orientations. The latter approach makes a side–by–side comparison difficult because the two vertical orientations are symmetric and their labels can always be interchanged.

We described two loss functions above: the relative depth error and the labelling error. We also described two feature spaces: one containing exclusively single view features and one containing multiple view features. In total we trained four predictors, corresponding to all

combinations of feature spaces and loss functions. For clarity we will use the following notation throughout this section.

$f^{\text{sview}}_{\text{depth}}$	Trained with respect to Δ_{depth} in the single view feature space
$f^{\text{sview}}_{\text{labelling}}$	Trained with respect to $\Delta_{\text{labelling}}$ in the single view feature space
$f^{\text{mview}}_{\text{depth}}$	Trained with respect to Δ_{depth} in the multiple view feature space
$f^{\text{mview}}_{\text{labelling}}$	Trained with respect to $\Delta_{\text{labelling}}$ in the multiple view feature space

The performance of all predictors are summarised in Table 7.2. Our approach significantly out–performs the approach of the previous chapter. Anecdotally we noticed that much of the improvement resulted from a reduction in catastrophic failures. This makes sense because we would expect the learning algorithm to concentrate on reducing those mistakes that result in the largest loss. Some example predictions in the multiple–view feature space are shown in Figure 7.6.

Figure 7.2 shows the evolution of the weight vector $\boldsymbol{w}$ during training for each of the four predictors. The primary conclusion to draw from this figure is that the weights do in fact converge, and that the single–view scenario is, as expected, the more difficult learning problem. Finally, Figure 7.1 compares the error distribution on two error metrics for the two multiple–view predictors. The fact that the distributions are skewed along opposite axes shows that training with respect to different loss functions has indeed resulted in different prediction rules, which correctly minimise their respective losses on held–out instances.

7.6 Single View Results

We evaluated our system for single–view reconstruction using the same data–set described in the previous section. We used the single–view features summarised in Figure 7.1. We compared

[1]This column corresponds to using all sensor modalities
[2]This column corresponds to using photometric features alone

	Multiple–view			Single–view		
Sequence	$f^{\text{mview}}_{\text{depth}}$	$f^{\text{mview}}_{\text{labelling}}$	Chapter 6[1]	$f^{\text{sview}}_{\text{depth}}$	$f^{\text{sview}}_{\text{labelling}}$	Chapter 6[2]
ground	4.9	5.5	24.5	17.3	28.0	66.6
foyer1	6.1	4.5	31.0	25.1	29.2	6.6
foyer2	4.3	4.9	30.1	29.1	28.5	5.4
corridor	14.6	15.0	33.6	31.7	32.7	52.9
mcr	34.0	37.3	45.9	70.1	58.6	67.6
kitchen	16.8	19.3	26.2	25.1	25.8	23.6
Average	**13.4**	14.4	31.9	33.1	33.8	37.1

(a) Relative depth error

	Multiple–view			Single–view		
Sequence	$f^{\text{mview}}_{\text{depth}}$	$f^{\text{mview}}_{\text{labelling}}$	Chapter 6[1]	$f^{\text{sview}}_{\text{depth}}$	$f^{\text{sview}}_{\text{labelling}}$	Chapter 6[2]
ground	2.8	2.9	10.4	14.8	7.8	12.4
foyer1	3.6	3.1	3.1	20.3	15.1	22.2
foyer2	3.3	3.7	4.0	18.6	15.9	18.6
corridor	11.4	9.5	19.2	23.7	19.3	24.8
mcr	15.4	15.8	16.2	24.5	26.7	20.8
kitchen	5.3	5.2	6.1	11.0	7.7	11.9
Average	7.0	**6.7**	9.8	18.8	15.4	18.4

(b) Labelling error

Table 7.2: Performance for each predictor, for each sequence, and for each error metric. The six predictors under comparison are listed in the top row of each table — see the main text for details on these symbols. Note that even when a predictor is trained with respect to a particular loss function, we may still evaluate it with respect to a different metric (though as expected the predictors perform best when evaluated by the same error metric that they were trained for).

our approach to the single–view approach described in the previous chapter and in [21], which uses only line–sweep features.

Performance for each algorithm is summarised in Table 7.2. When measured by labelling error, our approach out–performs the comparison system, but on the depth error metric our approach is inferior. While investigating this result we found that our learning algorithm assigns small weights to all but the line–sweep features, which are the same features used by the single–view–only instantiation of Chapter 6. This suggests that the hand–tuned weights are in fact close to optimal within this feature space, though one would expect that with additional feature engineering our learning algorithm would be able to leverage more salient information and

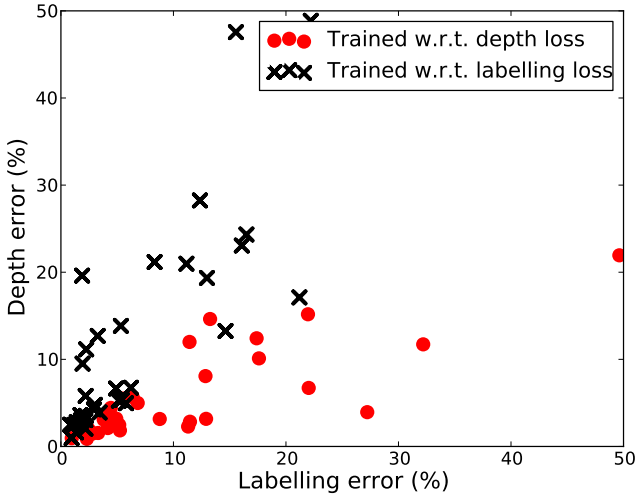

Figure 7.1: The effect of the loss function on training. We train two predictors, one with respect to Δ_{depth} and one with respect to $\Delta_{\text{labelling}}$, then evaluate both on all held–out instances. Each data point shows the error obtained by one predictor on one held–out instance. The differing distribution of errors shows that the two predictors trade off errors as expected.

reduce the error rate further.

The evolution of the weight vector $\boldsymbol{w}$ over the course of training is shown in Figure 7.2. Due to the size of the single view feature space we show selected features only. The single view learning problem is, as expected, the more difficult problem, as shown by the considerably longer training times and the higher volatility during the exploration phase.

Table 7.3: Reconstructions predicted by our system using the multiple view feature space; comparison with the bootstrapping approach described in Chapter 6 and in [24]. The first two columns correspond to the predictors trained on Δ_{depth} and $\Delta_{\text{labelling}}$ respectively, the third column is from Chapter 6, and the fourth column is ground truth. This figure shows samples from the hold–out set, and were selected uniformly at random for inclusion here.

$f^{\text{mview}}_{\text{depth}}$	$f^{\text{mview}}_{\text{depth}}$	Chapter 6	Ground Truth
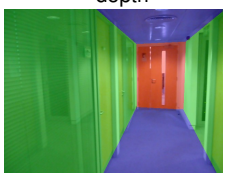	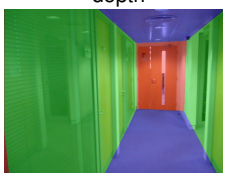		

Continued on next page

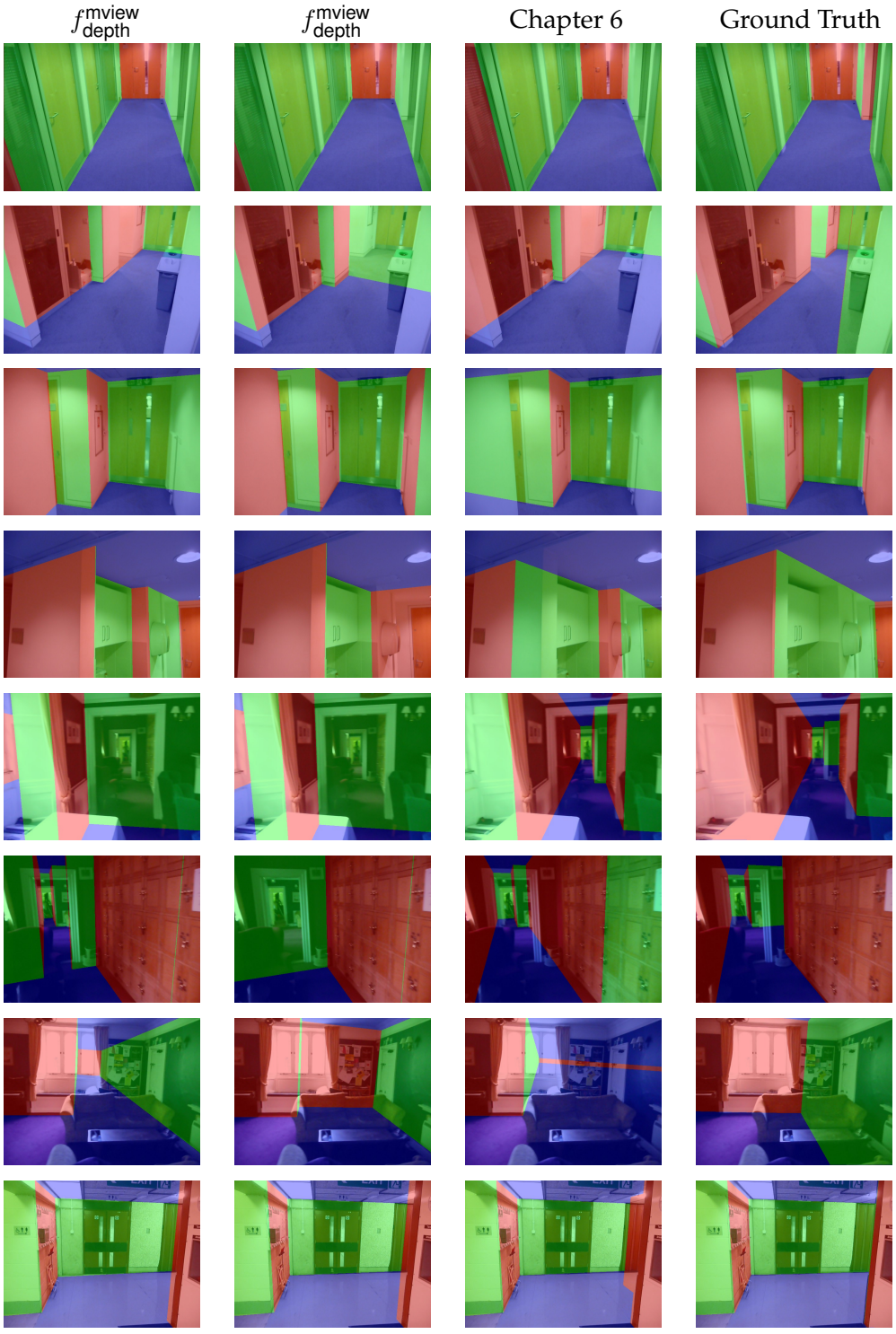

Continued on next page

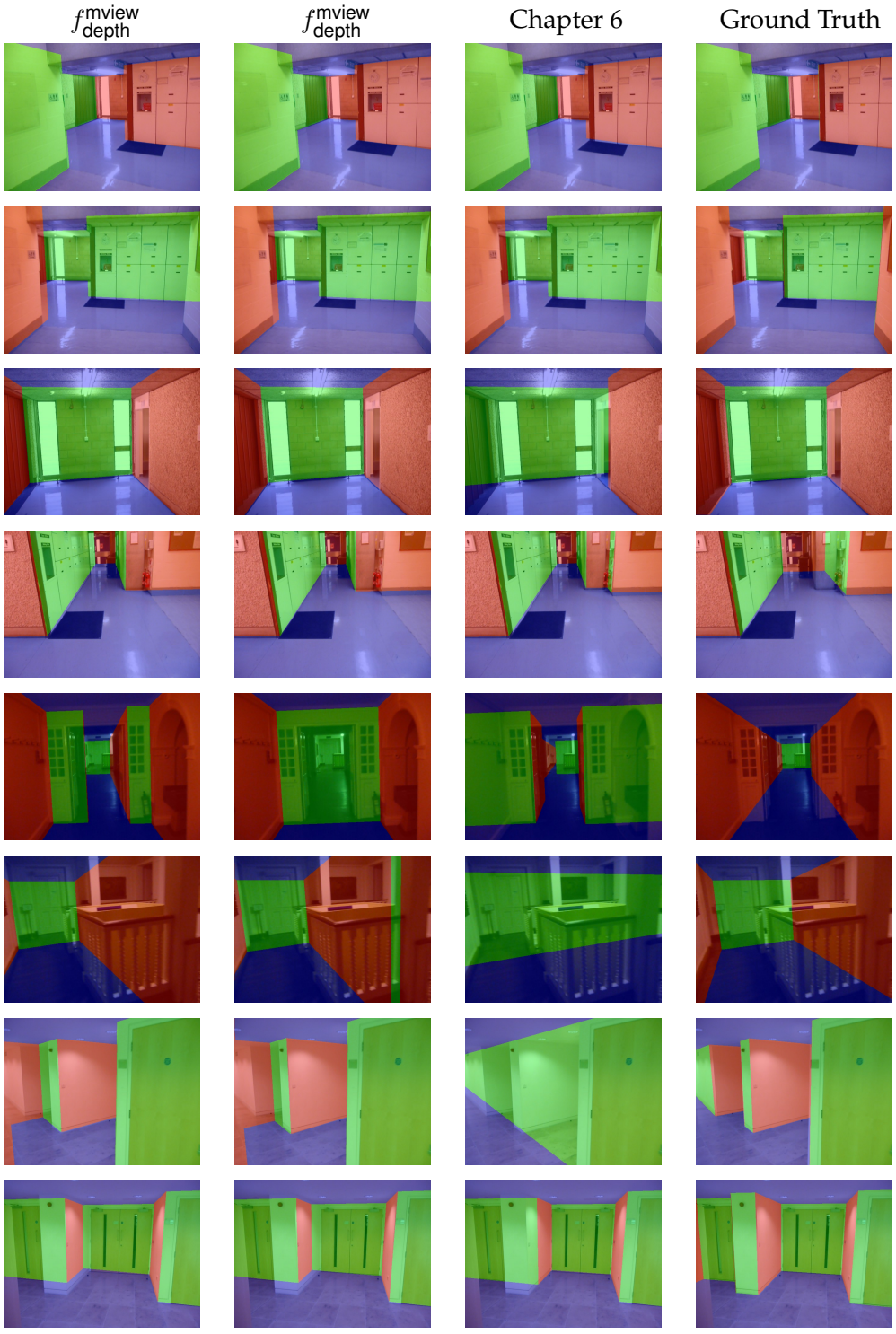
$f^{\text{mview}}_{\text{depth}}$
$f^{\text{mview}}_{\text{depth}}$
Chapter 6
Ground Truth

Table 7.4: Reconstructions predicted by our system using the single view feature space; comparison with the bootstrapping approach described in Chapter 6 and in [24]. The first two columns correspond to the predictors trained on Δ_{depth} and $\Delta_{\text{labelling}}$ respectively, the third column is from Chapter 6 using photometric features alone, and the fourth column is ground truth. This figure shows samples from the hold–out set, and were selected uniformly at random for inclusion here.

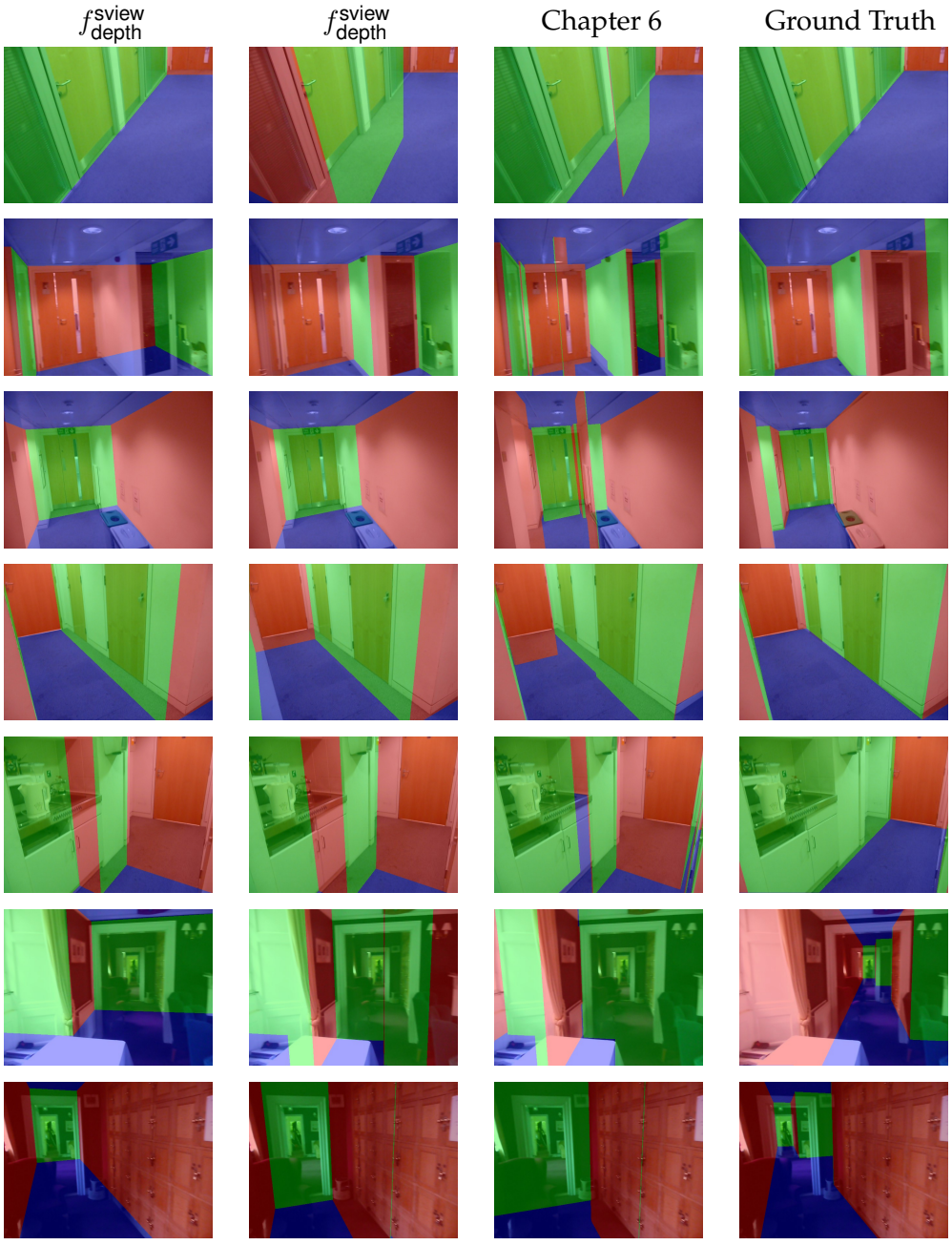

Continued on next page

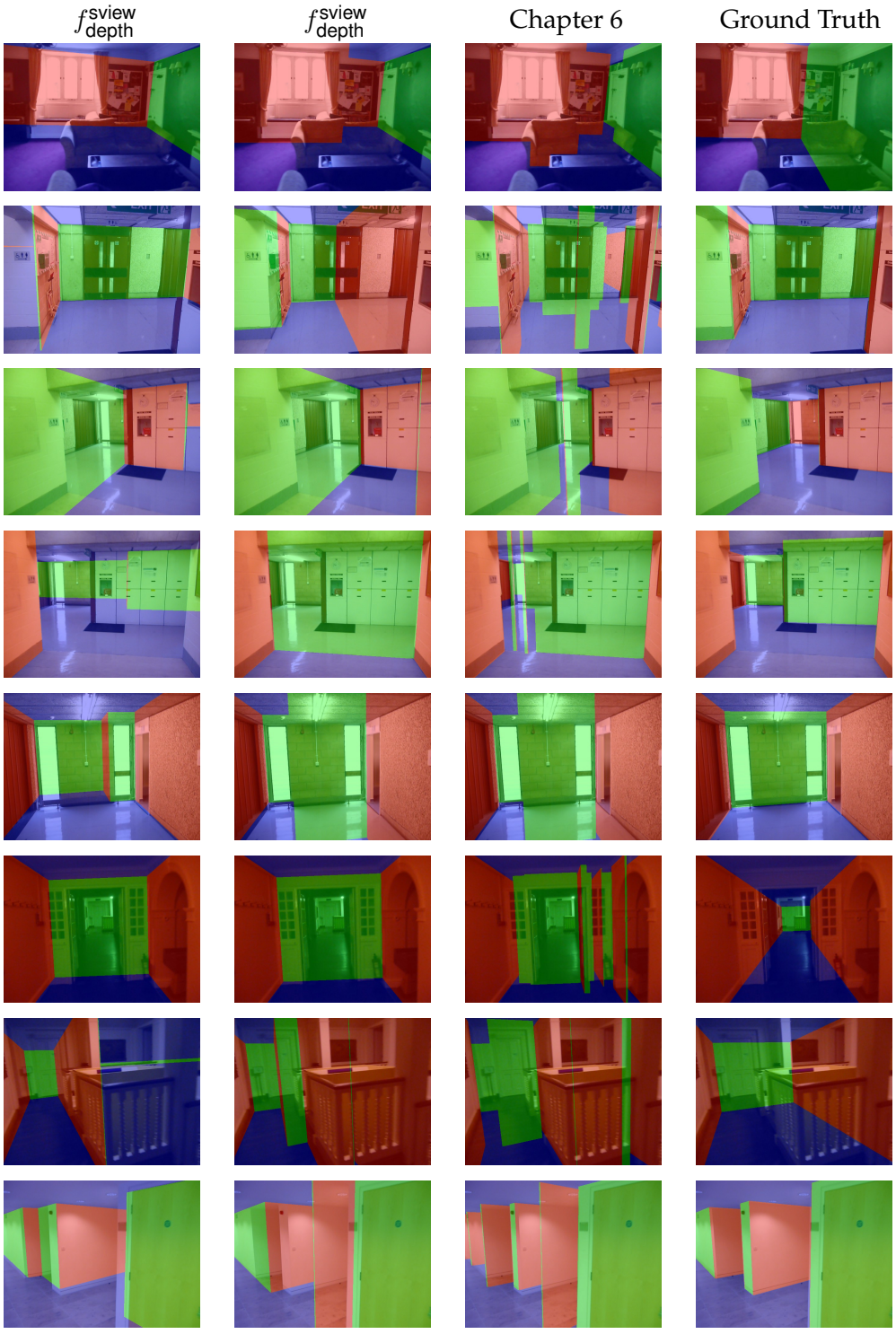

Continued on next page

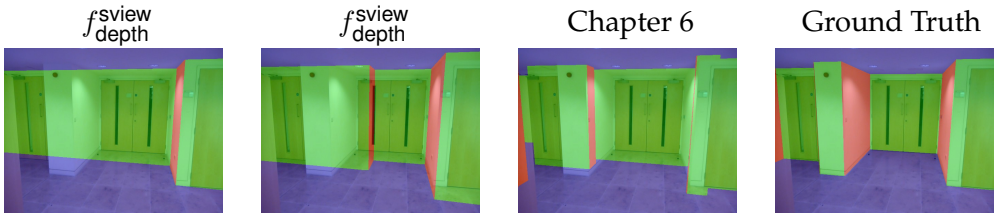

7.7 Discussion

The hypothesis class considered in this chapter is amongst the most complex (in terms of internal constraints on the output space) studied within the structured prediction framework. In this section we turn to some practical lessons learned that may be of value to other practitioners.

7.7.1 Condition in the joint feature space, not the input feature space.

A common pre–processing operation for statistical learning is to transform the observed features Φ to zero mean and unit variance. However, for structured prediction tasks it is the joint feature space Ψ, not the input feature space, that should be conditioned:

$$\Psi' = \frac{\Psi - \mu}{\sigma^2} \,. \tag{7.42}$$

Ideally one would sample directly from the joint feature space to determine the conditioning transformation, but the distribution of inputs and outputs is generally unknown in an empirical risk minimisation setting. Instead, we suggest using the training set as a proxy. We compute the empirical mean and variance of $\{\Psi(\Phi_k, S_k)\}_{k=1}^n$ for the training set at the outset, then apply the transformation (7.42) after each feature computation.

7.7.2 Condition the loss terms.

For any $\eta > 0$, the minimisation problem (7.35) is equivalent to the following (this is proved in Proposition 2 at the end of this chapter):

$$\begin{aligned} &\min_{\boldsymbol{w}', \boldsymbol{\xi}'} \ \frac{1}{2}\|\boldsymbol{w}'\|^2 + \eta C \sum_{k=1}^{n} \xi'_k \\ &s.t. \ \forall k, S \neq S_k : \ \left\langle \boldsymbol{w}', \Psi(\Phi_k, S_k) \right\rangle - \left\langle \boldsymbol{w}', \Psi(\Phi_k, S) \right\rangle \geq \eta \Delta(S, S_k) - \xi'_k \ . \end{aligned} \tag{7.43}$$

Although any $\eta > 0$ preserves the correctness of the optimisation algorithm, we found that choosing $\eta = \text{Var}(\Delta)$ improved numerical stability, since this means that the loss terms will have roughly unit variance. Unfortunately, we cannot use the training set to estimate $\text{Var}(\Delta)$ since the loss for the ground truth output is always zero. Instead we computed $\Delta(\Phi_k, S_j)$ for each $k \neq j$ in the training set. This is not an ideal estimate, but we found that it worked well in practice.

7.7.3 Check that the hypothesis class contains the ground truth.

The algorithm described in [68] implicitly assumes that the hypothesis class $\mathcal{Y}$ contains the ground truth labels S_k. This means that if S^+ is the maximiser of (7.36) then

$$\left\langle \boldsymbol{w}, \Psi(\Phi_k, S_k) \right\rangle - \left\langle \boldsymbol{w}, \Psi(\Phi_k, S^+) \right\rangle - \Delta(S^+, S_k) \leq 0 \ , \tag{7.44}$$

since otherwise we would have

$$\left\langle \boldsymbol{w}, \Psi(\Phi_k, S_k) \right\rangle + \Delta(S_k, S_k) > \left\langle \boldsymbol{w}, \Psi(\Phi_k, S^+) \right\rangle + \Delta(S^+, S_k) \ , \tag{7.45}$$

contradicting S^+ as the maximiser of (7.36). However, our output space contains fundamentally real–valued quantities such as polygon vertices, which are recovered only to some finite precision by the inference algorithm, and since our ground truth labels were acquired by manual labelling, they sometimes exceed the maximum precision of the inference algorithm. In this

case we effectively have $S_k \notin \mathcal{Y}$ (although there is always some $S' \in \mathcal{Y}$ close to S_k), so it is possible that S^+ violates (7.44). Our workaround here is simply to check the condition (7.44) each time we solve the separation problem and, if violated, substitute S_k for S^+. This is justified by the observation that if (7.44) is violated for S^+ then it is violated for all $S \in \mathcal{Y}$. One could think of this as learning with respect to the hypothesis class $\mathcal{Y} \cup \{S_k\}$ but evaluating with respect to $\mathcal{Y}$. Again, this is not an ideal solution but we found it to work well in practice.

7.7.4 Equivalence of (7.35) and (7.43)

Here we prove the equivalence of the minimisation problems (7.35) and (7.43) stated above. For clarity we re–state the claim in the following proposition.

Proposition 2. *Let $\boldsymbol{w}, \boldsymbol{\xi}$ be the solution to*

$$\begin{aligned} &\min_{\boldsymbol{w},\boldsymbol{\xi}} \ \frac{1}{2}\|\boldsymbol{w}\|^2 + C\sum_{k=1}^{n} \xi_k \\ &s.t. \ \forall k, S \neq S_k : \ \big\langle \boldsymbol{w}, \Psi(\Phi_k, S_k)\big\rangle - \big\langle \boldsymbol{w}, \Psi(\Phi_k, S)\big\rangle \geq \Delta(S, S_k) - \xi_k \ . \end{aligned} \tag{7.46}$$

Let $\boldsymbol{w}', \boldsymbol{\xi}'$ be the solution to

$$\begin{aligned} &\min_{\boldsymbol{w}',\boldsymbol{\xi}'} \ \frac{1}{2}\|\boldsymbol{w}'\|^2 + \eta C\sum_{k=1}^{n} \xi'_k \\ &s.t. \ \forall k, S \neq S_k : \ \big\langle \boldsymbol{w}', \Psi(\Phi_k, S_k)\big\rangle - \big\langle \boldsymbol{w}', \Psi(\Phi_k, S)\big\rangle \geq \eta\Delta(S, S_k) - \xi'_k \ . \end{aligned} \tag{7.47}$$

Then

$$\boldsymbol{w}' = \eta\boldsymbol{w} \tag{7.48}$$

$$\boldsymbol{\xi}' = \eta\boldsymbol{\xi} \ . \tag{7.49}$$

Proof. Substituting for $\boldsymbol{w}'$ and $\boldsymbol{\xi}'$ in (7.47),

$$\begin{aligned} &\min_{\boldsymbol{w},\boldsymbol{\xi}} \ \frac{1}{2}\|\eta\boldsymbol{w}\|^2 + \eta C \sum_{k=1}^{n} \eta\xi_k \\ &s.t. \ \forall k, S \neq S_k : \ \left\langle \eta\boldsymbol{w}, \Psi(\Phi_k, S_k) \right\rangle - \left\langle \eta\boldsymbol{w}, \Psi(\Phi_k, S) \right\rangle \geq \eta\Delta(S, S_k) - \eta\xi_k \end{aligned} \tag{7.50}$$

and dividing the objective by η^2 and the constraints by η we obtain the desired result. □

7.8 Conclusion

We have presented a unified learning framework for recovering semantically meaningful geometric models from single and multiple views of a scene. We have chosen to work with the indoor Manhattan class in order to leverage the simple parametrisation and efficient inference algorithm made possible by this hypothesis class. Our approach to learning performs a single optimisation with respect to a clearly defined loss function. Experiments show our system out–performing the approach of the previous chapter in the multiple–view setting (by a large margin) and on one metric in the single–view setting.

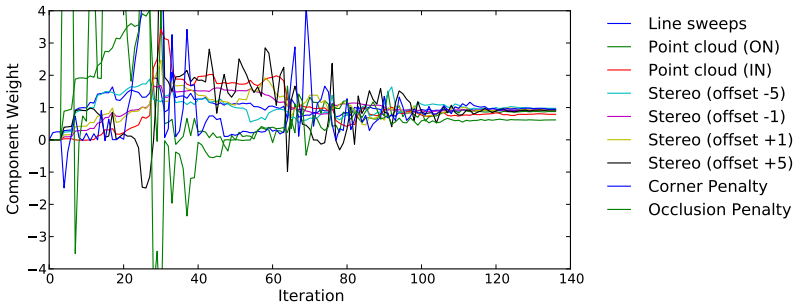

(a) Evolution of $f^{\text{mview}}_{\text{depth}}$ during training

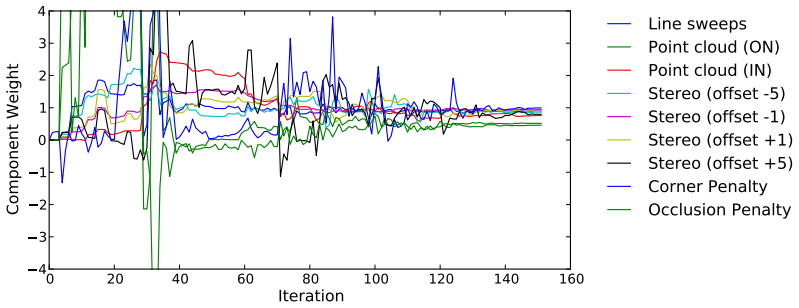

(b) Evolution of $f^{\text{mview}}_{\text{labelling}}$ during training

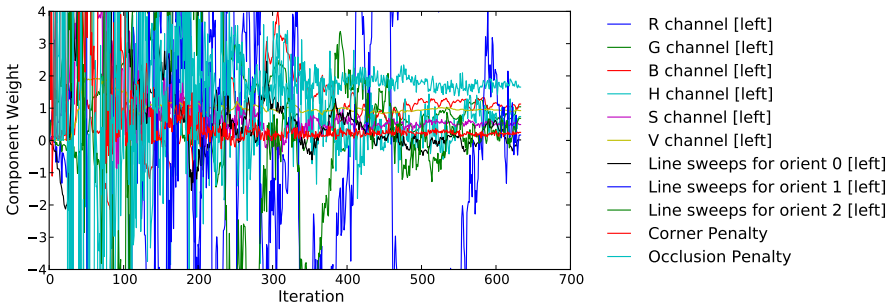

(c) Evolution of $f^{\text{sview}}_{\text{depth}}$ during training (selected features only)

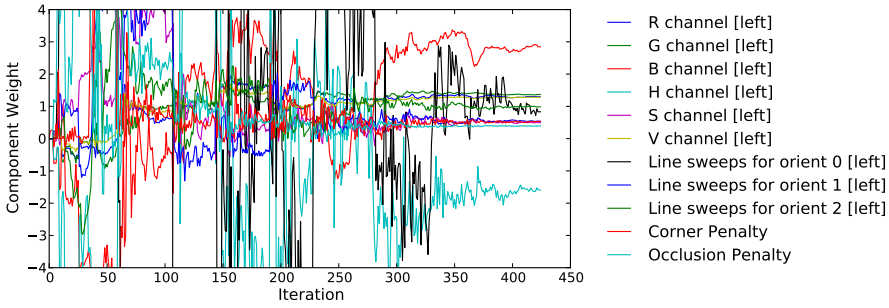

(d) Evolution of $f^{\text{sview}}_{\text{labelling}}$ during training (selected features only)

Figure 7.2: Evolution of model weights $\boldsymbol{w}$ during training of each predictor. See main text for description of the four predictors we trained.

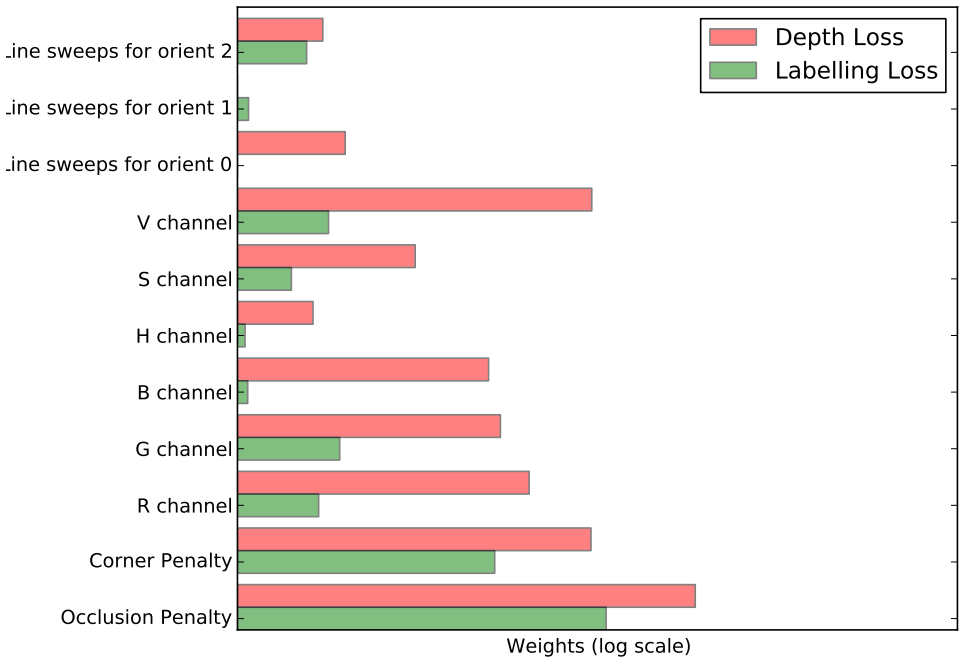

(a) Weight vector learned for single view features

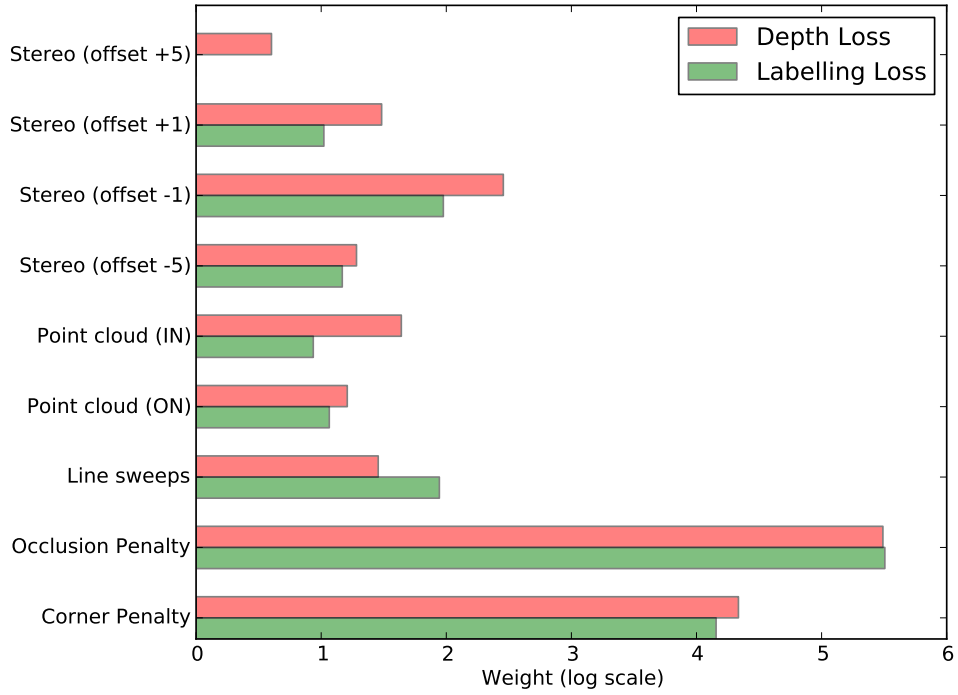

(b) Weight vector learned for multiple view features

Figure 7.3: Final weight vector that was learned for the single– and multiple–view feature spaces. The two figures each show the weights learned when minimizing the labelling loss and when minimising the depth loss.

8

Conclusion

In this thesis we have presented ideas for inference of high–level scene structure in the context of a moving observer. Drawing inspiration from scene understanding ideas that have traditionally been the purview of single–view computer vision, we have demonstrated a number of promising approaches towards multiple–view scene understanding. In this concluding chapter we will briefly review the key results and present ideas for future work.

8.1 Key Results

Chapter 3 presented textons as a simple and flexible basis for inferring contextual variables such as scene categories. Building on ideas from texture analysis, we presented a probabilistic model and accompanying inference procedure, and evaluated our approach on two classification problems. In both cases our system out–performed the Gist descriptor of Torralba *et al.*.

In Chapter 4 we gave a formal account of the indoor Manhattan model — the first comprehensive analysis that we are aware of in the literature (though not the first description *per se*). This chapter did not present any empirical results; its primary contribution was the development of the "vertex" and "seam" representations, and the decomposability property of indoor

Manhattan scenes.

Next we discussed recovery of the Manhattan world's orientation with respect to a camera, given multiple calibrated views of a scene. We showed that reasoning from photometric information rather than geometric information, and integrating multiple images into a joint optimisation improved substantially upon existing approaches. Our algorithm built upon ideas from single–view vanishing point estimation; our contribution was in showing how to extend this to multiple calibrated views.

Chapter 6 focussed on inferring indoor Manhattan scene structure from single and multiple views of a scene. We presented a probabilistic model relating Manhattan scene structure to three sensor modalities, and showed that the likelihoods for all three sensor modalities can be written in terms of payoff functions. Beyond the specific model that we proposed, this approach suggests a general strategy by which further sensor modalities can be integrated with our model without modifying the inference algorithm. The other contribution of this chapter was the dynamic programming algorithm to solve the payoff optimisation problem. We showed that a decomposition into sub–problems permitted an efficient and exact solution to both MAP and ML inference. Experiments in this chapter showed our system substantially out–performing two other systems.

Finally, Chapter 7 described an approach to learning indoor Manhattan models from training examples. We described a structured prediction learning algorithm for the indoor Manhattan hypothesis class, and showed that the two required inference problems were solvable by the dynamic programming algorithm of Chapter 6. Among learning approaches to geometric scene context, our contribution is among a small number that implement a single optimisation with respect to a clearly defined loss function. We showed a clear improvement over the system proposed in Chapter 6.

A theme of this thesis has been the use of geometry for scene understanding purposes. We have shown how to extract semantically meaningful scene structure using ideas drawn from both the geometry literature and the scene understanding literature. The ideas from geometry allowed

us to decompose our reconstructions into a representation amenable to dynamic programming, and the ideas from single–view scene understanding allowed us to connect our hypothesis class to observed image features.

8.2 Future Work

In this section we discuss directions for future work.

8.2.1 Applications of Indoor Manhattan Models

Perhaps the clearest direction for future work is to apply the indoor Manhattan model to the semantic inference tasks for which it was originally designed, namely scene category recognition and contextual object detection.

Scene category recognition is the problem of classifying scenes into categories such as "bedroom", "bathroom", or "office". There is a significant literature on this problem for the single–view case (as reviewed in Chapter 2), but little effort has been directed at leveraging multiple–view geometry to this end. Since humans greatly out–perform computers at this task, and humans appear to use various notions of geometry to achieve their high performance, the use of geometry for scene categorisation appears to be a particularly compelling direction for future work.

Indoor Manhattan models could be leveraged for scene categorisation in a number of ways. At the simplest level, one could recover an indoor Manhattan representation for a query scene and compute a series of geometric features to capture the shape of the scene (ratios of length, breadth, and height, for example) and the position of the camera within it. These could be appended to a vector of photometric features (such as the many proposed in the single–view literature), then a classic multiple–label classifier could be trained to distinguish the various categories. A more sophisticated approach might link the recovered geometry with photometric information more closely. A typical photo captured by a camera located close to the ceiling

would be expected to appear different to that of a camera located close to the floor, even within one scene category. Photometric approaches rely on a classifier to learn such variations automatically, but with an indoor Manhattan model at hand one could model such variations explicitly. For example, one could build up separate appearance models of the floor, wall, and ceilings, using known scene geometry and camera position. Finally, the possibility exists of improving upon simple Markovian models to integrate information over time. A system that recognises when the camera moves between rooms (such as by identifying doorways) could segment a video sequence according to which frames are situated in which rooms. Such a system could perform data association between observations and room categories much more accurately than under a hidden Markov model with a homogeneous transition function such as that used in [67].

The second application to which we intend to apply indoor Manhattan models is object recognition. Contextual information appears to greatly improve object recognition (see Chapter 2 for a review), and the prospect of leveraging the high–level geometric information captured by the indoor Manhattan for this purpose seems promising. A simple approach would be to append geometric features derived from the recovered indoor Manhattan model to traditional appearance features. These geometric features might include the distance of the object from the floor plane (as a percentage of the distance from floor to ceiling), the distance from the closest wall, shape features of the environment, and so on. However, once again the possibility exists of using Manhattan geometry in a more sophisticated way. For example, one could integrate observations from different viewpoints to improve the estimate of an object's identity. The floorplan provided by an indoor Manhattan model could provide a natural basis for integrating such observations.

Several robotics applications may also benefit from the ability to recover Manhattan structure. Path planning requires knowledge of "traversable" surfaces in the environment as well as boundaries that will obstruct movement. The floorplan provided by an indoor Manhattan model seems a natural representation of such information. One might divide the floor plane into a series of cells and separately estimate traversability of each. The occupancy grid estima-

tion might benefit substantially from knowing the shape of the environment about each cell.

A related to path planning is the problem of *active exploration*, in which an agent must plan a path to find an object or location of interest as quickly as possible. Typically this problem is approached from the perspective of information gain rather than shortest path. One might use Manhattan models as a basis for active exploration by reasoning explicitly in terms of rooms and corridors. For example, if a robot seeking a teapot recognises that it is in a bathroom then it could move to a different room immediately, not bothering to continue searching the current environment.

8.2.2 Relaxing Geometric Constraints

A common criticism levelled against indoor Manhattan models is the strong geometric constraints that one must make. We have argued that even in their present form, indoor Manhattan models are surprisingly versatile. Nevertheless, there are several promising approaches to relaxing these assumptions. The difficulty, of course, is finding relaxations that retain the fast inference algorithm of Chapter 6, which is based on the left–to–right decomposability of indoor Manhattan models.

A first relaxation is to permit walls oriented in more than two directions. This could be accomplished by identifying vanishing points on the horizon line corresponding to additional wall orientations, then extending the domain of the orientation variable in the inference algorithm to account for these. These vanishing points could be found either by clustering lines with respect to their intersection at the horizon, or by modifying the rotation estimation algorithm to jointly estimate these wall orientations together with the scene orientation.

A second relaxation would be to permit walls that do not project to straight lines on the floor plane. Zeisl *et al.* [75] show one way to accomplish this: by parametrising walls in pixel coordinates and penalising smoothness in the transition matrix between successive columns. A different approach would be to permit parametric curves so that pillars and circular wall segments could be represented. This could be accomplished without expanding the state–space of

the dynamic programming algorithm at all; it would simply entail integrating the parametric family into the maximisation for each sub–problem.

Another promising direction for relaxation would be to target outdoor areas by removing the assumption of a fixed ceiling plane. Many built–up areas could be represented by a horizontal ground plane and series of vertical facades. The key difference between indoor environments is that building facades typically have varying height. By adding a height parameter to the state space one could jointly estimate the orientation and height of each facade using only a slight modification to the algorithm presented in Chapter 6.

8.2.3 Extensions Of The Probabilistic Model

In addition to the geometric extensions suggested above, there are several promising ways in which the probabilistic models underlying Manhattan structure recovery could be extended. In Chapter 7 we considered learning from labelled examples, but other types of background information could also be helpful for fixing parameters. For example, a database of architectural floorplans could be leveraged to learn about the architectures an agent is most likely to encounter, and hence to form a more accurate prior over building structures. This would require a Bayesian model connecting architectural floorplans to our prior over building structures

In a different direction, one might consider *marginalizing* over indoor Manhattan reconstructions for certain purposes rather than just using a single MAP estimate. That is, for the purpose of, say, scene categorisation or object search, we would consider *all* possible indoor Manhattan reconstructions and their implications for the task at hand, weighted by their plausibility under the model presented in Chapter 6. In this case we would see the reconstruction as a latent variable. In many cases such a marginalisation is intractable, but in the case of indoor Manhattan models there is a promising approach by which the decomposition of Chapter 6 might be leveraged to perform exact marginalisation for a large family of models.

Finally, there is much room for integrating the estimation of indoor Manhattan models over time. Currently our inference procedure is a batch operation that re–estimates the model from

scratch at each time step. Extending this to a recursive estimation framework would allow us to integrate new information in a more principled way, and avoid discarding the computational effort invested at previous time steps. Recursive state estimators maintain a distribution over an underlying hypothesis class that can be efficiently updated from new evidence. A filter for indoor Manhattan environments might represent hypotheses in the seam representation discussed in chapter Chapter 4 and summarise a distribution over this space using a payoff matrix as discussed in Chapter 6. Updating the payoff matrix over time requires integrating image evidence from new viewpoints, but we have already presented the basic geometry that such updates would require during our discussion of stereo features in Chapter 6. Significant work would be required to deal with the occlusion artefacts that integrating information over long periods would introduce.

8.3 Final Remarks

The meeting between geometric ideas from structure–from–motion and scene understanding ideas from single view computer vision seems to hold promise as an exciting research direction over the coming years. This will be driven as much by the new sensor modalities discussed in the introduction as by the maturity of both existing SLAM systems and scene understanding as separate areas of study. We look forward to seeing this unfold.

Bibliography

[1] A. P. DEMPSTER, N. M. L., AND RUBIN, D. B. Maximum likelihood from incomplete data via the em algorithm. *Journal of the Royal Statistical Society 39*, 1 (1977), 1–38.

[2] BAKIR, G. H., HOFMANN, T., SCHLKOPF, B., SMOLA, A. J., TASKAR, B., AND VISHWANATHAN, S. V. N. *Predicting Structured Data*. MIT Press, 2007.

[3] BARINOVA, O., KONUSHIN, V., YAKUBENKO, A., LEE, K., LIM, H., AND KONUSHIN, A. Fast automatic single-view 3-d reconstruction of urban scenes. In *Proc 10th European Conf on Computer Vision* (2008), pp. 100–113.

[4] BARNARD, S. Interpreting perspective images. *Artificial Intelligence 21*, 4 (Nov. 1983), 435–462.

[5] BAZIN, J., SEO, Y., DEMONCEAUX, C., VASSEUR, P., IKEUCHI, K., KWEON, I., POLLEFEYS, M., ET AL. Globally optimal line clustering and vanishing point estimation in manhattan world. In *IEEE Conf. on Computer Vision and Pattern Recognition* (2012).

[6] BLASCHKO, M., AND LAMPERT, C. Learning to localize objects with structured output regression. *Proc 10th European Conf on Computer Vision* (2008), 2–15.

[7] BROSTOW, G. J., SHOTTON, J., FAUQUEUR, J., AND CIPOLLA, R. Segmentation and recognition using structure from motion point clouds. In *Proc 10th European Conf on Computer Vision* (Berlin, Heidelberg, 2008), Springer-Verlag, pp. 44–57.

[8] BUSCHKA, P., AND SAFFIOTTI, A. A virtual sensor for room detection. In *Proc IEEE/RSJ Conf on Intelligent Robots and Systems, Lausanne, Switzerland, Oct 2-4, 2002* (2002), vol. 1, pp. 637–642 vol.1.

[9] CANNY, J. A Computational Approach to Edge Detection. *IEEE Transactions on Pattern Analysis and Machine Intelligence PAMI-8*, 6 (Nov. 1986), 679–698.

[10] CORNELLS, N., LEIBE, B., CORNELLS, K., AND VAN GOOL, L. 3d city modeling using cognitive loops. In *Proc 3rd Int Symposium on 3D Data Processing, Visualization, and Transmission* (2006), IEEE, pp. 9–16.

[11] CORTES, C., AND VAPNIK, V. Support-vector networks. *Machine Learning 20*, 3 (1995), 273–297.

[12] COUGHLAN, J., AND YUILLE, A. Manhattan world: compass direction from a single image by bayesian inference. In *Proc 18th IEEE Conf on Computer Vision and Pattern Recognition* (1999), vol. 2, pp. 941–947.

[13] CRIMINISI, A. *Accurate visual metrology from single and multiple uncalibrated images*. Springer-Verlag New York, Inc., New York, NY, USA, 2001.

[14] CUMMINS, M., AND NEWMAN, P. Fab-map: Probabilistic localization and mapping in the space of appearance. *International Journal of Robotics Research 27*, 6 (2008), 647–665.

[15] DELAGE, E. A dynamic bayesian network model for autonomous 3d reconstruction from a single indoor image. *Proc 24th IEEE Conf on Computer Vision and Pattern Recognition* (2006).

[16] DENIS, P., ELDER, J., AND ESTRADA, F. Efficient edge-based methods for estimating manhattan frames in urban imagery. Springer, pp. 197–210.

[17] EVERINGHAM, M., VAN GOOL, L., WILLIAMS, C. K. I., WINN, J., AND ZISSERMAN, A. The PASCAL Visual Object Classes Challenge 2009 (VOC2009) Results. http://www.pascal-network.org/challenges/VOC/voc2009/workshop/index.html.

[18] FEI-FEI, L. A Bayesian hierarchical model for learning natural scene categories. In *Proc 23rd IEEE Conf on Computer Vision and Pattern Recognition* (2005), pp. 524–531.

[19] FELZENSZWALB, D., AND VEKSLER, O. Tiered scene labeling with dynamic programming. In *Proc 28th IEEE Conf on Computer Vision and Pattern Recognition* (2010).

[20] FELZENSZWALB, P. F., AND HUTTENLOCHER, D. P. Efficient graph-based image segmentation. *International Journal of Computer Vision 59* (2004).

[21] FLINT, A., MEI, C., REID, I., AND MURRAY, D. A dynamic programming approach to reconstructing building interiors. In *Proc 12th European Conf on Computer Vision* (2010).

[22] FLINT, A., MEI, C., REID, I., AND MURRAY, D. Growing semantically meaningful models for visual slam. In *Proc 28th IEEE Conf on Computer Vision and Pattern Recognition* (2010).

[23] FLINT, A., REID, I., AND MURRAY, D. Learning textons for real–time scene context. In *Proc 27th IEEE Conf on Computer Vision and Pattern Recognition* (2009).

[24] FLINT, A., REID, I., AND MURRAY, D. Manhattan scene understanding using monocular, stereo, and 3d features. In *Proc 13th IEEE Int Conf on Computer Vision* (2011).

[25] FORSYTH, D., AND PONCE, J. *Computer vision: A modern approach*. Prentice Hall, 2002.

[26] FURUKAWA, Y., CURLESS, B., SEITZ, S., AND SZELISKI, R. Manhattan–world stereo. *Proc 27th IEEE Conf on Computer Vision and Pattern Recognition*, 1422–1429.

[27] GALLUP, D., FRAHM, J., MORDOHAI, P., YANG, Q., AND POLLEFEYS, M. Real-time plane-sweeping stereo with multiple sweeping directions. In *Proc 25th IEEE Conf on Computer Vision and Pattern Recognition*.

[28] GUPTA, A., EFROS, A., AND HEBERT, M. Blocks world revisited: Image understanding using qualitative geometry and mechanics. In *Proc 12th European Conf on Computer Vision* (2010), pp. 482–496.

[29] HARTLEY, R. I., AND ZISSERMAN, A. *Multiple View Geometry in Computer Vision*, second ed. Cambridge University Press, ISBN: 0521540518, 2004.

[30] HEDAU, V. Thinking inside the box: Using appearance models and context based on room geometry. *Proc 12th European Conf on Computer Vision* (2010).

[31] HEDAU, V., HOIEM, D., AND FORSYTH, D. Recovering the spatial layout of cluttered rooms. In *Proc 12th IEEE Int Conf on Computer Vision* (2009), vol. 2.

[32] HEITZ, G., AND KOLLER, D. Learning spatial context: Using stuff to find things. In *Proc 10th European Conf on Computer Vision* (2008), pp. 30–43.

[33] HOIEM, D., EFROS, A. A., AND HÉBERT, M. Automatic photo pop-up. *ACM Transactions on Graphics 24*, 3 (2005), 577.

[34] HOIEM, D., EFROS, A. A., AND HÉBERT, M. Geometric context from a single image. In *Proc 10th IEEE Int Conf on Computer Vision* (2005), pp. 654–661.

[35] HOIEM, D., EFROS, A. A., AND HÉBERT, M. Putting objects in perspective. In *Proc 24th IEEE Conf on Computer Vision and Pattern Recognition* (2006), pp. 2137–2144.

[36] HUYNH, D. Q. Metrics for 3D Rotations: Comparison and Analysis. *Journal of Mathematical Imaging and Vision 35*, 2 (June 2009), 155–164.

[37] JEBARA, T. Images as bags of pixels. In *Proc 9th IEEE Int Conf on Computer Vision* (2003), pp. 265–272.

[38] JULESZ, B. Textons, the elements of texture perception, and their interactions. *Nature 290* (Mar. 1981), 91–97.

[39] KANATANI. *Geometric Computation for Machine Vision*. Oxford University Press, USA, 1993.

[40] KLEIN, G., AND MURRAY, D. Parallel tracking and mapping for small AR workspaces. In *Proc 6th IEEE/ACM Int Symp on Mixed and Augmented Reality* (Nara, Japan, November 2007).

[41] KOLMOGOROV, V., AND ZABIH, R. What energy functions can be minimized via graph cuts? *IEEE Transactions on Pattern Analysis and Machine Intelligence* (2002).

[42] KOSECKÀ, J., AND ZHANG, W. Video compass. In *Proc 7th European Conf on Computer Vision* (2002), Springer, pp. 476–490.

[43] LEE, D. C., HEBERT, M., AND KANADE, T. Geometric reasoning for single image structure recovery. In *Proc 27th IEEE Conf on Computer Vision and Pattern Recognition* (June 2009).

[44] LEJEUNE-DIRICHLET, P. *Vorlesungen ber Zahlentheorie*. Vieweg, Braunschweig, 1863.

[45] LI, Y., AND HUTTENLOCHER, D. Learning for stereo vision using the structured support vector machine. In *Proc 26th IEEE Conf on Computer Vision and Pattern Recognition* (2008), pp. 1–8.

[46] LINDEBERG, T. *Scale-Space Theory in Computer Vision*. Kluwer Academic Publishers, Norwell, MA, USA, 1993.

[47] LOWE, D. Object recognition from local scale-invariant features. In *Proc 7th IEEE Int Conf on Computer Vision* (1999), pp. 1150–1157.

[48] MACKAY, D. J. C. *Information Theory, Inference, and Learning Algorithms*, vol. 22. Cambridge University Press, 2003.

[49] MALIK, J., BELONGIE, S., SHI, J., AND LEUNG, T. Textons, contours and regions: cue integration in image segmentation. In *Proc 7th IEEE Int Conf on Computer Vision* (1999), vol. 2, pp. 918–925.

[50] MIRZAEI, F. M., AND ROUMELIOTIS, S. I. Optimal estimation of vanishing points in a Manhattan world. In *Proc 13th IEEE Int Conf on Computer Vision* (2011), pp. 2454–2461.

[51] MOZOS, O., STACHNISS, C., AND BURGARD, W. Supervised learning of places from range data using adaboost. In *Proc 2005 IEEE Int Conf on Robotics and Automation* (2005), pp. 1730–1735.

[52] NEDOVIC, V., SMEULDERS, A., REDERT, A., AND GEUSEBROEK, J. Stages as models of scene geometry. *IEEE Transactions on Pattern Analysis and Machine Intelligence 32*, 9 (2010), 1673–1687.

[53] PARZEN, E. On estimation of a probability density function and mode. *The Annals of Mathematical Statistics 33*, 3 (1962), 1065–1076.

[54] POSNER, I., SCHROETER, D., AND NEWMAN, P. Online generation of scene descriptions in urban environments. *IEEE Journal of Robotics and Automation 56*, 11 (2008), 901–914.

[55] REN, X., AND MALIK, J. Learning a classification model for segmentation. In *Proc 9th IEEE Int Conf on Computer Vision* (Oct. 2003), pp. 10–17 vol.1.

[56] ROBERT E. SCHAPIRE, YOAV FREUND, P. B., AND LEE, W. S. Boosting the margin: A new explanation for the effectiveness of voting methods. *The Annals of Statistics 26*, 5 (1998), 1651–1686.

[57] ROBERTS, L. *Machine perception of 3–d solids*. PhD Thesis, 1965.

[58] SAXENA, A., SUN, M., AND NG, A. Y. Make3d: Learning 3d scene structure from a single still image. *IEEE Transactions on Pattern Analysis and Machine Intelligence 31*, 5 (2009), 824–840.

[59] SCHARSTEIN, D., AND SZELESKI, R. A taxonomy and evaluation of dense two–frame stereo correspondence algorithms. *International Journal of Computer Vision* (2001).

[60] SCHINDLER, G., AND DELLAERT, F. Atlanta world: an expectation maximization framework for simultaneous low-level edge grouping and camera calibration in complex man-made environments. In *Proc 22nd IEEE Conf on Computer Vision and Pattern Recognition* (2004), vol. 1, pp. I–203.

[61] SHI, J., AND MALIK, J. Normalized cuts and image segmentation. *IEEE Transactions on Pattern Analysis and Machine Intelligence 22*, 8 (2000), 888–905.

[62] SHUFELT, J. Performance evaluation and analysis of vanishing point detection techniques. *IEEE Transactions on Pattern Analysis and Machine Intelligence 21*, 3 (Mar 1999), 282–288.

[63] SINHA, S., STEEDLY, D., SZELISKI, R., AGRAWALA, M., AND POLLEFEYS, M. Interactive 3d architectural modeling from unordered photo collections. In *ACM Transactions on Graphics* (2008), vol. 27, ACM, p. 159.

[64] STACHNISS, C., MARTNEZ-MOZOS, O., ROTTMANN, A., AND BURGARD, W. Semantic labeling of places. In *Proc Int Symp on Robotics Research, 2005* (2005).

[65] SZUMMER, M., KOHLI, P., AND HOIEM, D. Learning crfs using graph cuts. *Proc 10th European Conf on Computer Vision* (2008), 582–595.

[66] TASKAR, B., KLEIN, D., COLLINS, M., KOLLER, D., AND MANNING, C. Max-margin parsing. In *Proc Conf on Empirical Methods in Natural Language Processing* (2004), pp. 1–8.

[67] TORRALBA, A. Contextual priming for object detection. *International Journal of Computer Vision 53*, 2 (2003), 169–191.

[68] TSOCHANTARIDIS, I., HOFMANN, T., JOACHIMS, T., AND ALTUN, Y. Support vector machine learning for interdependent and structured output spaces. *Proc Int Conf on Machine Learning 36* (2004), 104.

[69] VAPNIK, V. *The Nature of Statistical Learning Theory*. Springer–Verlag, New York, 1995.

[70] VAPNIK, V. N. *Statistical Learning Theory*, vol. 2. Wiley-Interscience, 1998.

[71] VARMA, M., AND ZISSERMAN, A. A statistical approach to texture classification from single images. *International Journal of Computer Vision 62*, 1-2 (2005), 61–81.

[72] VASUDEVAN, S., GÄCHTER, S., NGUYEN, V., AND SIEGWART, R. Cognitive maps for mobile robots—an object based approach. *Proc. Robotics and Autonomous Systems 55*, 5 (2007), 359–371.

[73] WERNER, T., AND ZISSERMAN, A. New Techniques for Automated Architectural Reconstruction from Photographs. In *Proc 7th European Conf on Computer Vision* (2002), pp. 541–555.

[74] YANG, W., TRIGGS, W., DAI, D., AND XIA, G.-S. Scene Segmentation with Low-dimensional Semantic Representations and Conditional Random Fields. *Journal on Advances in Signal Processing* (2010), 1–14.

[75] ZEISL, B., ZACH, C., AND POLLEFEYS, M. Stereo reconstruction of building interiors with a vertical structure prior. In *Proc Int Conf on 3D Imaging, Modeling, Processing, Visualization and Transmission* (2011), pp. 366–373.

[76] ZHU, S., GUO, C., WANG, Y., AND XU, Z. What are textons? *International Journal of Computer Vision* (2005), 121–143.